X-Ray Fluorescence Imaging with a Laser-Driven X-Ray Source

Dissertation
zur Erlangung des Doktorgrades
an der Fakultät für Mathematik, Informatik und Naturwissenschaften
Fachbereich Physik
der Universität Hamburg

vorgelegt von
Theresa Maria Staufer

Hamburg
2020

Gutacher der Dissertation:	Prof. Dr. Florian Grüner Dr. Jens Osterhoff
Zusammensetzung der Prüfungskommission:	Prof. Dr. Daniela Pfannkuche Prof. Dr. Florian Grüner Dr. Jens Osterhoff Dr. Elisabetta Gargioni Prof. Dr. Wolfgang Parak
Vorsitzende der Prüfungskommission:	Prof. Dr. Daniela Pfannkuche
Datum der Disputation:	11. August 2020
Vorsitzender Fach-Promotionsausschuss PHYSIK:	Prof. Dr. Günter Hans Walter Sigl
Leiter des Fachbereichs PHYSIK:	Prof. Dr. Wolfgang Hansen
Dekan der Fakultät MIN:	Prof. Dr. Heinrich Graener

„Als Wissenschaftler schafft man keine Fakten“

– Prof. Dr. med. Christian Drosten, German virologist during the Covid-19 pandemic

Abstract:

The medical imaging modality of X-ray fluorescence imaging (XFI), first proposed in 1986 by Boisseau, offers the possibility to utilise gold nanoparticles (GNPs) that are functionalised with specific biomarkers, offering the advantage of low dose exposure and high detection sensitivity. If these nanoparticles are injected into an organism, they can be taken up by tumour cells - a prevailing challenge for commonly used imaging modalities like computed tomography (CT) or positron emission tomography (PET), especially for early tumour diagnostics. Excitation with the subsequent emission of fluorescence X-rays of the nanoparticles can either be done with conventional or laser-driven X-ray sources. Recent work in our group has shown that excitation with monochromatic X-ray beams from a synchrotron yields the best results with respect to sensitivity. These sources have circumferences on the order of hundreds of metres, making them unsuitable for applications in hospitals. Therefore, it is necessary to develop more compact sources such as laser-driven Thomson X-ray sources. The recent developments in the field of laser wakefield acceleration and in laser technologies offer the possibility to shrink the acceleration length of electrons from the km- to the cm-scale by using the ponderomotive force of highly intense laser pulses. Combining this mechanism with the process of Thomson scattering in which electrons transfer part of their energy to incident laser photons, results in a compact, high energy X-ray source. Further optimisation by e.g. the implementation of focusing devices such as active plasma lenses lead to the even better properties of tunability and low bandwidth of the resulting radiation spectra. Currently existing limits such as low laser repetition rates and electron charge densities can be overcome with kHz-laser systems and elaborated electron injection schemes. Therefore, such a novel source can be an excellent driver for XFI with all the desired properties.

Zusammenfassung:

Die Methode der Röntgenfluoreszenzbildgebung wurde bereits von Boisseau im Jahr 1986 vorgeschlagen und war seitdem das Thema zahlreicher wissenschaftlicher Studien. Diese Bildgebungsmethode ermöglicht es, geringe Mengen von Goldnanopartikeln, die an spezifische Biomarker gekoppelt werden, zu detektieren. Dabei bleibt die Dosisbelastung gering, während die Nachweisempfindlichkeit hoch ist. Wenn diese Nanopartikel in einen Organismus injiziert werden, können sie sich an Tumorzellen anlagern, die vor allem im Frühstadium mit heute gängigen Bildgebungsverfahren wie Computertomographie (CT) oder Positronen-Emissions-Tomographie (PET) oft nicht detektiert werden können. Die Anregung zur nachfolgenden Emission von Fluoreszenzphotonen kann entweder durch konventionelle oder laserbasierte Röntgenquellen erfolgen. Untersuchungen unserer Gruppe haben gezeigt, dass Anregung durch monochromatische Röntgenstrahlen von einem Synchrotron die besten Ergebnisse in Bezug auf die Nachweisempfindlichkeit liefert. Diese Anlagen haben meist einen Umfang in der Größenordnung von hunderten Metern, was sie für medizinische Anwendungen in Krankenhäusern uninteressant macht. Deshalb ist es nötig, kompaktere Quellen, wie zum Beispiel laserbasierte Thomson-Röntgenquellen, zu entwickeln. Aufgrund der vielen Neuentwicklungen im Bereich der Beschleuniger- und Lasertechnologie ist es heute möglich, die Beschleunigungsstrecke für Elektronen von Kilometern auf lediglich wenige Zentimeter zu schrumpfen indem man die ponderomotive Kraft eines extrem intensiven Laserpulses nutzt. Die Kombination aus Laser-Plasma-Beschleunigung und Thomson-Streuung, in welcher relativistische Elektronen einen Teil ihrer Energie auf Laserphotonen übertragen, resultiert in kompakten, hochenergetischen Röntgenquellen. Weitere Optimierungen durch z.B. den Einbau fokussierender Elemente wie Plasmalinsen führen zu Durchstimmbarkeit und niedriger Bandbreite der resultierenden Röntgenspektren. Aktuell exisitierende Limits wie niedrige Laser-Repetitionsraten und Elektronen-Ladungsdichten können durch den Einsatz von kHz-Lasersystemen und angepassten Elektronen-Injektionsmechanismen überwunden werden. Eine solche neuartige Quelle liefert somit alle nötigen Eigenschaften für XFI neben der Tatsache, dass sie sich auf deutlich kleinerem Raum verwirklichen lässt als die heutigen Synchrotron-Strahlungsquellen.

Contents

1 Introduction

Wilhelm Conrad Röntgen's famous discovery of a "new kind of rays" in 1895 [1] was quickly followed by first clinical applications of X-rays only one year later. Over many decades, doctors used two-dimensional projection radiography to depict structures within human bodies without the necessity to cut it open. The development of the first computed tomography (CT) scanner by Godfrey Hounsfield in 1972 [2] finally extended the method to 3-dimensional imaging. Both of these so-called transmission imaging methods are based on the property that human tissues selectively attenuate X-ray intensities which can be used to form an image.

Another famous discovery at about the same time, radioactivity, by Antoine Henri Bequerel in 1896 [3] and the subsequent development of radioactive tracers to study physiological processes by George Hevesy in 1923 [4], were the foundation stones of nuclear medicine. In this modality, radiotracers whose molecules are labelled with radionuclides that emit spontaneous radiation, are injected into an organism. There, they move according to the natural uptake of the carrier molecule, reflecting its physiological behaviour. Today, three different nuclear imaging modalities exist which are scintigraphy, single-photon emission CT (SPECT) and positron emission tomography (PET). The last commonly used method is magnetic resonance imaging (MRI) which is based on the property of nuclear magnetic resonance. Several different operation modes such as functional MRI (fMRI) or magnetic resonance spectroscopic imaging (MRS) offer the possibility to visualise various body functions, e.g. the brain metabolism [2]. Depending on the object of investigation, it is the task of radiologists to find the most appropriate diagnostic method.

X-ray fluorescence imaging (XFI) had first applications for biological samples such as for the estimation of strontium in an animal bone [5] or the determination of calcium, potassium, chlorine, sulphur and phosphorus in biological tissues [6]. In XFI, characteristic X-ray photons are produced from a dedicated sample after irradiation, making it possible to determine the elements contained within the sample. The spatial resolution of this method is only determined by the applied beam diameter, which can be as low as several µm and therefore extremely sensitive.

For the investigation of bigger samples, typically elements with a high atomic number Z, such as gold, are functionalised with specific peptides and injected into an organism [7]. Following the natural behaviour of the peptide, the elements accumulate at dedicated regions of interest and, after external irradiation emit characteristic X-ray photons.

In recent years, nanomedicine, especially in the form of nanoparticles, has gained much popularity for a wide range of applications, including the imaging of "deep tumours" with gold nanoparticles (GNPs) [8]. One big advantage of such particles lies in the fact that their properties can be easily influenced by varying their size and shape, making it possible to tailor their characteristics to specific needs [9]. For the purposes of XFI, GNPs offer the further advantages of a high photoelectric interaction probability and specific tumour targeting. Furthermore, gold as an element is non-toxic and chemically inert.

Ideally, XFI is performed with monochromatic X-rays which are nowadays produced at high-brilliance synchrotron sources where the energy of the incident radiation can be precisely tuned to maximise the fluorescence-to-background ratio [10]. However, as those machines have circumferences on the order of kilometres, they are impractical for clinical purposes. The recent developments in accelerator and laser technology have given rise to the construction of novel laser wakefield accelerators, based on an idea first published by Tajima and Dawson in 1979 [11]. They proposed to use the intense electric field of a relativistic plasma wave, driven by an intense laser pulse, to accelerate electrons to high energies. Such a plasma has the ability so sustain an acceleration gradient on the order of 100 GV/m, orders of magnitude higher than in conventional RF accelerating modules. Their acceleration gradient is limited to about 100 MV/m mainly by structure breakdown [12]. Therefore, it is possible to accelerate electrons to high energies on a mm- or cm-scale in plasma-based accelerators [13].

Until the 1980s, the amplification of ultra-short laser pulses was limited by self-focusing and other nonlinear processes of intense laser pulses. This phenomenon can be overcome with the principle of chirped pulse amplification (CPA), first demonstrated by Donna Strickland and Gerard Mourou in 1985 [14] at the University of Rochester. Instead of amplifying the compressed pulse, a long pulse is produced by stretching a short, low-energy pulse. The stretched, linearly chirped pulse is then amplified and afterwards compressed, allowing much higher energies before self-focusing occurs. CPA is since then the technique used by the highest-power lasers and Strickland and Mourou received the Nobel Prize in Physics in 2018, as their pioneering work led to huge progress in laser technology.

The production of X-ray and γ-ray radiation via the process of scattering photons from highly energetic electrons was first proposed and demonstrated in the 1960s, after the discovery of the laser [15–18]. Starting in the 1990s, several results from Thomson scattering (TS) sources were published including comprehensive theories and source designs [19, 20] as well as experimental demonstrations [21]. The combination of laser wakefield acceleration and Thomson scattering offers the possibility to design compact X-ray sources with photon energies ranging from the keV- to the MeV-level and low-bandwidth energy distributions. Especially in combination with focusing devices for the accelerated electrons, such a source can offer optimal conditions for XFI. Another possibility is the use of conventional linear accelerators which have been able to produce highly energetic electrons in a stable manner for many years, again in combination with Thomson scattering. Even though their footprint is not as compact as in an all-optical setup, they offer the advantage of more stable electron parameters, e.g. tuneable energy, very low energy spread, high charge, small emittance and resultingly high photon fluxes [22].

The basics of X-ray physics, semiconductors, gold nanoparticles and data analysis are discussed in chapter 2. Chapter 3 explains the principles of laser-plasma acceleration, the experimental production of electron beams in such novel accelerators and the different injection mechanisms. In chapter 4, Thomson scattering and the various influences on the resulting radiation are discussed, followed by a short introduction to simulation and software frameworks in chapter 5. The used laser system, diagnostics and laboratories are presented in chapter 6 and chapter 7 describes the setup of the first proof-of-principle experiment as well as results from Thomson signal and XFI measurements with a laser-driven, Thomson X-ray source. Finally, chapter 8 presents the optimised experimental setup with an active plasma lens and its results and discusses the next steps towards a high-flux X-ray source.

2 Basics of X-ray physics, semiconductors, XFI and statistics

2.1 Ionising radiation

Today's concept of atomic structure is based on a quantum mechanical picture of the atom which arose from the Bohr model of the hydrogen atom [23]. Bohr postulated that an atom consists of a nucleus, formed by protons and neutrons, surrounded by orbiting electrons. The electrons are organised in orbits or shells, labelled with capital letters, starting with the K-shell closest to the nucleus, followed by the L-shell and so on, as shown in figure 2.1. Each atom has a ground

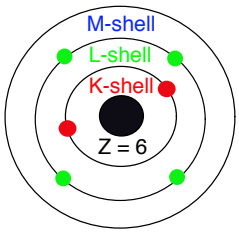

Figure 2.1: Arrangement of electrons into shells for the carbon atom. Electrons are restricted to specific quantum states within each shell, leading to a maximum number of electrons per shell. For the carbon atom this means that two electrons are allowed in the K-shell and four more are allowed in the L-shell.

state configuration for its electrons which corresponds to the lowest energy configuration of the atom. Energetically it is more favourable for an electron to be bound in an atom than to be free. Thus, the total energy of the atom is less than the total energy of the atom (minus the electron) and the (free) electron. The difference between these two energies is called the binding energy of the electron, usually specified in units of electron volts (eV). This energy depends on the element to which an electron is bound and on the occupied shell.

If radiation transfers energy to an orbiting electron equal to or higher than its binding energy, it is ejected from the atom. This process is called ionisation and the forms of ionising radiation

Frequency Range [Hz]	Wavelengths	Photon Energies	Description
$1\cdot 10^5 - 3\cdot 10^{10}$	3 km – 0.01 m	413 peV – 124 meV	Radio waves
$3\cdot 10^{12} - 3\cdot 10^{14}$	100 – 1µm	12.4 meV – 1.24 eV	Infrared radiation
$4.3\cdot 10^{14} - 7.5\cdot 10^{14}$	700 – 400 nm	1.77 – 3.1 eV	Visible light
$7.5\cdot 10^{14} - 3\cdot 10^{16}$	400 – 10 nm	3.1 – 124 eV	Ultraviolet light
$3\cdot 10^{16} - 3\cdot 10^{18}$	10 nm – 100 pm	124 eV – 12.4 keV	Soft X-rays
$3\cdot 10^{18} - 3\cdot 10^{19}$	100 – 10 pm	12.4 – 124 keV	Diagnostic X-rays
$3\cdot 10^{19} - 3\cdot 10^{20}$	10 – 1 pm	124 keV – 1.24 MeV	Gamma rays

Table 2.1: Summary of frequencies, wavelengths and photon energies of the electromagnetic spectrum

can be divided into particulate and electromagnetic radiation. The latter is conceptualised of photons with energies given by

$$E = h \cdot \nu, \tag{2.1}$$

where $h = 6.626 \cdot 10^{-34}\mathrm{Js}$ is Planck's constant and ν is the frequency of radiation in Hz.

The electromagnetic spectrum ranges from radio waves up to gamma rays which differ in frequency and therefore have different photon wavelengths and energies as shown in table 2.1. Gamma rays and X-rays are not distinguished by their photon energies but rather by their point of origin. While X-rays are created in the electron cloud of atoms, gamma rays originate from the nuclei of atoms undergoing reorganisation due to radioactive decay. Hence, gamma rays are associated with radioactivity and X-rays are not.

2.2 Fundamental properties of ionising radiation

The following sections about ionising radiation and its properties were extracted from Pearson's Medical Imaging book [2] if not stated otherwise. Ionising radiation interacts with materials it is traveling through by depositing energy. As a consequence, new types of particles and radiation are created. Electrons for example can interact with a medium by collisional and radiative energy transfer. In the first case, a fraction of the electron's kinetic energy is transferred to another electron in the target medium with which it collides. As this affected atom returns to its original state, infrared radiation is generated, producing heat in the target medium. Furthermore, the path of the incident electron can be changed because of the interaction and many more interactions may take place until all kinetic energy is lost. In radiative transfer, the electron's

interaction with an atom produces X-rays. This can also happen in two different ways which are characteristic radiation or Bremsstrahlung radiation. In the first process, the incident electron collides with an electron from one of the shells, kicking it out and temporarily leaving a hole. This hole is then filled by an electron from one of the higher shells which experiences a loss of energy. During this process, a photon is created with a characteristic energy, exactly equal to the difference in electron binding energies between the two shells. This process is shown in figure 2.2.

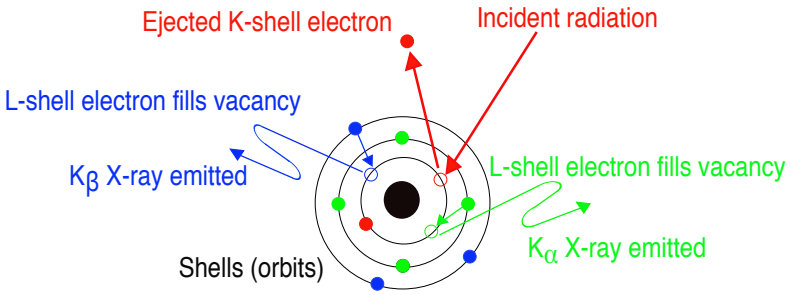

Figure 2.2: Generation of characteristic radiation, if incident electrons have enough energy to kick out inner-shell electrons

Bremsstrahlung on the other hand is caused by the interaction of an electron with the nucleus of an atom as the positive charge of the nucleus attracts the electron, causing it to orbit around the nucleus. Since the electron decelerates around the nucleus, it loses energy in form of a photon as shown in figure 2.3. Bremsstrahlung radiation is the primary source of X-rays produced in a conventional X-ray tube.

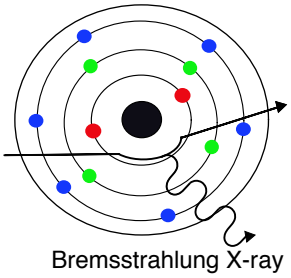

Figure 2.3: Generation of Bremsstrahlung radiation due to energy loss of an electron in the field of a nucleus

2.3 Primary electromagnetic radiation interactions

In principle, there are four main mechanisms by which ionising radiation interacts with matter:

- Photoelectric effect
- Rayleigh scattering
- Compton scattering
- Pair production

The photoelectric effect was discovered by Albert Einstein and describes the process in which energy quanta in the form of photons penetrate the body's surface layer and transfer their energy to a single electron [24]. The incoming photon is completely absorbed by the atom, while the electron, usually referred to as photoelectron, is ejected with the energy

$$E = h \cdot \nu - E_B, \tag{2.2}$$

where E_B is the binding energy of the electron. The resulting hole must be filled with an electron from one of the higher shells which produces radiation with characteristic energies as illustrated in figures 2.2 and 2.4. The emission of light with an energy generally lower than the absorbed radiation, is called fluorescence.
Sometimes, it can happen that the produced characteristic X-ray transfers its energy to an electron in one of the outer shells which is consequently ejected as a so-called Auger electron. This leads to a readjustment of the remaining electron shells as shown in figure 2.5.

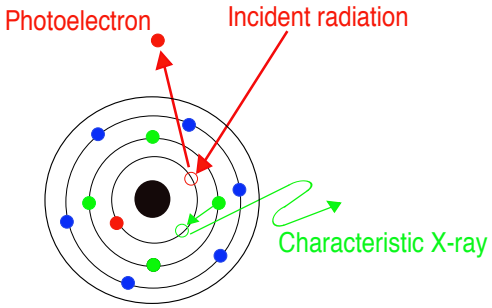

Figure 2.4: Principle of the photoelectric effect leading to the ejection of an electron and characteristic X-ray radiation. In contrast to figure 2.2, the characteristic radiation is generated by incoming photons, kicking out electrons.

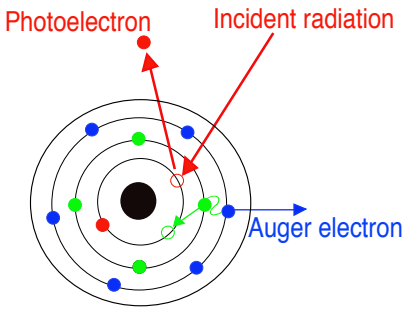

Figure 2.5: The produced characteristic X-ray may transfer its energy to an electron from one of the outer shells, leading to the ejection of an Auger electron

Since a photoelectric event occurs as a result of an electron interacting with the Coulomb field of the nucleus, the probability for such an event is proportional to Z_{eff}^4, where Z_{eff} represents the number of protons that an electron effectively is influenced by [25]. The other factor is the energy of the incident photon since high-energy photons penetrate deeper into an object before being absorbed. Therefore, the probability for a photoelectric event is given by

$$P_{photoeffect} = \frac{Z_{\text{eff}}^4}{(h \cdot \nu)^3}. \tag{2.3}$$

Rayleigh scattering involves the elastic scattering of X-rays by atomic electrons where no ionisation occurs. The energy of the scattered X-ray is therefore identical to the energy of the incident X-ray, but the scattered X-ray ends up with a changed trajectory. This process is most likely for low-energy X-rays and high-Z materials.

Compton scattering on the other hand is the process of inelastic scattering of an X-ray photon by an atomic electron. It typically occurs at higher X-ray energies where the energy of the incoming photon is much greater than the binding energy of the atomic electron. The products of the interaction are a scattered photon with an energy of $h \cdot \nu'$, an electron and an ionised atom, related via

$$h \cdot \nu' = \frac{h \cdot \nu}{1 + (1 - \cos\theta)\frac{h \cdot \nu}{m_0 \cdot c^2}}, \tag{2.4}$$

where $m_0 \cdot c^2 = 511\,\text{keV}$ is the energy equivalent to the rest mass of an electron and θ is the observed scattering angle, as shown in figure 2.6. From the equation above, it can be seen that a photon loses more energy, the more it is deflected and the maximum energy loss occurs in a 180 ° backscatter event. Since Compton events occur with outer shell electrons, the probability for such an event is proportional to the target electron density.

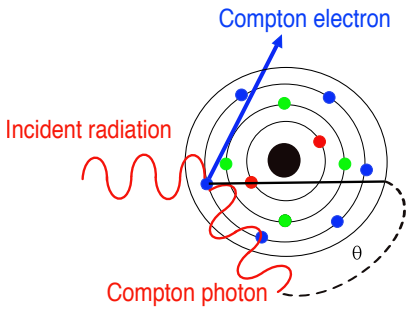

Figure 2.6: An X-ray photon may transfer its energy to an electron from one of the outer shells which leads to the ejection of a Compton electron and a modified trajectory of the incoming photon

Pair production is the last main electromagnetic interaction process, but since it can only occur at energies higher than 1.022 MeV, i.e. two m_e, it is not relevant for the medical imaging purposes discussed in this thesis where the energies are in the keV range.

Since the different radiation interactions influence diagnostic imaging differently, it is important to understand their relative frequency of occurrence in body tissues [2] which is summarised in table 2.2. The relative frequency of Compton scattering interactions increases as the incident energy gets higher. Above 30 keV, it is the dominant mechanism in water and therefore also in human tissue. Nevertheless, at 60 keV, where Compton scattering occurs in over 90 per cent of all events, these events account for only 55 per cent of energy deposited in the tissue. This phenomenon can be explained with the fact that photoelectric events deposit all of their incident photon energy while in Compton scattering only a fraction is deposited.

Photon Energy [keV]	Percentage of Compton Interactions	Percentage of Compton Energy
10	3.2	0.1
20	26.4	1.3
40	77.9	19.3
60	93.0	55.0
80	97.0	78.8
100	98.4	89.6
150	99.5	97.4

Table 2.2: Percentage of Compton interactions and of Compton energy deposition in water for diagnostically relevant X-ray energies taken from [2]

2.4 Attenuation of electromagnetic radiation

Attenuation is the process in which a beam of electromagnetic radiation loses energy as it propagates through material [2]. If there is a slice of material present between an incident X-ray beam and a detector, some photons will be absorbed within the material by the photoelectric effect while others undergo Compton scattering and are deflected away. As a consequence, less photons are registered by the detector. If n is the number of photons lost in such a scenario, Δx is the thickness of the slice and N the number of recorded photons without the slice of material, the following relation holds:

$$n = \mu N \Delta x. \tag{2.5}$$

The constant of proportionality μ is the so-called linear attenuation coefficient and it can be interpreted as the number of photons lost per length interval. Approximating the slice by an infinitely small object and considering the number of recorded photons N as a continuous quantity, leads to

$$N = N_0 e^{-\mu \Delta x}, \tag{2.6}$$

where N_0 is the number of photons at $x = 0$. In general, μ is material-dependent and varies as a function of energy for the same material, which also represents the primary mechanism by which contrast is created in radiographic imaging. Figure 2.7 shows that bone is more attenuating than soft tissue and that X-rays are more penetrating at higher energies. In many applications not μ itself is calculated but rather $(\frac{\mu}{\rho})$, the mass attenuation coefficient in cm^2/g with ρ representing the mass density of the material.

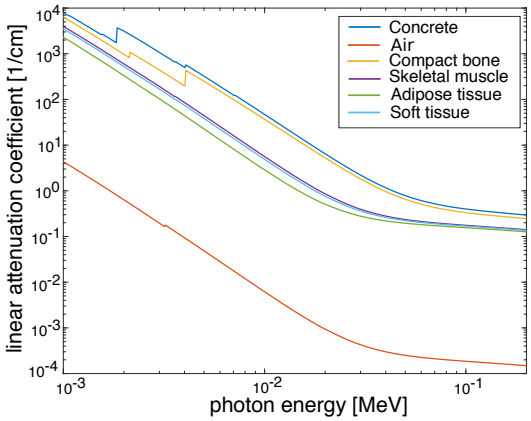

Figure 2.7: Linear attenuation coefficients for concrete, air, compact bone, skeletal muscle, adipose and soft tissue as a function of incident X-ray energy. The tables of absorption were taken from NIST [26] and embedded in MATLAB code [27].

2.5 Radiation dosimetry

The definition of ioinising radiation as given in section 2.2 implies that electromagnetic radiation passing through a material deposits energy by both the photoelectric effect and Compton scattering, which is the concept of dose, given the symbol D. The SI-unit of the absorbed dose, gray [1 Gy = 1 J/kg], refers to an energy-deposition concentration rather than a total amount of energy. Another closely related unit is called kerma, defined as the amount of energy per unit mass transferred to the electrons in the exposed material, also measured in Gy. For completeness, also the linear energy transfer (LET) has to be mentioned, which characterises the energy transferred to a material per unit length, where a higher LET produces greater biological consequences.

Understanding the effects of dose is not only relevant in a medical context, also in our everyday lives we are exposed to ionising radiation from cosmic rays, building materials, soil and other sources. However, different types of radiation can have different effects on an exposed organism, which is accounted for within the concept of the dose equivalent H, defined as $H = DQ$, with the quality factor Q, a property of the type of radiation. Since $Q \approx 1$ for X-rays, gamma rays and electrons, H is equivalent to D in typical medical applications and for a dose of 1 Gy and Q = 1, H is 1 sievert [1 Sv = 1 J/kg]. However, if not X-rays but protons ($Q \approx 10$) or alpha particles ($Q \approx 20$) are used, it is essential to consider the much higher dose equivalent.

Finally, it is necessary to define dose levels for medical applications which keep the main risk of cancer production as low as reasonably possible. Therefore, another quantity, the effective dose is used, which represents the sum of dose equivalents to different organs or tissues multiplied with a weighting factor. This way, a value is provided that allows to compare the potential risks for different radiations and target tissues. The effective dose $D_{effective}$ is expressed as

$$D_{effective} = \sum_{organs} H_j w_j, \tag{2.7}$$

with H_j the dose equivalent for an organ j and w_j the same organ's weighting factor. Typical dose levels reached in medical applications range from 0.02 mGy for a single chest X-ray examination up to 10 mGy for a CT scan of the whole abdomen/pelvis [28]. Therefore, 10 mGy of integrated absorbed dose for the intersection volume of an object of investigation and the incident beam are also used as an upper dose limit in the context of XFI.

2.6 Semiconductor detectors

Semiconductor detectors based on germanium (Ge), silicon (Si) and cadmium-telluride (CdTe) created revolutionary advances in nuclear physics, chemistry, non-destructive materials analysis and other fields [29]. To date, however, they have a limited effect on medicine due to their disadvantages of small size and high cost compared with other systems. Nevertheless, the energy resolution of semiconductor detectors allows the separation of γ- and X-rays differing in energy by only a few keV or even less. This is a huge advantage in applications where energy resolution is the critical factor. A more detailed description of the properties and functionality of semiconductors is given in this section, following the framework of [29].

2.6.1 Basic principle

Semiconductor detectors are essentially solid-state analogues of gas-filled ionisation chambers. Because their materials are 2000 to 5000 times denser than gases, they have much better stopping power and are therefore more efficient detectors for X- and γ-rays. Such detectors normally are poor electrical conductors but when they are ionised, the electrical charge produced can be collected by an externally applied voltage. This principle could not be used with conducting detector materials (e.g. a block of metal) because such a material would conduct a large amount of current even without ionising events. Insulators (e.g. glass) on the other hand are not suitable detector materials either, because they do not conduct any charge even in the presence of ionising radiation.

When ionising radiation is absorbed in a semiconductor crystal, electron-hole pairs are created which are collected through the application of an electric field. Each crystal has a quantised electron energy band structure that describes the allowed energy states in the crystal lattice as shown in figure 2.8 (a). In a pure crystal, the electron can only reside in the many close-lying energy levels of the valence or conduction band and not in the well-defined energy gap E_g between them. The interaction of a nuclear particle raises the energy of electrons from the valence band, where they are bound to a particular lattice site, across the energy gap to the conduction band where the electrons are free to move around the crystal lattice. This action leaves a positive hole or absence of a valence electron and under an appropriate electric field, the electron will move toward the anode and the positive hole will move toward the cathode as shown in figure 2.8 (b).

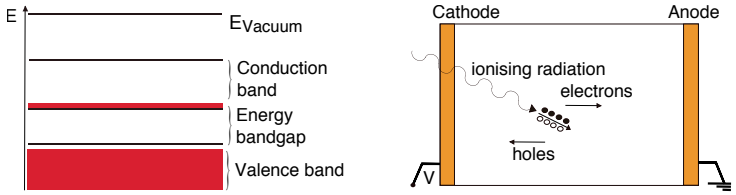

(a) (b)

Figure 2.8: Simplified energy band diagram used to describe semiconductors (a). Since the electronic properties of a semiconductor are dominated by the highest partially empty and the lowest partially filled band, it is sufficient to only consider these bands. When ionising radiation is absorbed in a semiconductor crystal, electron-hole pairs are created (b). Due to the application of an external voltage V, the electrons are moving toward the anode and the holes in the opposite direction toward the cathode.

A small energy gap will yield a large number of electron-hole pairs from a particle interaction and the goal is the complete collection of the charge carriers such that the amplitude of the detected electrode signal is proportional to the number of electrons and holes created. However, not all semiconductors make good detectors. Owing to the higher atomic density in semiconductor detectors, trapping of charge carriers at defects or impurities can become a severe issue. The mobilities of electrons and holes should be high and the lifetimes long for fast signal rise time and efficient charge collection. So, the purity of semiconductor materials must be extraordinarily high, which can be realised for germanium, but at the moment is a challenging factor for CdTe.

The most commonly used semiconductor materials are silicon, germanium and cadmium telluride. In the following, only CdTe-detectors will be described in more detail, since the high stopping power of this material makes it excellent for applications requiring high detection efficiency at energies up to 120 keV [30]. X-rays and γ-rays interact with CdTe atoms to create an average of one electron-hole pair for every 4.43 eV of energy lost in the material. Depending on the energy of the incoming radiation, this energy loss is either dominated by the photoelectric effect or by Compton scattering. The probability to effectively stop the incoming radiation and create electron-hole pairs, the efficiency of the detector, increases with the thickness of CdTe. In order to facilitate the collection of the created pairs, a 500 Volt potential is applied which is too high for operation at room temperature as it will cause excessive leakage and eventually a breakdown. Therefore, a thermoelectric cooler is typically implemented to cool both the detector and the input field effect transistor (FET). The current is then sent to the charge sensitive preamplifier in order to reduce leakage and thus, reduce the electronic noise of the system.

2.6.2 Charge transport

At the electric field strengths usually found in a radiation detector, the drift velocity of the carriers is proportional to the electric field strength, where the constant of proportionality is defined as the mobility [31]. The duration of the transient current pulse is determined by the distance the carriers have to travel. There are two clearly distinct current pulses, one from holes and the other from electrons, where the electrons produce a much higher current for a shorter time, due to their higher mobility. Because the hole lifetime is typically much shorter than the hole transit time, the induced current is significantly reduced. Further, the signal strength also depends upon the depth of interaction in the detector. About one-eighth of the interactions will occur near the front contact, in the region of the detector where charge collection efficiency is maximum and constant. Interactions occurring deeper will create a smaller signal, with the smallest signals arising from interactions at the cathode, where the signal is entirely due to the hole current. This results in a tail sloping down from the energy of the peak to a minimum at the charge collection efficiency of the cathode, which is why the effect is called hole tailing. It is mainly observed in compound semiconductors which have a far higher density of defects in the crystal lattice than e.g. silicon detectors where carrier lifetimes are several milliseconds long.
For spectroscopy, this effect means that, instead of a simple Gaussian with a small tail extending smoothly to zero, a significant fraction of the photon counts occurs in the tail, which terminates at a specific value. An examplary spectrum taken with an AMPTEK XR-100T CdTe detector [30], a high performance detector ideal for X-ray spectroscopy above 25 keV, at the P07 beamline of the PETRA III synchrotron at DESY is given in figure 2.9, where the noticeable features are indicated. Apart from the already described hole tailing effect, also escape peaks are clearly significant in the spectrum. Those peaks are again more important in CdTe than in other detector materials and are created if photons with an incident energy higher than the K-absorption edges of Cd and Te undergo photoelectric interactions, leaving the Cd and Te atoms in an excited state. As those atoms go back to the ground state, the emission of characteristic X-rays follows and depending on the direction, those X-rays then might leave the sensitive detector volume such that only a small amount of the incident energy is actually deposited in the volume. Therefore, peaks are visible at the characteristic energies of Cd and Te, as well as at the energy difference between the incident energy and the characteristic energy of the respective material. Table 2.3 lists the energies of the K-edges and the characteristic energies of Cd and Te and figure 2.10 illustrates the possible processes in a CdTe detector chip. However, the phenomenon of hole-tailing is strongly reduced in pixelated detectors which will be discussed in the following section.

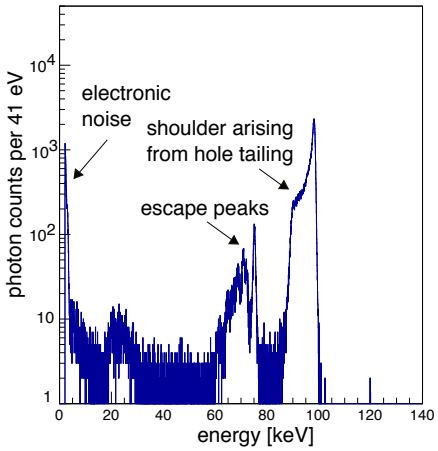

Figure 2.9: Spectrum taken at the P07 beamline with an incident energy of 98.2 keV. Besides the peak at the expected incident energy, the shoulder left to it and escape peaks between 60 and 80 keV are clearly visible. Such detector effects have to be considered in spectroscopic measurements as signal counts might be in the energy region of escape peaks or the shoulder from hole tailing, making it hard to discriminate them from the intrinsic detector background.

Element	K-edge [keV]	$K_{\alpha 1}$ [keV]	$K_{\alpha 2}$ [keV]	$K_{\beta 1}$ [keV]	$K_{\beta 2}$ [keV]
Cd	26.71	23.17	22.98	26.09	26.06
Te	31.81	27.47	27.20	30.99	30.95

Table 2.3: K-absorption and characteristic energies of the detector materials Cd and Te

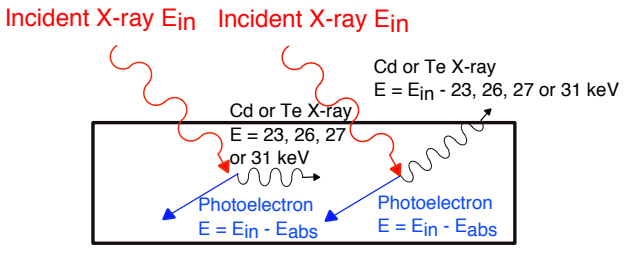

Figure 2.10: Schematic drawing of possible events in a CdTe detector if photons of an incident energy higher than the K-absorption energies of Cd and Te hit the sensitive area. In the left scenario, the complete incident energy is deposited, while in the right scenario, a characteristic X-ray escapes. As a consequence, peaks at the characteristic energies of Cd and Te, as well as at energies E_{in} - $E_{characteristic}$ occur in the measured spectrum.

2.6.3 Pixelated detectors

For future clinical applications, it is not sufficient to use a small detector such as the AMPTEK XR-100T with only a sensitive area of 25 mm^2, since in that case it would be necessary to move the detector in very small steps around the patient, increasing measurement time and applied dose. Therefore, one has to look for alternative solutions, especially pixelated detectors with a much bigger sensitive area. Up to date, it is very challenging to produce such detectors from CdTe and so far only prototypes with sensitive areas up to 100 cm^2 exist [32]. One company that has taken the step towards bigger CdTe detectors is Quantum Detectors, a spinout from the Science and Technology Facilities Council and Diamond Light Source [33]. They have developed the HEXITEC system, a fully spectroscopic hard X-ray imaging detector shown in figure 2.11. This detector is capable of measuring the energy and position of every incident photon in the 4-200 keV range, where each one of the 80 x 80 pixels provides a full energy spectrum with an average energy resolution of 800 eV FWHM at 60 keV. It is a self-contained module that only requires a mains power supply and connection to a computer, where it can be supplied with a user-friendly GUI to operate the detector and provide calibrated spectra per pixel. Further specifications of the HEXITEC system include:

- Frame rate: 9 kHz
- Data rate: 5×10^6 photons/second
- Dimensions: 21 x 5 x 5 cm
- Sensitive detector area: 4 cm^2
- Weight: 700 g
- HEXITEC modules can be supplied with CdTe or cadmium zinc telluride (CZT) of various thicknesses

Figure 2.11: Photograph of a HEXITEC detector. The active area of 4 cm^2 is covered by an Al-window located at the right side of the module.

While the key features and benefits of this detector system sound very promising, also here several effects have to be studied, which was done in [34]. The phenomenon of the so-called small-pixel effect, which demonstrates that by reducing the anode size (pixel) with respect to the cathode, the weighting potential becomes strongly magnified close to the anode, is described using the Shockley-Ramo theorem [35]. It states that the charge Q and current i on an electrode

induced by a moving point charge q are given by

$$Q = -q\phi_0(\mathbf{x}) \tag{2.8}$$

$$i = q\mathbf{v} \cdot \mathbf{E}_0(\mathbf{x}). \tag{2.9}$$

$\mathbf{v}$ is the instantaneous velocity of the charge q, $\phi_0(\mathbf{x})$ and $\mathbf{E}_0(\mathbf{x})$ are the electric potential and field that would exist at q's instantaneous position $\mathbf{x}$ under the following circumstances: the selected electrode is at unit potential, all other electrodes are at zero potential and all charges are removed. ϕ_0 and $\mathbf{E}_0$ are called the weighting potential and the weighting field, respectively. While the trajectory of the charge q is determined by the actual operating electric field, the induced charge Q can be calculated much easier with the help of the weighting field because there is only one field that must be calculated, which is independent of the moving charge q and space charge is not involved. The proof of this theorem, based on the conservation of energy [35], shows how the energy is transferred from external power supplies to the moving charge q in an actual device. Here it should be kept in mind that the charge induced on an electrode by q is independent of the actual bias voltages on each electrode.

In the instance of a reduced anode size, only carriers drifting close to the pixel will induce a charge. For interactions occurring close to the cathode, the holes will be collected without inducing a significant charge on the pixel, consequently reducing the effect of hole tailing. In this arrangement, only the electrons, which have good transport properties in CdTe, contribute to the spectroscopy. However, one of the limitations of small pixel detectors is the increase in the number of charge sharing events between pixels as the size of the single pixels decreases relative to the thickness of the device. As soon as an interaction occurs within the detector, the resulting charge cloud diffuses both perpendicular and parallel to the applied field. The diameter of the charge cloud thereby increases due to carrier diffusion and charge repulsion, of which the latter effect occurs mainly in dense charge clouds created by high-energy interactions [36]. For a sufficiently long drift time, the size of the charge cloud becomes comparable to the pixel pitch and consequently the diffusion perpendicular to the field is significant compared to the pixel size, such that there is a high probability that charge will be shared between pixels [37].

An analytical solution of the diffusion equation gives [36]

$$\sigma^2 = 2\,D\,t_{drift}, \tag{2.10}$$

where σ is the width of the charge cloud, t_{drift} describes the time the charge has drifted and D represents the diffusion coefficient. The diffusion coefficient is described by Einstein's relationship: $D = \mu\, k_B\, T\, q$, with μ the mobility of the carrier, k_B the Boltzmann constant, T the temperature of the semiconductor and q the electrical charge. At room temperature, D for electrons in CdTe has a value on the order of 25 $cm^2\ s^{-1}$, while holes only have a value of 0.25 $cm^2\ s^{-1}$. In a 2 mm thick CdTe sensor at -300 V bias voltage, drift times are on the order of 100 ns and the resulting diameter of a charge cloud is around 60 µm [36]. If the contribution of the charge sharing events is not corrected for, the spectroscopy performance of the detector will be affected which will be further discussed and demonstrated in section 6.3.1.

For a good compromise between small pixels for low tailing and large enough pixels to allow efficient inter-pixel-sharing processing to be achievable, the HEXITEC collaboration has chosen a 250 µm pitch. This also allows to integrate the low-noise electronics and their connections to the pixels via a simple, low cost bump bonding process [38]. With this geometry, typically 40 % of events are shared between pixels. In case of charge-sharing, the signals can either be added together (addition) or if efficiency is not a problem, shared events can simply be rejected (discrimination). The pixel structure has a rolling shutter architecture so that the 20 columns of outputs of each of the 80 rows are sent sequentially to an ADC (analogue to digital converter) which is repeated four times on the ASIC (application-specific integrated circuit). These four outputs allow the ASIC to operate in 20 x 80 x 50 ns plus some extra clock cycles for data alignment such that the effective readout happens at about 10000 frames per second. Each pixel in the structure has a preamplifier to read out the induced charge formed on the electrode, followed by a 2 µs shaper and a peak-track-and-hold circuit. This circuit stores the peak value of the largest signal that occurs in the frame which represents the charge deposited in the detector and is thus proportional to the energy of the single photon stopping in the detector. This analogue voltage is then held until the end of the frame where it is transferred to the row output. Here, only the largest energy photon in each frame is readout of each pixel.

The readout of the HEXITEC is operated with a 20 MHz clock with separate outputs for four blocks such that a full frame of 80 $\times$ 80 pixels is read out at a rate of 10 kHz. The ASIC is only sensitive to electron readout and the noise performance per channel was determined to be better than 800 eV. In order to still be able to properly compensate for charge sharing, a maximum rate of $\sim 2.5 \times 10^6$ photons $s^{-1}\ cm^{-2}$ has been estimated as only a limited number of pixels can detect an event in a single frame [36].

2.7 X-ray Fluorescence Imaging (XFI) and Gold Nanoparticles (GNPs)

In XFI, characteristic X-ray photons are produced from a sample, making it possible to identify the elements contained within the object of investigation. Typically, elements with a high atomic number, like gold, are functionalised with specific peptides [7] and injected into an organism. Thus, they are accumulating at the regions of interest and emitting characteristic photons after the excitation with an X-ray source.

GNPs offer unique physical and chemical properties due to their different shapes and sizes [39]. The progress of engineered nanoparticles at the scale of 5 to 100 nm over the last few years opens the possibility for a wide range of biomedical applications such as imaging, diagnostics and many more [7]. Gold nanoparticles are promising candidates for such applications since they have favourable physiochemical properties and large absorption and scattering cross-sections that can be controlled by varying their size. Besides their non-toxicity [40], an advantage is given by the fact that GNPs can be conjugated with various peptides and antibodies like, e.g., L1. This neural cell adhesion molecule, which has shown positive effects in acute and chronic diseases, coupled to GNPs, is a promising candidate to localise neural diseases. Furthermore, GNPs acting as drug delivery agents can increase the pharmacokinetics of the drug which leads to the reduction of side effects and can achieve higher doses of targeted drug delivery [39] which makes them suitable to act as vehicles for the delivery of molecules into cells.

Even though nanomaterials offer significant improvements in cancer diagnosis and treatment, there still are a few challenges that have to be overcome. One of them is to determine the uptake of nanoparticles by tumorous tissue, typically less than 5 % because of poor retention within the tumour and uptake by organs such as the skin, spleen and liver [41]. Sykes et al. [42] have studied the influence of changing tumour pathophysiology, mainly caused by tumour growth, on the ideal nanoparticle size, shape and surface chemistry for targeting tumours. They were able to characterise changes in the physiological structures and microenvironment of tumours as they grew, e.g. cell density, vascularity, necrosis and stroma, and the following changes in the uptake of polyethylene glycol (PEG)-coated GNPs. Different sizes (diameters of 15, 30, 45, 60 and 100 nm) of GNPs were used and it was found that larger nanoparticles become more effective when tumours mature, while small ones are applicable for detection and drug delivery when the tumour size is unknown. This is mainly caused by the fact that tumour tissue

becomes more dense and chaotic as tumours mature, thus restricting blood flow and consequently preventing agents from reaching their target. While smaller particles are then still able to penetrate tumours, nanoparticles with diameters of 100 nm or even larger do not penetrate tumours any more as they sequester near tumour blood vessels. Under this consideration of tumour biology and nanoparticle size, they were able to experimentally show a much higher GNP uptake by prostate tumours up to 40 % of the injected amount. This concept of "personalised nanomedicine" by tailoring nanoparticle designs according to the patient's tumour characteristics, has the potential to improve the targeting process for the detection of tumours by over 50 %.

Apart from imaging applications, GNPs are also used in therapy, as e.g. shown in [43] where gold-silica nanoparticles were designed such that they absorb near-infrared light at wavelengths of high tissue transparency to provide a highly localised light-based strategy for the treatment of prostate cancer. This example shows that in case of a highly tuneable X-ray source, it is possible to first use GNPs for the localisation of a tumour and secondly make use of their enhancing properties in tumour therapy without the necessity of moving the patient to different treatment stations.

The nanoparticles for the experiments reported in this thesis were manufactured at the Center for Hybrid Nanostructures (CHyN) which is part of the Institute of Nanostructure- and Solid State Physics (INF) of the University of Hamburg in the group of Prof. Dr. Parak. Research done in this group showed that the physiochemical properties of GNPs are mainly accounted for by their hydrodynamic diameter and their zeta potential (the measure of surface charge) which in turn determines the in vitro uptake and in vivo biodistribution of those particles [44]. For any scenario of an in vitro or in vivo application of GNPs, the nanoparticles would be exposed to proteins which eventually will adsorb to the surface of the particles and, furthermore, their kinetics depends on the interaction between nanoparticles and proteins [45, 46].

2.8 Data analysis

2.8.1 Fitting algorithm for photon spectra

Even if filters, collimators, and an optimal detector geometry are used for the measurements, the total counts registered by the detector are the sum of background coming from Compton scattered X-rays and fluorescence X-rays from the target element and other elements in the setup. Therefore, it is necessary to isolate the signal from the background by constructing an

appropriate fit. The region selected for this analysis covers the strongest lines present, resulting from fluorescence processes in the target element, lead from the shielding and the electron beam dump and the detector material CdTe. The background non-peak region is fitted with a third-order polynomial function and interpolated to give an estimate of the background function in the region of the signal peaks. Gaussian functions are used to fit the fluorescence signals, limited by the following constraints:

- For the Gaussians fitted to the characteristic gold K-lines, the width is fixed to the values of the norm spectrum of a gold-foil.
- The width of the Gaussians fitted to the characteristic Gd K-lines is fixed to the values of the spectrum of 78 mg/ml Gd-solution.
- All peak positions are set to the corresponding peak energies taken from [47].

Finally, the number of fluorescence photons is given by the area underneath the Gaussian functions, divided by the bin width of the histogram.

If one wants to quantify the level of agreement between the data and a hypothesis, a test of significance [48] has to be carried out. The discrepancy between the data and the expectation under the assumption of a hypothesis H_0 is quantified by the p-value. It is defined as the probability to find a defined statistic t in the region of equal or lesser compatibility with H_0 than the level of compatibility observed with the actual data,

$$p = \int_{t_{\text{obs}}}^{\infty} f(t|H_0)\,\mathrm{d}t, \tag{2.11}$$

where t_{obs} is the value of the statistic obtained in the experiment.

Often the p-value is converted into an equivalent significance Z which is usually expressed in units of the standard deviation σ,

$$Z = \Phi^{-1}(1-p), \tag{2.12}$$

with Φ being the cumulative distribution of the standard Gaussian and Φ^{-1} its inverse function.

For a very large number of photons, the calculation of the significance can be simplified to

$$Z \approx \frac{n_{\text{obs}} - n_{\text{exp}}}{\sqrt{n_{\text{exp}}}}. \tag{2.13}$$

In order to make sure that the net signal was within the 99.7 % confidence interval, only signal values in the interval $\pm 3\sigma$ around the $K_{\alpha 1}$ and $K_{\alpha 2}$ fluorescence lines are considered. The evaluation of this combined significance is commonly used for the quantification of the signal quality in XFI measurements and will be used in this thesis as well.

The last statistical parameter of interest is the so-called goodness-of-fit, where one obtains the minimum value of the quantity χ^2. As it is a Poisson distribution with variances $\sigma_i^2 = \mu_i^2$, this quantity becomes Pearson's χ^2 statistic,

$$\chi^2 = \sum_{i=1}^{N} \frac{(n_i - \mu_i)^2}{\mu_i}. \tag{2.14}$$

If the hypothesis $\mu = (\mu_1, ..., \mu_N)$ is correct, and if the measurements n_i can be treated as a Gaussian distribution, then the χ^2 statistic will follow the probability density function with the number of degrees of freedom equal to the number of measurements N minus the number of fitted parameters. A χ^2 value close to one implies that the fit can describe the data well, whereas higher values represent a poor fit.

2.8.2 Fitting algorithm for electron spectra

The electron spectra are fitted with a Gaussian model in MATLAB [27] which is given by

$$y = \sum_{i=1}^{n} a_i e^{[-(\frac{x-b_i}{c_i})^2]}, \tag{2.15}$$

where a is the amplitude, b is the centroid (location), c is related to the peak width, n is the number of peaks to fit, and $1 \leq n \leq 8$. The corresponding two-term Gaussian model is therefore given by

$$y = a_1 e^{[-(\frac{x-b_1}{c_1})^2]} + a_2 e^{[-(\frac{x-b_2}{c_2})^2]}. \tag{2.16}$$

It has to be noted that the definition used in MATLAB is different from the standard Gaussian distribution (also known as standard normal distribution). The simplest case with a mean $\mu = 0$ and standard deviation $\sigma = 1$, is described by the probability density function

$$\phi(x) = \frac{1}{\sqrt{2\pi}} e^{-\frac{1}{2}x^2}. \tag{2.17}$$

Every normal distribution is a version of the standard normal distribution whose domain has

been stretched by a factor σ and then translated by μ as

$$f(x|\mu,\sigma^2) = \frac{1}{\sigma}\phi(\frac{x-\mu}{\sigma}). \tag{2.18}$$

The probability density must be scaled by $1/\sigma$ so that the distribution remains normalised. If Z is a standard normal deviate, then $X = \sigma Z + \mu$ will have a normal distribution with expected value μ and standard deviation σ. Conversely, if X is a normal deviate with parameters μ and σ^2, then $Z = (X - \mu)/\sigma$ will have a standard normal distribution.

If one wants to equate the standard deviation s (as defined in the MATLAB model) for a single Gaussian model, it can be computed by

$$s = c_1/\sqrt{2}, \tag{2.19}$$

while the mean value μ is simply given by the parameter b_1.

2.9 Basics of error calculation

Error estimation in scientific practice is necessary to quantify the results of a measurement. The first step is to determine whether the sources of error in the experiment are of systematic or random nature [49–51]. As a single measurement can have various possible error sources, the measurement should be repeated several times (if possible) to identify random errors, which are often quantified by the standard deviation of the measurements. If an observed value, e.g. the number of detected fluorescence photons, changes in each single measurement, it is highly likely that there is a random error. Detecting systematic errors on the other hand needs a more complex analysis of the whole setup and the assumptions made beforehand. One option to detect such an error would be a repeated measurement with a different method or by several different groups with various setups conducting the experiment.

As there exist several different error estimation methods, there may be no best option but still, some rules and formulae have to be considered. At the beginning of an estimation it is necessary to distinguish between independent and dependent errors as they are combined in different ways. If dependent values are combined, they accumulate in a linear manner while independent ones accumulate in quadrature (their squares add) since their randomness has the effect that multiple errors can cancel out each other.

If a quantity x is measured several times, the best estimate for x is given by the average or mean $\bar{x}$ defined as

$$\bar{x} = \frac{x_1 + x_2 + ... + x_N}{N} = \frac{1}{N}\sum_{i=1}^{N} x_i, \tag{2.20}$$

with N being the total number of measurements and x_i representing the single measurements [52]. The standard deviation is an estimate of the average uncertainty of the single measurements and is determined as

$$\sigma_x = \sqrt{\frac{1}{N-1}\sum_{i=1}^{N}(x_i - \bar{x})^2}. \tag{2.21}$$

With this definition, it provides a useful way to characterise the reliability of the measurements. The detailed significance of the standard deviation σ_x is that approximately 68 % of the measurements of x should lie within a distance σ_x of the true value [52]. In the context of this thesis, results where a certain quantity x is measured N times using the same method, are given as $(\bar{x} \pm \sigma_x)$.

3 Principles of laser-plasma acceleration

In 1979, Tajima and Dawson proposed to use the intense electric field of a plasma wave, created in the wake of an intense laser pulse, to accelerate electrons to relativistic energies [11]. The main advantage of plasmas lies in their ability to sustain an accelerating gradient much larger (on the order of 100 GV/m) than a conventional radio frequency (RF) accelerating module (on the order of 10 MV/m) such that electrons can be accelerated up to 1 GeV in millimetre- or centimetre-scale plasmas [13]. The huge progress in laser technology due to the development of chirped pulse amplification in 1985 has given rise to the construction of novel laser-plasma accelerators. If not stated otherwise, all information in the following sections was taken from [53].

3.1 Plasma properties

A useful definition of a plasma describes it as a quasi-neutral gas of charged and neutral particles which exhibits collective behaviour [54]. In the case of moving charged particles, local concentrations of positive or negative charge give rise to electric fields. Resultingly, also magnetic fields are created which affect the motion of other charged particles even at large distances. The particles in a plasma therefore behave collectively because of attractive and repelling forces. Owing to this collective behaviour, a plasma often behaves as if it had a mind of its own as it tends not to conform to external influences [54]. Quasi-neutrality on the other hand is a mathematical formulation for the fact that even though a plasma consists of free electrons and ions, their overall charge densities cancel each other in equilibrium [55]. If an electron in a quasi-neutral plasma slice is displaced from its initial position by a distance δ, e.g. due to a laser pulse, two "capacitor plates" with surface charge $\sigma = \pm e n_0 \delta$ are created [55]. This results in an electric field

$$\mathbf{E} = \frac{\sigma}{\epsilon_0} = \frac{e n_0 \delta}{\epsilon_0} \tag{3.1}$$

with the vacuum permittivity ϵ_0, the electron charge e and the ambient electron density n_0. Owing to this restoring force, the electron layer is accelerated back towards the slice according to

$$m_e \frac{dv}{dt} = -m_e \frac{d^2\delta}{dt^2} = -eE = \frac{e^2 n_0 \delta}{\epsilon_0}, \tag{3.2}$$

or

$$\frac{d^2\delta}{dt^2} + \omega_p^2 \delta = 0, \tag{3.3}$$

where

$$\omega_p \equiv \sqrt{\frac{e^2 n_0}{\epsilon_0 m_e}} \approxeq 5.6 \times 10^4 \sqrt{\frac{n_0}{\mathrm{cm}^{-3}}} \mathrm{s}^{-1} \tag{3.4}$$

is the electron plasma frequency [55] and m_e represents the electron rest mass. The inverse electron plasma frequency gives the fundamental time scale on which collective plasma effects occur.

3.2 Ponderomotive force

An important parameter in laser-plasma interactions is the laser strength parameter defined as the peak amplitude of the normalised vector potential of the laser field $a_0 \equiv eA_0/m_e c^2$. a_0 is related to the laser peak intensity I_0 by $I_0 = (\pi c/2)(m_e c^2 a_0/e\lambda)^2$, which yields

$$a_0^2 \approxeq 7.3 \times 10^{-19} [\lambda(\mu\mathrm{m})]^2 I_0(\mathrm{W/cm}^2) \tag{3.5}$$

with the laser wavelength $\lambda = 2\pi/k$ and $\omega = ck$ the laser frequency in vacuum. Physically, a_0 is equal to the normalised electron quiver motion in the laser field [56]. An expression for the ponderomotive force of an intense laser is in the non-relativistic regime is [57]

$$\mathbf{F_p} = -m_e c^2 \nabla a_0^2/2. \tag{3.6}$$

The ponderomotive force expels electrons from regions of high laser intensity and causes them to move towards regions of less intensity. The heavier ions are left behind, leading to a charge separation and the creation of an electric field.
The motion of an electron in a laser field is determined by the Lorentz force equation

$$\frac{\partial \tilde{\mathbf{p}}}{\partial ct} = \frac{\partial \mathbf{a}}{\partial ct} - (\tilde{\mathbf{p}}/\tilde{\gamma}) \times (\bigtriangledown \times \mathbf{a}), \tag{3.7}$$

where $\tilde{\mathbf{p}}$ is the electron momentum normalised to $m_e c$, $\tilde{\gamma} = (1+\tilde{p}^2)^{1/2}$ is the relativistic Lorentz factor and $\mathbf{a}$ the normalised vector potential of the laser field. The first term on the right-hand side causes the electrons to oscillate whereas the second term is responsible for "ponderomotive" laser acceleration.

3.3 Acceleration in plasma

In a laser wakefield accelerator, a single, short, high-intensity laser pulse drives a plasma wave which is most efficient if the laser pulse length is on the order of the plasma wavelength. As such an intense pulse propagates through an underdense plasma, the ponderomotive force expels electrons from the laser axis which leads to charge separation and the excitation of large amplitude plasma waves. A typical experiment consists in focusing a laser pulse into a gas target, where the interaction parameters are the laser intensity, focal spot size and duration and plasma density. Depending on these parameters, the features of the resulting electron bunches can be very different.

Ionised plasmas can sustain electron plasma waves with electric fields in excess of $E_0 = cm_e\omega_p/e$ or as described by the cold nonrelativistic wave breaking field [58]

$$E_0(\mathrm{V/m}) \approxeq 96\sqrt{n_0(\mathrm{cm^{-3}})} \tag{3.8}$$

with c being the speed of light in vacuum. Hence, for a plasma density of n_0 = 10^{18} cm^{-3}, an acceleration gradient on the order of 96 GV/m can be achieved.
Another feature of plasma-based accelerators lies in their capability of producing extremely short electron bunches. The length of the accelerating wave in such an accelerator is approximately the plasma wavelength $\lambda_p = 2\pi c/\omega_p$ or

$$\lambda_p(\mu\mathrm{m}) \approxeq 3.3 \times 10^{10}/\sqrt{n_0(\mathrm{cm^{-3}})}, \tag{3.9}$$

e.g. $\lambda_p \approxeq 33$ µm for n_0 = 10^{18} cm^{-3}. An electron bunch produced in a plasma-based accelerator can therefore have a bunch duration of $\tau_b < \lambda_p/c$ which gives a duration of less than 100 fs for n_0 = 10^{18} cm^{-3}.

3.3.1 The cavitated wakefield or bubble regime

The most efficient mechanism to accelerate electrons in a plasma wave is the so-called bubble, blowout or cavitated wakefield regime. It is reached when the laser intensity is sufficiently high ($a_0 > 2$) to expel most of the electrons out of the focal spot and the pulse duration is on the order of half a plasma wavelength ($c\tau \sim \lambda_p/2$). If these conditions are met, a spherically shaped ion cavity is formed in the wake of the laser pulse, where electrons can be trapped at the back and accelerated by the high electric field until they reach the middle of the cavity where they start to decelerate. By setting the acceleration length close to the dephasing length (the distance over which electrons must propagate before they start to decelerate), electrons exit the plasma with the maximum energy gain. The maximum electric field and the radius of the cavity are, respectively,

$$E_m = m\,\omega_p\,c\,\sqrt{a_0}/e, \tag{3.10}$$

and

$$r_b = \omega_0 = (2/k_p)\sqrt{a_0}. \tag{3.11}$$

For a typical experimental condition accessible with present lasers, e.g. $a_0 = 4$ with a 30 fs laser, the maximum electric field is $E_m \sim 600$ GeV/m and the radius of the cavity is $r_b \sim 7$ µm for an electron density of $n_e = 1 \times 10^{19}$ cm^{-3}.

3.3.2 Acceleration limits

There are several mechanisms which limit the energy gain in a laser-plasma accelerator such as laser diffraction, dephasing and depletion. In vacuum, a laser pulse undergoes Rayleigh diffraction which means that the laser spot size evolves as $r_s = r_0(1 + z^2/Z_R^2)^{1/2}$, where $Z_R = kr_0^2/2$ is the Rayleigh length and r_0 the minimum spot size at the focal point $z = 0$. Z_R describes the distance from the laser beam focus where the beam radius is increased by a factor of $\sqrt{2}$. The laser-plasma interaction distance is limited to a few Z_R if no optical guiding method such as using a plasma density channel is applied. Electron dephasing occurs if the highly relativistic electrons outrun the wakefield, which typically has a phase velocity < c, and consequently decelerate. This process happens over the dephasing length which is defined as the length an electron must travel before it phase slips by one-half of a period with respect to the plasma wave.

Pump depletion describes the laser energy loss as it excites a plasma wave and the pump depletion length can be estimated by equating the laser pulse energy to the energy left behind in the wakefield.

Prior to 2004, high plasma densities ($> 10^{19}$ cm^3) were used, resulting in electron bunches with broadband spectra, extending up to about 100 MeV. In 2004, major advances were made by setting the laser pulse duration close to the plasma period, increasing the interaction length and matching the dephasing to the propagation length. Thus, monoenergetic beams in the 100 MeV range, collimated within a few milliradians and with charges on the order of 100 pC could be produced. However, the high nonlinearity of this mechanism resulted in electron bunches which were neither stable nor tuneable in energy and which additionally remained below the GeV-level. One scheme to overcome these limitations is the external and controlled electron injection into the wakefield which consists of colliding the main laser pulse with a second laser pulse, creating a beat wave whose ponderomotive force can preaccelerate and locally inject background electrons in the wakefield. The energy of the electron bunch can then be tuned by varying the collision point and therefore the acceleration length, resulting in energies from a few tens of MeV to above 200 MeV with an energy spread on the order of 1 %.

Several other possibilities to control electron injection have been investigated recently, which are the use of a plasma density downramp, cold optical injection, ionisation-induced injection or magnetically controlled injection. The most important schemes in the context of this thesis are briefly summarised in the following section 3.4.

3.4 Injection mechanisms

A key feature of a novel accelerator lies in its reliability and stability of the produced electron bunches. In case of a laser wakefield accelerator this implies the controlled injection of electrons which can then be further used to vary the charge, divergence and also the energy of the electrons [59].

3.4.1 Self-injection

One possible injection mechanism relies on the process of wave breaking, or self-injection, where some electrons can become trapped in the wave close to the wave breaking threshold [60]. This threshold describes the point at which the plasma wave breaks and if the wave is driven even far beyond this threshold, the wave structure gets destroyed and large amounts of charge can be accelerated to high energies [61]. As electrons statistically scatter in forward direction into the wake where they get trapped, the injection happens as a continuous process.

This results in electrons receiving a different total acceleration due to different timings and a large energy spread of the bunch. The main parameters that have to be optimised for this injection mechanism include the pulse energy and power, the focal spot quality and furthermore, the processes of self-focusing and pulse compression have to be taken into account [60].

Since self-injection is based on highly nonlinear physics and depends crucially on the evolution of the laser pulse, it is hard to control and makes different methods, consisting in the "external" injection of electrons, desirable [62]. This can for example be done by using a second, counter-propagating laser pulse with the same wavelength and polarisation, where the first pulse creates a wakefield and the second one will only be used to inject electrons due to the generation of a slow beat wave [63].

3.4.2 Ionisation and shock-front injection

Another method achieves electron trapping initiated by ionisation in a laser wakefield accelerator which can increase the trapped charge and furthermore decrease the emittance of the resulting electron beam [64]. In [64], a range of different noble gases as well as nitrogen were added as a small percentage to helium gas. The underlying mechanism is based on the fact that the wakefield is excited in a plasma created from a gas mixture with multiple ionisation states. Gases with low atomic numbers have a low ionisation threshold and get fully ionised even at low laser intensities. A second gas with a higher atomic number only gets ionised close to the laser intensity peak. As the ponderomotive force is proportional to the intensity gradient, electrons ionised at the peak intensity experience a weaker transverse kick and can directly be trapped inside the wake and be accelerated. By using a gas mixture and therefore the process of ionisation injection, it is possible that even lower power laser systems can create high charge, high energy and low emittance electron beams. Although this approach offers simplicity and is relatively easy to realise, it has the disadvantage of continuous injection as long as the laser has enough intensity to ionise inner-shell electrons. This leads to the production of high charges but a relatively broad energy spectrum. Options to terminate the injection process are the use of dual-stage targets [65], shock-front injection [66] or self-truncated ionisation injection [67].

Shock-front injection is based on the creation of a shock front in a supersonic gas jet. When the laser crosses this shock front, ionised electrons spend more time in the accelerating field due to an expansion of the plasma cavity. Resultingly, they are more likely to be trapped, leading

to the production of stable electron beams with longitudinal and transversal momentum spreads up to ten times lower than with self-injected beams [66].

3.4.3 Self-truncated ionisation injection

The mechanism of self-truncated ionisation injection uses the evolution of the plasma cavity and its trapping conditions. By the use of an initially unmatched laser spot to ionise the doped gas, the injection process can be truncated and its distance limited to a few hundred micrometres [68]. The ionisation condition breaks due to self-focusing of the laser pulse in the plasma and the resulting wake deformation. Self-focusing in LWFA occurs due to the transverse nonlinear refractive index gradient of the plasma and the spot size decreases towards a matched spot size [60]. In [67], they report on the generation of quasi-monoenergetic, intense electron beams where the truncation is reached by combining relativistic self-focusing and the original laser focusing geometry. Experimentally, the laser focus is placed about one Rayleigh-length behind the gas jet target. This novel scheme was found to enable well-controlled tuning of the injected charge while preserving acceleration conditions and beam quality resulting in electron beams at several 100 MeV energy and 15 % relative energy spread with a total charge reaching 0.5 nC.

4 Thomson scattering theory

The production of X-ray and γ-ray radiation via the process of scattering photons from highly energetic electrons was first proposed and demonstrated in the 1960s, after the discovery of the laser [15–18]. Starting in the 1990s, several results from Thomson Scattering (TS) sources were published including comprehensive theories and source designs [19, 20] as well as experimental demonstrations [21, 69–72]. The produced radiation was, among other applications, used for nuclear resonance fluorescence experiments ([21]), to measure transverse and longitudinal density distributions of electron beams ([70]) and for quantitative computed tomography (CT) measurements ([72]).

Recent developments in laser-plasma acceleration technology, where electron energies up to the GeV-level can be achieved on a cm-scale [53], have opened up the possibility to design compact Thomson sources without the usage of storage rings for electrons as designed by Lynceantech [73]. The produced photon energies ranging from the keV- to the MeV-level can be used in many different areas such as medicine [74], nuclear research [75] and industry [76]. Due to the intrinsic short duration on the order of femtoseconds of electron beams produced in a laser-plasma accelerator and the intrinsic synchronisation to laser probe beams [77], easy setups for time-resolved studies are possible.

In order to reach high photon fluxes with a Thomson source, either large scattering lasers, high electron beam currents or other, novel solutions are required [78]. It has already been demonstrated that the production of GeV-electron beams is possible with a 40 TW laser system [79] which is nowadays available in sizes at the level of $6\,\mathrm{m}^2$ [80]. As increasing the electron current makes more radiation shielding necessary, it is not the first option of choice but rather maximising the photon yield per electron by working on the laser parameters. Conventionally, this requires laser pulses and electrons to be tightly focused while at the same time keeping the intensity low enough to avoid nonlinear broadening effects resulting in long pulse durations [78]. One optimisation strategy without the necessity to increase the source size is the usage of waveguides for diffractionless propagation [81] of the laser pulses to increase the interaction

length. Another means of flux enhancement and bandwidth reduction is the implementation of a discharge-capillary active plasma lens (APL) which can be used as an energy filter to reduce the effective electron energy spread [82], as discussed in detail in section 4.5. The upcoming sections describe the basic principles of Thomson scattering following the work of [78]. In the final section, already existing all-optical Thomson scattering X-ray sources with their main parameters are presented.

4.1 General concept of Thomson scattering

Thomson sources are often promoted as high photon energy sources of intrinsic small divergence. In the electromagnetic field of a laser, a relativistic electron oscillates due to the Lorentz force and emits radiation upon this acceleration. In its mean rest frame, the oscillating electron may be regarded as a Hertzian dipole and the emission angle in forward direction is Lorentz contracted. This emission angle is the synchrotron angle $\theta_S \sim 1/\gamma$ which lies in the sub-mrad divergence regime for electron energies of $\gamma > 1000$. The photon energy radiated by an electron of velocity β and Lorentz factor γ is given by

$$E_\gamma = \frac{2\gamma^2(1-\beta\cos\alpha)E_L}{1+\frac{a_0^2}{2}+\gamma^2\theta_{obs}^2} \tag{4.1}$$

with the laser photon energy $E_L = \frac{hc}{\lambda}$ and the interaction angle between laser and electrons α. θ_{obs} is the scattering angle of the photon with respect to the electron propagation direction and $a_0 = \frac{eA}{m_e c^2}$ represents the laser strength parameter containing the electron charge e, the laser pulse vector potential amplitude A, the electron rest mass m_e and the speed of light in vacuum c. A simple schematic of the scattering process with the corresponding angle definitions is shown in figure 4.1.

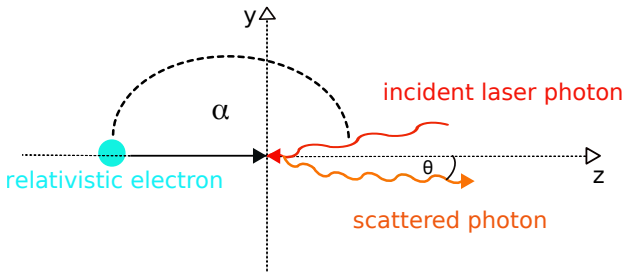

Figure 4.1: Schematic of the Thomson scattering process between an electron and laser photon with the corresponding angle definitions

The photon energy given in equation 4.1 can be derived from the scattering process of a single electron with a single photon. While in such a case only two single particles are involved, several effects arise when considering electron bunches and laser pulses. The first effect that has to be taken into account is the influence of the laser strength parameter a_0 which is the peak amplitude of the normalised vector potential. The highest accelerating fields in plasma-based accelerators can be reached with lasers with $a_0 > 1$, implying peak intensities $I_0 > 2.1 \times 10^{18}$ $\mathrm{W/cm^2}$ for a 800 nm wavelength laser. Lasers with $a_0 > 1$ have high intensity electrical fields which have an influence on the trajectories of electrons propagating through them. Those fields lead to large transverse oscillations and thereby a reduction of the longitudinal velocity of the electrons and consequently a reduction of the γ-factor for the interaction. Furthermore, the recoil of the electron can be neglected as long as the energy of the incoming photon is much lower than the rest energy of the electron, in the rest frame of the electron, and a_0 and γ are not extremely high [83], leading to the known expression for relativistic Thomson scattering given in equation 4.1. For an incoming photon with 800 nm wavelength, equaling an energy of 1.55 eV, this condition implies that the electron energy must be less than 85 GeV (coming from the relation $\frac{E_{e,rest}}{2E_i} \gg \gamma$), which is the case in all laser wakefield accelerator experiments considered in this thesis. The resulting energy reaches its maximum for $\alpha = \pi$ and $\theta = 0$. If also the influence of a_0 is neglected, the maximum energy can be approximated with

$$E_{s,max} \approx 4\gamma^2 E_i \tag{4.2}$$

which is shown in figure 4.2. The photon energy for such a head-on collision is given by the double relativistic Doppler shift.

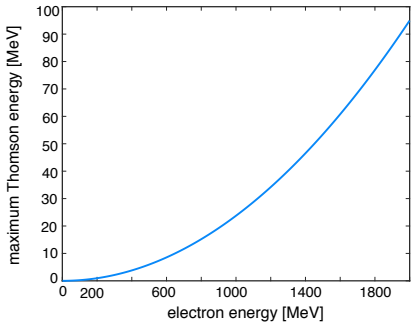

Figure 4.2: Maximum energy of Thomson scattered photons resulting from the scattering of λ = 800 nm photons on electrons with energies of 0 to 2000 MeV. The energies are calculated under the assumption that the scattering happens head on (α = 180 °), under the neglection of a_0 and for an observation angle θ of 0 °.

4.2 Influence of laser and electron parameters on the Thomson spectrum

The influence of electron and laser beam parameters on the resulting spectrum of Thomson scattered photons can be studied by looking at equation 4.1, where one can see that the energy of the generated photons depends on

- θ_{obs}, the observation angle of the generated photon,
- γ, the electron energy,
- a_0, the laser pulse amplitude, and
- E_L, the laser energy.

As realistic electron beams have non-zero divergence, the single particles moving under different angles will produce photon spectra with a peak in the original direction of propagation, consequently leading to a broad spectrum. Furthermore, electron energy spread also has a broadening effect on the resulting spectrum as different energies in the beam generate different photon energies as one can see from the γ - contribution in equation 4.1. Finally, the a_0 - term can lead to additional photon beam broadening as different frequencies will be generated at different times throughout the pulse. This is especially the case for focused, pulsed lasers where a transverse and longitudinal field gradient are present, thus increasing the bandwidth of the emitted energy. Another effect arising at a_0 values greater than one is the emission of photons into higher harmonics [84], making it necessary to keep a_0 at moderate values where a compromise between flux enhancement and bandwidth requirement can be found. An additional aspect one can derive directly from equation 4.1 is that the photon energy is maximum on the beam axis and decreases with larger observation angles θ_{obs}. A more detailed description of those effects is given in the following subsections.

4.2.1 Spectral shape of the produced Thomson radiation

The influence of laser and electron beam parameters on the characteristics of the resulting Thomson spectrum described above have to be studied in detail in order to design a source with certain radiation features such as narrow bandwidth and high photon numbers. The whole detailed derivation of the formulae occurring in this section can be found in [78]. The following assumptions were made for the calculation of the photon spectrum:

- Number of periods in the laser pulse N_0 is large ($N_0 \gg 1$), meaning that a photon with a specific energy also has a specific emission angle
- Neglection of the laser bandwidth and laser divergence
- Neglection of the slight angular spread due to focusing or diffraction of the laser pulse
- Assumption of an ideal case with no electron energy or angular spread

Starting from a particle moving with arbitrary trajectory, the total number of photons radiated into the cone $\theta_S = 1/\gamma$, the synchrotron angle, is

$$N = \frac{\pi}{3}\alpha\gamma^2 N_0 a_0^2, \tag{4.3}$$

where $\alpha \approx 1/137$ is the fine-structure constant and N_0 the number of oscillations (laser periods). The total number of photons radiated over all angles is twice this value, $N_\gamma = 2N$. The number of photons emitted into a confined angle θ smaller than θ_S, is given as

$$N_{\gamma,\theta} = N_\gamma \cdot \sigma(\kappa), \tag{4.4}$$

where κ describes the relative FWHM bandwidth of the photon source near the maximum frequency [82]. The percentage of photons radiated into θ is described by

$$\sigma(\kappa) = \kappa(\kappa^2 - \frac{3}{2}\kappa + \frac{3}{2}) \tag{4.5}$$

and the bandwidth contribution $\kappa = \frac{dE_\gamma}{E_\gamma}$ from the collimation angle $\pm\theta$ is given by [78]

$$\kappa = \frac{\gamma^2\theta^2}{1+\gamma^2\theta^2}. \tag{4.6}$$

A bandwidth of 15 % contains approximately 20 % of all generated photons, illustrating that the majority of generated photons has energies deviating from the central energy as the spectrum is only narrow bandwidth for a small angular range.

4.2.2 Effects of electron beam divergence

Electrons moving under different angles do not necessarily generate maximum frequencies along the z-axis but rather in their propagation direction. For the case of a circularly polarised

laser pulse interacting with a divergent electron beam, the approximate condition for the electron beam FWHM divergence can be derived as [78]

$$\gamma\sigma_{\theta,FWHM} < 2\sqrt{\kappa}. \tag{4.7}$$

Note that the polarisation has an effect on the polarisation of the generated X-ray beam but not on the total photon number.

4.2.3 Effects of electron beam energy spread

If only the effect of different electron energies resulting in different photon energies is considered and the electron beam is assumed to be non-divergent, one can get the following condition for the electron beam FWHM energy spread:

$$\frac{\sigma_{\gamma,FWHM}}{\gamma} < \frac{\kappa}{2} \tag{4.8}$$

assuming a Gaussian distribution for γ [78]. An electron beam with 10 % FWHM energy spread will consequently generate at least 20 % FWHM photon bandwidth. Thus, the electron energy spread has to be kept as low as possible. Electron beams produced in laser-plasma accelerators are suitable candidates as they can have energy spreads as low as a few % [85]. The combination of equations 4.7 and 4.8 gives an approximate condition for divergent beams with a certain energy spread for the on-axis bandwidth [78]:

$$\sqrt{\frac{\gamma^4\sigma^4_{\theta,FWHM}}{16} + \frac{4\sigma^4_{\gamma,FWHM}}{\gamma^2}} < \kappa. \tag{4.9}$$

4.2.4 Collimation angle and relative photon number

The goal of a narrow-bandwidth source requires collimation as the produced Thomson spectrum has an intrinsic correlation between produced energy and emission angle. Therefore, it is necessary to collimate the spectrum by first estimating the collimation angle θ_C and then calculating the number of photons emitted into this bandwidth. The collimation angle can be approximated as the angle for which the photon frequency is equal to $\omega = (1-\kappa)\cdot 4\gamma^2\omega_L$, or in other words [78]

$$\frac{1}{1+\gamma^2\theta_C^2} = 1-\kappa. \tag{4.10}$$

In combination with equation 4.7, one gets the following expression for the collimation angle:

$$\gamma\theta_C = \frac{\gamma\sigma_{\theta,FWHM}}{2} = \sqrt{\kappa}. \tag{4.11}$$

Thus, the peak value of the thereby obtained spectrum is $\frac{3}{2\sigma_\theta^2}$. Multiplying it by κ and the angular area $\frac{1}{2}\theta_C^2$ and using equation 4.11 for the collimation angle, the relative photon number lying in the desired bandwidth κ can be estimated with [78]

$$\frac{N_\kappa}{N_\gamma} \approx \frac{3}{2\sigma_\theta^2} \cdot \kappa \cdot \frac{1}{2}\theta_C^2 \approx \kappa. \tag{4.12}$$

According to this estimate, roughly 5 % of all generated photons are found in 5 % bandwidth.

4.2.5 Influence of a_0 and multiple scattering

As already discussed in section 4.2, it is possible to increase the total photon yield by using a higher laser amplitude a_0. Nevertheless, increasing this value induces some undesirable effects that have to be considered. In the nonlinear case with $a_0 > 1$, the commonly used equations to calculate Thomson spectra cannot be used any more as the higher laser amplitude leads to photon source bandwidth broadening and the occurrence of substructures in the spectrum [86]. Figure 4.3 shows the influence of a_0 on the resulting spectra calculated with the numerical code VDSR [87] for a single electron interacting with a Gaussian plane wave with an FWHM duration of 800 fs.

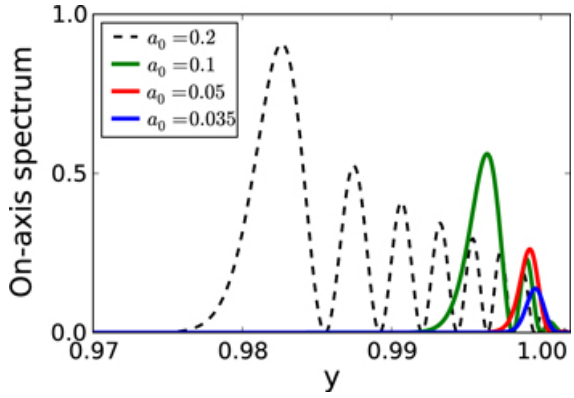

Figure 4.3: Normalised on-axis spectrum as a function of the normalised photon energy y for the different laser amplitude values a_0 = 0.035 (blue solid line), 0.05 (red solid line), 0.1 (green solid line) and 0.2 (black dashed line) taken from [78]

Increasing the laser pulse amplitude from a_0 = 0.035 to a_0 = 0.05, meaning that the laser photon number is doubled, does not change the shape of the spectrum and the amplitude increases by a factor of 2, proportional to the increased number of laser photons. Increasing the value of a_0 further leads to the occurrence of broadening and sidebands and even though the number of laser photons is still getting higher, the amplitude of the spectrum does not do so likewise any more. In general, this broadening is on the order of $\frac{a_0^2}{2}$ and for scattering from an electron beam, this value should be kept as low as possible relative to the electron energy spread and divergence effects discussed in sections 4.2.2 and 4.2.3 to minimise the bandwidth of the resulting Thomson spectrum [78]. The use of appropriately chirped mirrors can prevent such effects by counteracting the superposition of different wavelengths arising from the different a_0 values along the pulse [88].

4.3 Realistic energies

The Thomson energies interesting for XFI are shown in figure 4.4, where the photon energy is given in keV. Photons of 90 keV mean energy are needed for XFI applications and the energies are calculated under the assumption that the scattering happens under an angle α = 172 $^\circ$ and for a laser strength parameter a_0 of 0.25, which are realistic experimental conditions. In figure 4.5, a comparison for the Thomson energies achieved under the experimental conditions for different values of a_0 is shown. Larger values for the laser strength parameters require higher electron energies to reach a certain Thomson photon energy, e.g. while for a_0= 0.25 electrons with energies of 60 MeV are sufficient to produce photons with energies of 82 keV, for a_0 = 1, already 72.5 MeV of electron energy are required.

4.4 Total yield estimation

As in the experiments discussed here, the incoming photon energy in the rest frame of the electron is much lower than the rest energy of the electron, the recoil effect on the electron can be neglected and the Thomson cross-section can be used. It is defined by $\sigma_T = \frac{8\pi}{3} r_e^2$ with the classical electron radius $r_e = \frac{1}{4\pi\epsilon_0}\frac{e^2}{m_e c^2}$. The total number of scattered photons can be calculated as [78]

$$N_\gamma = \sigma_T \int_{-\infty}^{+\infty} v_{rel} n_e(t, \mathbf{r}) n_p(t, \mathbf{r}) d^3\mathbf{r} dt, \tag{4.13}$$

with $n_e(t, \mathbf{r})$ and $n_p(t, \mathbf{r})$ being the time- and space-dependent densities of electrons and photons, respectively, and v_{rel} the relative velocity of electrons and photons ($v_{rel} \approx 2c$).

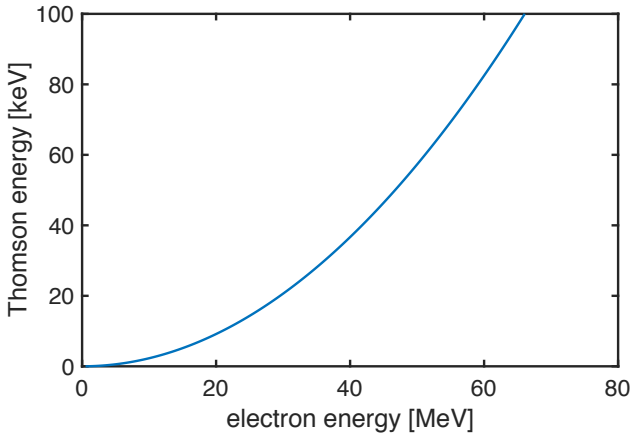

Figure 4.4: Energy of Thomson scattered photons resulting from the scattering of photons with a wavelength of λ = 800 nm on electrons with energies ranging from 0 to 80 MeV, the energy region interesting for XFI applications where photons of 90 keV mean energy are needed. The energies are calculated under the assumption that the scattering happens under an angle $\alpha = 172\,^\circ$ and for a laser strength parameter a_0 of 0.25. The observation angle θ is chosen to be $0\,^\circ$ where the energy has its maximum.

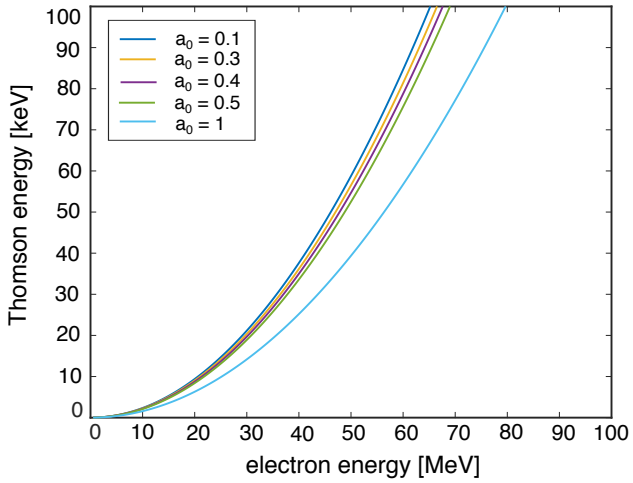

Figure 4.5: Energy of Thomson scattered photons resulting from the scattering of photons with a wavelength of λ = 800 nm on electrons with energies ranging from 0 to 80 MeV, the energy region interesting for XFI applications where photons of 90 keV mean energy are needed. The energies are calculated under the assumption that the scattering happens under an angle $\alpha = 172\,^\circ$ and for different laser strength parameters a_0 from 0.1 up to 1 (where the nonlinear regime starts). The observation angle θ is chosen to be $0\,^\circ$ where the energy has its maximum. As described in section 4.2.5, one can see that higher values for a_0 require higher electron energies to reach a certain X-ray photon energy.

Generally, the final integral can be calculated only numerically by simulation codes, but several analytical solutions exist for specific cases such as in [78] where the following derivation was taken from. For the case of an electron and laser beam interacting in vacuum and no relative displacements, the integral in equation 4.13 can be evaluated taking into account different beam sizes ($\sigma_{e,0}$ and $\sigma_{p,0}$) and beta-functions (β_e^* and β_p^*). The subscripts e and p denote electrons and laser photons respectively, σ_0 is the spot size at the focus position and the beta function is given by $\beta_e^* = \sigma_0^2/\epsilon_t$, where ϵ_t is the transverse geometrical emittance of the beam. The beta function of the laser photon beam equals its Rayleigh length. Integration yields

$$N_\gamma = \frac{\sigma_T N_e N_p F(x)}{\sqrt{2\pi}\sigma_l \sqrt{\sigma_{e,0}^2 + \sigma_{p,0}^2}} \frac{1}{\sqrt{\frac{\sigma_{e,0}^2}{\beta_e^{*2}} + \frac{\sigma_{p,0}^2}{\beta_p^{*2}}}}, \tag{4.14}$$

with x and $F(x)$ given by

$$\frac{\sqrt{2}}{\sigma_l} \sqrt{\frac{\sigma_{e,0}^2 + \sigma_{p,0}^2}{\frac{\sigma_{e,0}^2}{\beta_e^{*2}} + \frac{\sigma_{p,0}^2}{\beta_p^{*2}}}}, \tag{4.15}$$

$$F(x) = e^{x^2}[1 - \mathrm{erf}(x)], \tag{4.16}$$

respectively, and N denoting the total number of particles in the interaction of a certain kind. As a given laser beam is focused tightly, the photon yield increases due to a higher laser amplitude. Since such an intensity increase also causes broadening of the spectrum, as discussed in section 4.2.5, the desired source bandwidth sets an upper limit on the laser amplitude. By fixing the laser pulse energy E_L and its amplitude $a_{0,max}$, one can find the connection between longitudinal and transverse sizes and the total photon yield in the case when laser and electron beams have the same focus position and diverge in vacuum with given beta-functions β_e^* and β_p^*. There exists an optimal duration and laser spot size for every laser energy where the latter one is approximately twice the Rayleigh range. Taking all those considerations into account, the total photon yield per electron is given by

$$\frac{N_\gamma}{N_e} \approx 4.7 \cdot a_{0,max} \cdot \sqrt{\frac{E_L}{\lambda_{L,\mu m}}}, \tag{4.17}$$

with $\lambda_{L,\mu m}$ denoting the laser pulse wavelength measured in micrometres.

In the optimum case, the yield as given by equation 4.17, scales as a square root of energy which means that the laser energy has to be increased four times in order to increase the total yield by a factor of two.

4.5 Control of electron beam divergence and Active Plasma Lenses (APLs)

Several experiments [89, 90], including the one presented in chapter 7, have already successfully demonstrated the construction of broad bandwidth X-ray and γ-ray sources via Thomson scattering. But since many applications, especially medical ones, require narrow bandwidth sources, one has to control the electron beam divergence, as discussed in section 4.2.2. Since the design and construction of the Thomson scattering source discussed in this thesis are dedicated to X-ray fluorescence imaging, the ideal source parameters are used as an input and the source design is optimised to satisfy them. Several options exist to decrease the electron beam divergence, among them are the use of quadrupole magnet lenses [91, 92], density downramp [93] and active plasma lenses [94]. The latter one is discussed in this section as it is used in the optimisation process of the experimental setup presented in chapter 8.

APLs are ideal candidates to focus electron beams in laser-plasma based accelerators as they offer radially symmetric focusing and tunability in a compact design [95]. Such devices consist of a gas-filled capillary with a circular cross-section machined into glass or sapphire. If a multi-kV discharge voltage is applied to the ends of the capillary, breakdown of the gas occurs, driving a current along the generated plasma column. In this situation, the current density J is distributed approximately uniformly within the capillary and can be expressed as $J = I_0/(\pi R^2)$, with the total current I_0 and the capillary radius R. The magnetic field B_ϕ within the aperture ($r < R$) can be derived from Ampère's law

$$B_\phi(r) = \frac{\mu_0}{r} \int_0^r J(r')r'dr' \tag{4.18}$$

in case of a uniform current distribution $J(r') = J$ to be $B_\phi = \mu_0 Jr/2$. The corresponding high magnetic field gradient follows as

$$\partial B_\phi/\partial r = \mu_0 I_0/(2\pi R^2) \tag{4.19}$$

with μ_0 being the vacuum permeability. For currents on the order of 300 A, B_ϕ exceeds 0.2 T, with the field gradient ∂B_ϕ reaching values higher than 3000 T/m. An APL can be described by the strength parameter $k = e(\partial B_\phi/\partial r)/(m_0\gamma c)$ and the thin-lens approximation yields a focal length of $f = 1/(kL)$ [96]. Due to the energy-dependence of k, electrons of higher (lower) energy experience a longer (shorter) focal length and larger (smaller) focal waists, assuming

a constant emittance for all energies [82]. Figure 4.6 shows a schematic drawing of a typical active plasma lens focusing concept.

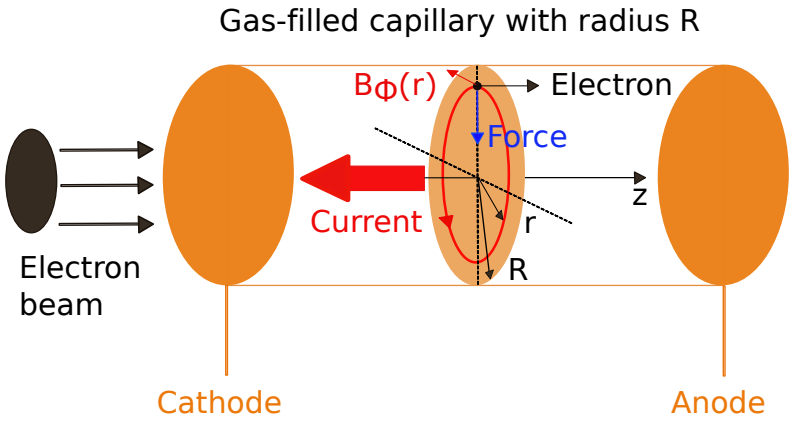

Figure 4.6: Schematic drawing of the focusing concept in an active plasma lens (adapted from [96]): a high voltage between anode and cathode results in the ignition of the gas in the capillary into a plasma. The resulting magnetic field B_ϕ from the traversing current can be derived from Ampère's law, resulting in a high field gradient and a focusing strength parameter $k \sim 1/\gamma$ with short focal lengths.

4.6 State-of-the-art all-optical Thomson sources

Up to date, several different approaches with the goal to produce X- or γ-rays in a compact setup have been presented and this section is dedicated to a short presentation of all-optical sources. A summary of their main parameters is given in table 4.1.

In [90], it is proposed to use a scattering foil positioned close to the exit of a gas jet where an intense femtosecond laser pulse drives a wakefield and accelerates electrons. This foil gets ionised by the rising edge of the laser pulse which results in a plasma mirror that reflects the laser pulse and therefore provides an inherent overlap in time and space with the relativistic electrons. The resulting X-ray spectrum is broadband due to the broadband electron distribution and a total photon number of $\sim 1 \times 10^8$ could be produced, covering the energy range from 50 keV to 200 keV.

Important characteristics of an X-ray source comprise energy tunability as well as a narrow bandwidth which is standard for synchrotrons but still a challenge for all-laser-based sources. In [97], they report on the production of quasi-monoenergetic ($\sim 50\,\%$ FWHM) and tuneable (~ 70 keV up to > 1 MeV) X-rays. Their setup consists of a high-power laser pulse which is divided into two parts, one to drive a wakefield and accelerate electrons and the second one for

the Thomson scattering process. The produced flux of 1.7×10^6 photons per shot was shown to be stable within 60 % of its average value, mainly dominated by the stability of the electron beam charge.

Another tuneable all-optical source is presented in [98] which is based on the combination of LWFA with a razor blade for shock-front injection to produce quasi-monochromatic electron beams and Thomson scattering. Depending on the chosen electron energy, the produced X-ray spectra peak at energies from 5 keV up to 42 keV with a bandwidth of $\sim$ 50 % FWHM.

Besides the production of X-rays in the keV-range, it is also possible to use Thomson scattering for the generation of more energetic γ-rays for e.g. astrophysics studies in the laboratory, as presented in [99]. The use of an ultrahigh-peak-power laser enables high-order multiphoton Thomson scattering (HMTS), in which multiple photons can scatter from a single electron and one single high-energy photon is emitted. The spectrum of the scattered photons covers a wide range due to high-order harmonic generation and field-strength-dependent red-shifting. In the presented setup, energies as high as 20 MeV could be reached, where the HMTS energies as well as the radiated power strongly depend on the incident electromagnetic field strength a_0.

Multi-MeV γ-ray beams from nonlinear relativistic Thomson scattering are also produced in the setup presented in [100] where ultrarelativistic laser-wakefield accelerated electron beams ($\gamma \sim 1100$) are produced. The resulting γ-rays have maximum energies on the order of 16-18 MeV and show narrow divergence (< 2.5 mrad) and a very high brightness of > 10^7 photons per laser shot.

In summary, all of the presented projects have not achieved the low X-ray bandwidth required for XFI-applications (max. 15 % FWHM $\approx$ 7 % σ [101]) and also the photon numbers per second have not reached the ideal value of $\sim 10^9$ yet.

Project	Energy	Bandwidth	Divergence [mrad]	Photon Number
ENSTA [90]	50 – 200 keV	large	18	10^8 in total
UNL 1 [97]	70 keV up to > 1 MeV	50 % FWHM	9	1.7×10^6 per shot
MPQ [98]	5 – 42 keV, 83 keV	$\sim$ 50 % FWHM	$\sim$10	$\sim 2 \times 10^4$ per shot
UNL 2 [99]	up to 20 MeV	n.a.	18 ± 2	n.a.
CLF [100]	up to 18 MeV	n.a.	< 2.5	> 10^7 per shot

Table 4.1: Main parameters of state-of-the-art all-optical Thomson X-ray sources. Given are the produced photon energy and bandwidth as well as the divergence and the photon number reached either per shot or in total. As one can see, the bandwidth of the currently existing sources is on the order of 50 % or even higher, making an optimisation for XFI-applications necessary.

5 Simulations and software

5.1 GEANT4

GEANT4 (GEometry ANd Tracking) is a powerful Monte Carlo toolkit for simulating the passage of particles through matter, including the processes of tracking, geometry, physics models and hits [102]. The software is a set of libraries, all written in C++, allowing the users to develop their own scenarios. Inspired by the needs of modern experiments, the software contains an event generator for different incident particles, detector simulation, reconstruction and analysis. In addition to the possibility to create individual geometrical models that can also be visualised, the GEANT4 framework provides a wide range of physical processes to model the behaviour of various particles.

5.1.1 General structure of a simulation

As it was discussed in section 2.6.2, a variety of semiconductor material effects that occur in measurements must be considered. While an ideal detector would only record the actual energy of incoming X-rays, in a real detector, not only photoabsorption but also other processes occur that result in a spectrum with different features. Since experiments always have to be predicted and validated with numerical calculations and simulations, it is necessary to consider such effects in the particle tracking framework GEANT4 as well [102]. Fortunately, such a class exists, namely the Sensitive Detector (SD) implementation [103]. Such a detector can be used to simulate the read-out of a detector by giving the user a handle to collect quantities such as the deposited energy, position and time information. A simplified illustration of a GEANT4 simulation and the necessary user actions, which will be explained in more detail in the following section, are shown in figures 5.1 and 5.2. If not stated otherwise, the information in this chapter was extracted from the GEANT4 user manual [104].

The GEANT4 toolkit does not provide the main program since its content varies according to the needs of a given simulation. Therefore, the main program has to be written by the user and

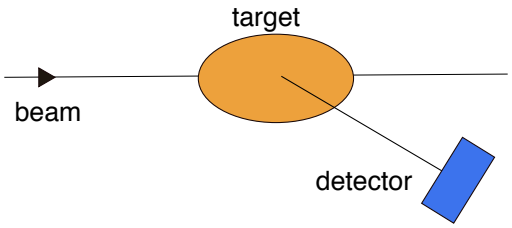

Figure 5.1: Simple illustration of the geometric arrangement in a GEANT4 simulation. The user always has to define the geometry of a target and a detector, and include the necessary physics processes in order to get an output.

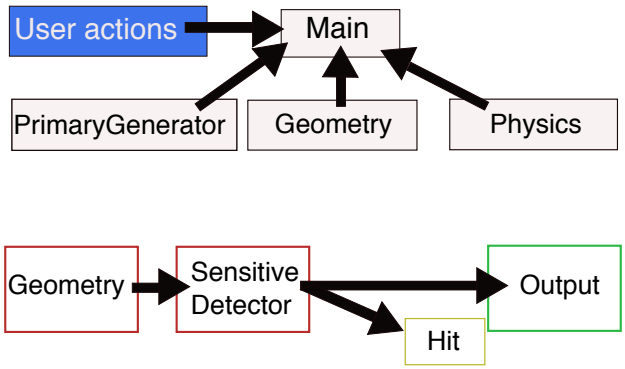

Figure 5.2: Simple diagram showing the necessary user actions to get an output of a Monte Carlo simulation

it is implemented by two toolkit classes. Main() has to create an instance of the G4RunManager class which controls the flow of the program and manages the event loops within a run. The run manager is responsible for initialisation procedures and it must be given all the information necessary to build the whole simulation, which includes

- detector description,
- physics processes,
- how the primary particles are produced and
- any additional requirements.

The detector description specifies the detector geometry and material and defines sensitive regions as well as readout schemes. The Logical Volume manages the information associated with detector elements represented by a given solid independently from its physical position in the detector. Physical Volumes on the other hand represent the spatial positioning of the volumes describing the detector elements. Sensitive Detector finally represents the parts of the

detector that will do the actual measurement, which is handled via logical volumes and the principal mandate of such a detector is the construction of hit objects using information from steps along the particle track.
In summary, the various stages during a simulation run are:

- Initialisation: detector description, physics processes selection and configuration
- Run: contains several events under the same conditions
- Event: generation and tracking of primary and final state particles

5.1.2 Physics processes and models

Within the GEANT4 toolkit, the distinction between a process, a particular initial and final state with a well-defined cross section or mean-life, and a model that implements the production of secondary particles, is made [102]. In general, processes describe how particles interact with a material and there are three basic types:

- At rest process (e.g. decay at rest)
- Continuous process (e.g. ionisation)
- Discrete process (e.g. Compton scattering)

This means that three different kinds of actions can be defined. Each action again defines two methods:

- One gives the step length from the current space-time point to the following one by calculating the probability of interaction based on the process' cross section information or
- one implements the actual action to be applied on the track, e.g. change of the particle's energy, momentum, direction and position.

Since a particle in a simulation proceeds in steps, it is necessary to find an unbiased way of choosing what either limits a step or to update the parameters for the following step. If one considers the interaction of a particle in flight, it is necessary to first calculate the distance to the point of interaction which is characterised by the mean free path λ. The probability of surviving a distance l is

$$P(l) = e^{-n_\lambda}, \tag{5.1}$$

where $n_\lambda = \int_0^l dl/\lambda(l)$. For the interaction of an isotope i of mass m_i that has the fraction x_i by mass in a material of density ρ, the cross section is σ_i and $1/\lambda = \rho \sum_i x_i \sigma_i / m_i$. It has to be noted that λ varies as the particle loses energy and that the probability distribution of n_λ is a simple exponential function, independent of material and energy. Therefore, at the point of production of the particle,

$$n_\lambda = -ln\,\eta, \tag{5.2}$$

where η is a uniformly distributed random number in the interval [0,1], used to determine the distance to the point of interaction in the present material. This information from all processes of the particle is then used to decide what actually happens, where each process is using a different random number. After each step Δx, n_λ is updated according to

$$n'_\lambda = n_\lambda - \frac{\Delta x}{\lambda(x)} \tag{5.3}$$

until the step originating from $s(x) = n_\lambda \cdot \lambda(x)$ is the shortest and the specific process is triggered.

With GEANT4, a number of different electromagnetic processes for various particle types and energies are available. The parameterised models for photon and electron processes are based on the exploitation of evaluated data libraries, EEDL (Evaluated Electrons Data Library) [105] and EPDL97 (Evaluated Photons Data Library) [106]. Those libraries provide data for the determination of cross sections and the sampling of the final state [107]. In the context of this thesis, the low energy electromagnetic library was used, based on the Livermore data library (livermore model) and on the Penelope2008 Monte Carlo code (penelope model). The recommended energy range of applicability for the livermore model ranges from 250 eV up to 100 GeV for all relevant effects such as Rayleigh scattering, Compton scattering, Photoelectric effect and Bremsstrahlung. The applicability energy range of the penelope model is given as 100 eV to 1 GeV. Different to the livermore model, also positrons are included and an even better low-energy description including atomic effects, fluorescence and Doppler broadening is provided. However, only the livermore model provides polarisation.

To make the process of decision making in a GEANT4 simulation more illustrative, a simple example setup is built. An incident X-ray beam of varying energy is passed through a water-filled box of 10 cm length, as shown in figure 5.3. The green lines indicate the tracks of 100 incident particles which start at the right edge of the box. In this scenario, an event is killed at

the first step of the incident particle, where it has either interacted within the box or has been transmitted through it. The absorption cross section of this photon process can be computed from the rate of unaltered transmitted particles and the result is compared to the cross sections which are used by GEANT4. Figure 5.4 shows the number of photons undergoing different physics processes at several energies for the livermore (a) and penelope (b) model. In table 5.1, the computed absorption coefficients are compared with the cross sections stored in the physics tables that are used by GEANT4. The good agreement between the calculated and tabulated values highlights the way GEANT4 decides between different processes and also the two different models produce very similar results.

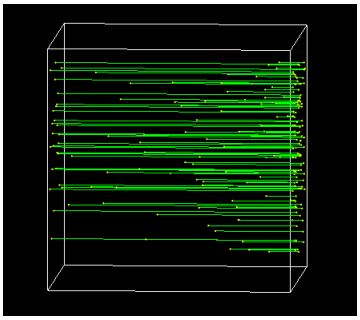

Figure 5.3: Simple simulation setup to study physics processes in GEANT4. The green lines show tracks of incident particles which start at the right edge of the box. After the first step of an incident particle, where it has either interacted within in the box or has been transmitted through it, the event is killed and the absorption cross section is computed from the rate of unaltered transmitted incident particles.

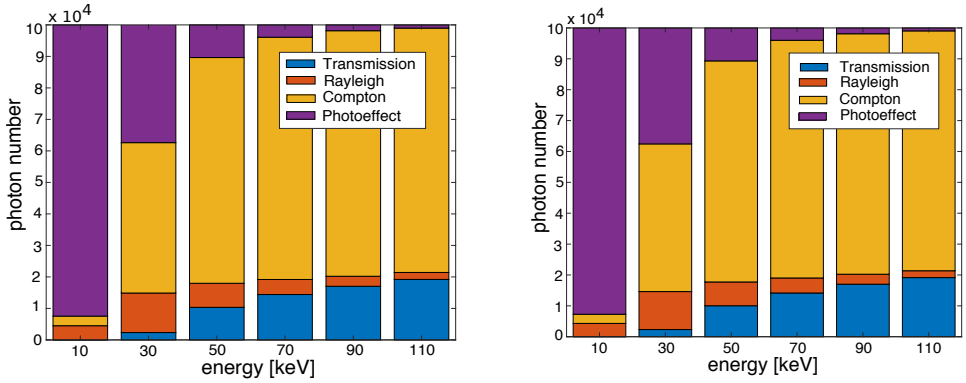

Figure 5.4: Physics processes calculated by GEANT4 for the two different low energy models livermore (a) and penelope (b). Shown are the numbers of photons undergoing different interaction events for 100 000 incident photons at several energies.

Model	Energy [keV]	$\sigma_{Rayleigh}$	$\sigma_{Compton}$	$\sigma_{Photoeffect}$	σ_{total}	$\sigma_{calculated}$	Ratio [%]
Livermore	30	4.6884	18.304	14.63	37.622	37.576	2.3233
Penelope	30	4.6926	18.54	14.569	37.801	37.623	2.2821
Livermore	50	1.9338	18.036	2.6761	22.646	22.687	10.387
Penelope	50	1.9344	18.164	2.7219	22.82	22.993	10.208
Livermore	70	1.0452	17.292	0.8786	19.221	19.374	14.63
Penelope	70	1.0454	17.415	0.8968	19.357	19.544	14.432
Livermore	90	0.6518	16.564	0.3850	17.6	17.701	17.204
Penelope	90	0.652	16.658	0.3911	17.701	17.711	17.032
Livermore	110	0.4443	15.879	0.2005	16.524	16.496	19.159
Penelope	110	0.4444	15.957	0.2018	16.603	16.533	19.008

Table 5.1: Comparison of calculated ($\sigma_{calculated}$) and tabulated cross sections for Rayleigh scattering ($\sigma_{Rayleigh}$), Compton scattering ($\sigma_{Compton}$), Photoeffect ($\sigma_{Photoeffect}$) and the sum of those three processes (σ_{total}) all given in [mm^2/g] for the two different low energy models livermore and penelope at different energies

5.1.3 Sensitive detectors

A step in a simulation has two points and also additional information of a particle such as the energy loss and the time-of-flight spent on the step. If a logical volume has a pointer to a sensitive detector, this volume becomes sensitive. A hit always represents a snapshot of the physical interaction of a track or an accumulation of interactions of tracks in the sensitive region of the detector. In GEANT4, a user-defined hit class can be created which can store various types of information, such as

- position and time of the step,
- momentum and energy of the track,
- energy deposition of the step,
- geometrical information,
- any combination of the examples listed above.

As soon as a sensitive detector is implemented and assigned to a logical volume of the detector geometry, the detector will become sensitive for each particle step if the step starts inside this logical volume.

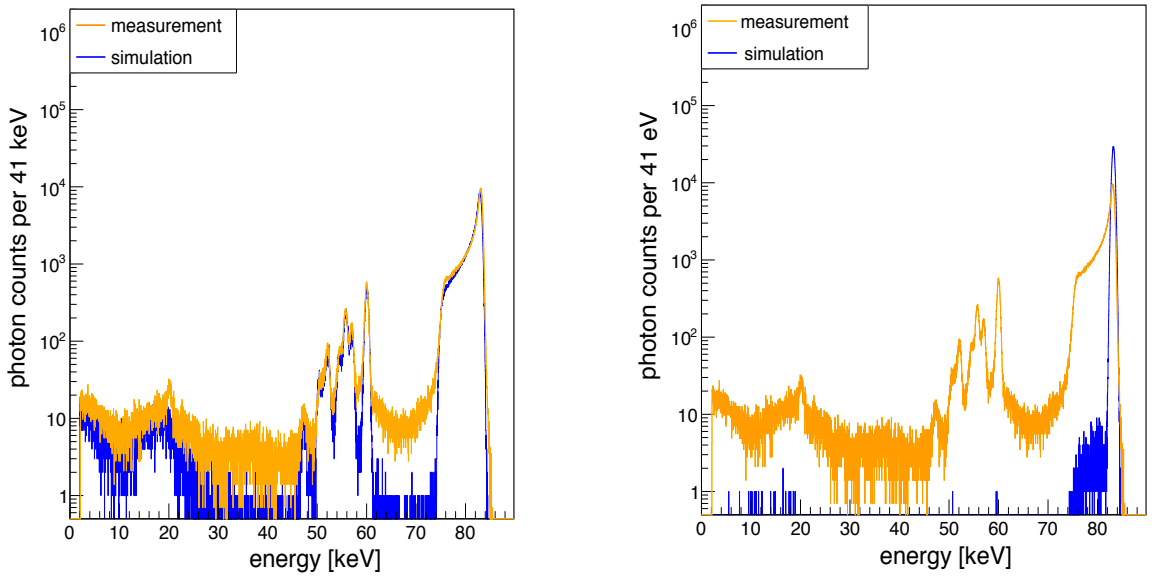

(a) (b)

Figure 5.5: Comparison between measurement (orange curve) and simulation (blue curve): the detector was positioned in the incident beam with an energy of 83 keV. The sensitive detector in (a) can model the photopeak shape but there still are deviations in the tail of the peak arising from scattering behind the detector chip. Nevertheless, these results match much better than simulations with an ideal detector (b) where the photopeak is Gaussian and does not show neither a tail, nor characteristic escape peaks arising from fluorescence processes inside the detector material.

The resulting spectra recorded by such sensitive detectors are much more realistic than those taken by ideal detectors. An example is shown in figure 5.5 (a) where a simulation with a sensitive detector is compared to a measurement at the P07-beamline of the PETRA III synchrotron at DESY. In both cases, the detector was positioned at the same distance from the source and the incident energy and photon flux were also matched. Figure 5.5 (b) on the other hand shows the same setup but with an ideal detector in the simulation. One can see that several effects such as hole tailing and the appearance of escape peaks are not correctly modelled, leading to a large discrepancy between experiment and simulation. Consequently, the sensitive detector module was used for all simulations presented in this thesis.

5.2 ROOT

The data analysis framework ROOT was developed in the context of the heavy ion experiment NA49 at CERN, which created a massive amount of data (around 10 Terabytes per run) [108]. Taking this situation as a chance, scientists developed and tested the next generation of data analysis methods in 1995, tailored to the specific needs of the experimental conditions. The resulting object-oriented framework aims at solving the data analysis challenges of high-energy physics but also of other fields and industries like big data processing, statistical analysis, visualisation and storage. It is mainly written in C++ but has been integrated with other languages such as Python and R in the meantime. Some of the most commonly used features amongst many others are: creating histograms and fitting them, 2D graphics and writing graphical user interfaces. In the context of this thesis, ROOT was used for the evaluation of simulation data produced by GEANT4, as well as for the analysis of experimental data and the following comparison to the simulated results.

5.3 MATLAB

MATLAB (MATrix LABoratory) is a multi-paradigm numerical computing environment and fourth-generation programming language [27]. A proprietary programming language developed by MathWorks, MATLAB, allows matrix manipulations, plotting of functions and data, implementation of algorithms, creation of graphical user interfaces (GUIs), and interfacing with programs written in other languages, including C, C++, Java, Fortran and Python. Built-in graphics make it easy to visualise and gain insights from data and a vast library of pre-built toolboxes offers algorithms for many different domains. MATLAB turned out to be a valuable tool at many different stages of this thesis and was therefore used in the form of GUIs during data taking and also for the later evaluation of experimental results.

6 Laser system and laboratories

6.1 Laser system

6.1.1 25 TW-class Ti:Sapphire laser system

One of the two preparation laboratories at the FLASHForward facility at DESY houses a 25 TW, 10 Hz, Titanium-Sapphire Chirped Pulse Amplification (CPA) laser system, which was built by Amplitude Technologies, France, and is capable of producing pulse durations of 25 fs. The concept of CPA was introduced by Strickland and Mourou in 1985 and won the Nobel Prize in Physics in 2018. As self-focusing of intense laser pulses limits the amplification of ultrashort pulses, in CPA, the initial short pulse from an oscillator is stretched to reduce its peak power [14]. The schematic in figure 6.1 shows a pair of gratings which disperses the spectrum and thereby stretches the pulse by a factor of a thousand. The resulting long pulse is amplified and recompressed by a double grating compressor. This method allows to produce high-energy, ultrashort pulses before self-focusing occurs.

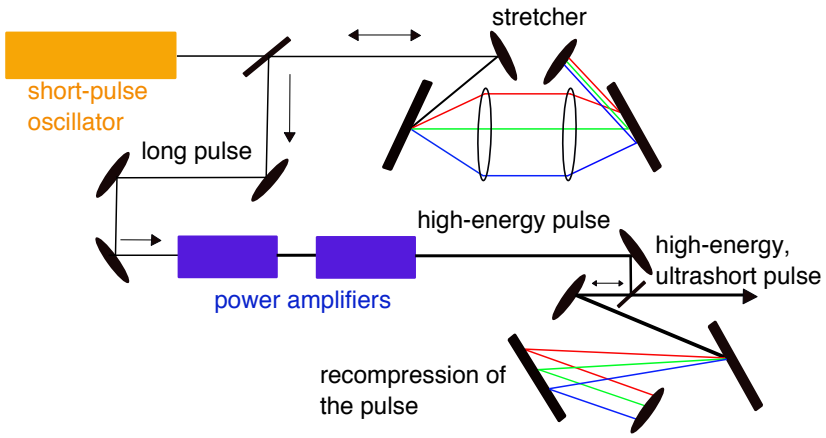

Figure 6.1: Schematic of a CPA laser system: an initial short-pulse from the oscillator is stretched by a pair of gratings before it gets amplified, which allows higher energies before self-focusing occurs. After the amplification, the pulse gets recompressed in a double grating compressor, resulting in a high-energy, ultrashort pulse.

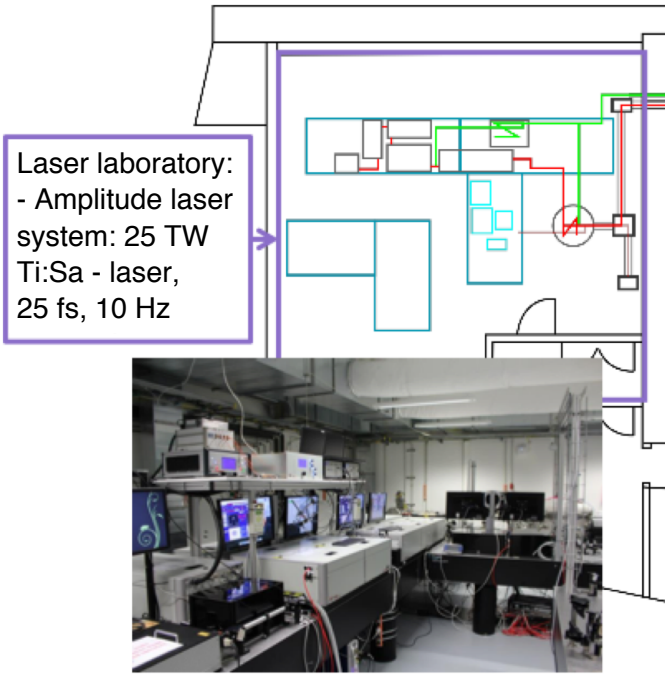

Figure 6.2: Schematic and picture of the laser laboratory housing the 25 TW system in the FLASHForward facility at DESY [110]

The Pulsar TW is a state-of-the-art high intensity laser for high field science, offering best-in-class performance with industrial-grade reliability in a compact footprint [109]. The pulse energy after vacuum compression was measured to be approximately 650 mJ and a secondary output of 3.5 mJ is compressed to 25 fs in order to allow an independent probe beam. A schematic and picture of the laser laboratory are given in figure 6.2 and tables 6.1 and 6.2 list the laser specifications for the main and secondary beam, respectively.

Energy per pulse	0.65 J
Pulse length	< 25 fs
Beam diameter	45 mm
Strehl ratio	0.7
Repetition rate	10 Hz
Contrast	$>10^9$
Peak power	>24.4 TW (assuming Gaussian temporal shape)

Table 6.1: Laser specification for the main beam

Energy per pulse	3.5 mJ
Pulse length	< 25 fs (5 fs with fibre compressor)
Beam diameter	10 mm
Repetition rate	10 Hz

Table 6.2: Laser specification for the secondary beam

6.1.2 Diagnostics

DAZZLER

In the context of ultrashort pulses it is often desirable to modify the shape of optical pulses with some kind of pulse shaper [111]. Dazzlers are pulse shaping systems, performing simultaneous and independent spectral phase and amplitude programming of ultrafast laser pulses [112]. A so-called AOPDF (Acousto-Optic Programmable Dispersive Filter) relies on a longitudinal interaction between a polychromatic acoustic wave and a polychromatic optical wave in the bulk of a birefringent crystal. The spectral phase control is as accurate as the material properties of the crystal are known, without any hypothesis or assumption, thus allowing users to fully trust the shaping characteristics. The Dazzler phase control is obtained through the control of group delays versus wavelength. The interaction between an optical wave and an acoustic wave also prevents the user from spectral phase discontinuities inherent to pulse shapers based on pixelated modulators. Dazzler systems can be inserted inside a CPA system to pre-compensate gain-narrowing and to compensate high order phase distortions, thus enabling the generation of shorter and cleaner ultrafast pulses. The combination of the Dazzler pulse shaping capabilities with the Wizzler high dynamic range measurement, as discussed in the following section 6.1.2, provides the most powerful compression optimisation tool.

WIZZLER

The Wizzler is a pulse measurement system designed to measure accurately the spectral phase of amplified ultra-short, near Fourier-transform limited laser pulses [113]. It is based on a pulse characterisation technique invented and patented by FASTLITE: Self-Referenced Spectral Interferometry (SRSI). It is single-beam, single-shot, and delivers both, spectral phase and amplitude measurements, i.e. the complete temporal characterisation of an ultrashort pulse. The Wizzler system is a standalone instrument with its hardware, implementing the optical setup that generates the SRSI signal and the spectrometer that records it, and its software, which extracts the pulse characterisation from the SRSI interferogram. In case a Dazzler pulse shaper is

integrated in the laser chain, the software also has the capability to send the phase information back to this device to perform pulse optimisation.

Fourier-Transform Spectral Interferometry

Fourier-Transform Spectral Interferometry (FTSI) is the treatment of the frequency-domain interference pattern between two pulses delayed in the time domain [114]. Inverse Fourier transform of the spectral interferogram results in a three-peak structure in which the oscillating term in the spectral domain, centred at the delay τ between the two pulses in the temporal domain, is numerically filtered. A Fourier transform convoluted with this filter provides information about the difference of the spectral phases and the product of the spectral intensities. Additionally, a similar treatment of the continuous term in the spectral domain, centred at delay 0 in the temporal domain, provides information about the sum of the spectral intensities. This enables the reconstruction of the two spectral amplitudes provided that the two spectral intensities do not overlap.

XPW effect

Cross-Polarized Wave Generation (XPW) is a third-order nonlinear effect. As its name suggests, it is the generation of a linearly polarised wave, orthogonally to the polarisation of a high-intensity linearly polarised input wave (see figure 6.3) [115]. Within the slowly-varying envelope, the undepleted regime and the thin crystal approximations, the XPW temporal amplitude is linked to the input temporal amplitude by

$$E_{XPW}(t) \propto |E_{IN}(t)|^2 \cdot E_{IN}(t). \tag{6.1}$$

As can be seen, the XPW effect acts like a temporal filter: an XPW generated pulse is a replica of the initial pulse, filtered by its own temporal intensity. Thus, it is expected to be shorter in time, i.e. to have a broader spectrum and a flatter spectral phase than the input pulse. This is true when the pulse is close enough to the Fourier transform limit, i.e. when the spectral phase is flat enough for the pulse to be filtered by the XPW effect. It is worth noting that the XPW generation is more sensitive to the chirp than to higher orders of the spectral phase, and that its efficiency vanishes for pulses chirped to above two times their Fourier transform limited pulse (FTL) duration.

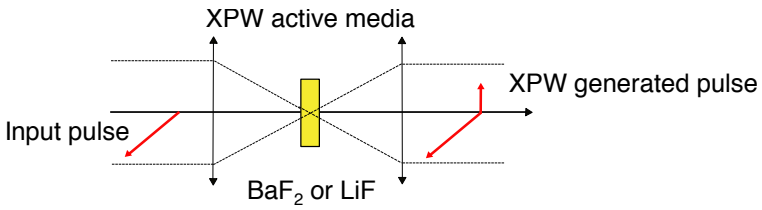

Figure 6.3: XPW generation resulting in a linearly polarised wave, orthogonal to the polarisation of a high-intensity linearly polarised input wave (taken and modified from [113]). The XPW effect can be used in ultrafast laser systems to achieve various pulse quality enhancements [116].

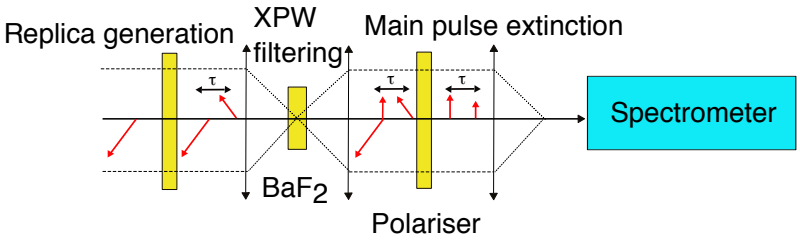

Figure 6.4: SRSI implementation in a Wizzler device (taken and modified from [113])

Self-Referenced Spectral Interferometry

The Wizzler measurement technique is called "Self-Referenced Spectral Interferometry (SRSI)" and its principle is described in figure 6.4. From the pulse to be measured, a replica is created with a linear polarisation different and delayed with respect to the input one. The main pulse is used to generate a reference pulse via XPW with a broader spectrum and a flatter spectral phase, but with the same carrier frequency. This reference pulse is created with the perpendicular polarisation, so that a polariser can transmit the XPW pulse and the replica to a spectrometer which records an interference signal. FTSI treatment is applied to this interferogram, and both spectral phase and spectral amplitude of the input pulse can be extracted, assuming that the spectral phase of the reference pulse Φ_1 is known. While Φ_1 is not perfectly flat, it can be set to 0 as a first approximation, and the algorithm shown on figure 6.5 improves the accuracy of the reference pulse phase value.

A screenshot of the Wizzler software in figure 6.6 shows an exemplary pulse optimisation. The actual input spectrum (white line), as well as the XPW spectrum (green dashed line), measured and fitted phases (red and green line, respectively) are shown in (a). A histogram of the optimised pulse with a FWHM duration of 31.1 ± 0.6 fs is shown in (b). This result was achieved after several feedback loops with the Dazzler device described in section 6.1.2.

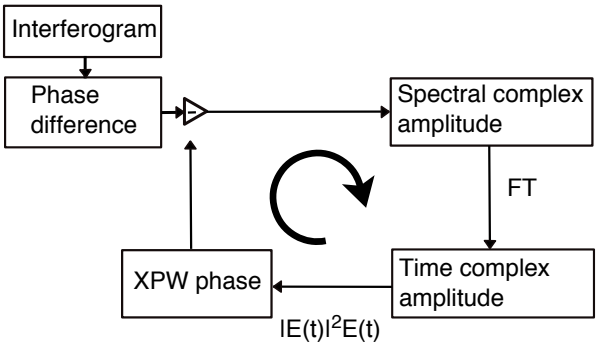

Figure 6.5: Algorithm loop to improve the accuracy of the XPW phase value (taken and modified from [113])

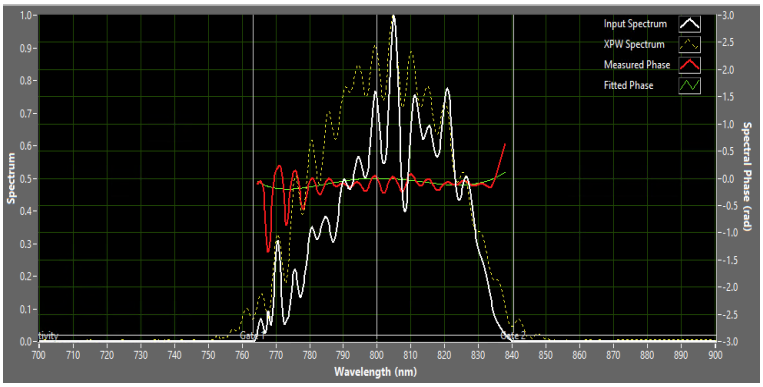

(a)

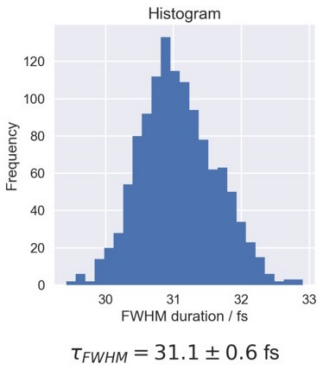

(b)

Figure 6.6: Screenshot of the Wizzler software to measure the spectral phase of an amplified pulse (a). After several feedback loops with the Dazzler, a FWHM duration of 31.1±0.6 fs could be achieved in this exemplary measurement (b).

6.2 Beam Optimisation and Novel Diagnostics (BOND) laboratory

The BOND (Beam Optimisation and Novel Diagnostics) [117] laboratory is designed to allow focusing of test beams from the high-intensity laser inside two experimental vacuum chambers. While the bigger of these two chambers houses the LWFA- and TS-setup, the smaller one, the ionisation test chamber, is used to characterise the ionisation and shaping of plasma targets which will later be used in the FLASHForward interaction chamber in the beamline. A schematic and a picture of the BOND laboratory are shown in figure 6.7.

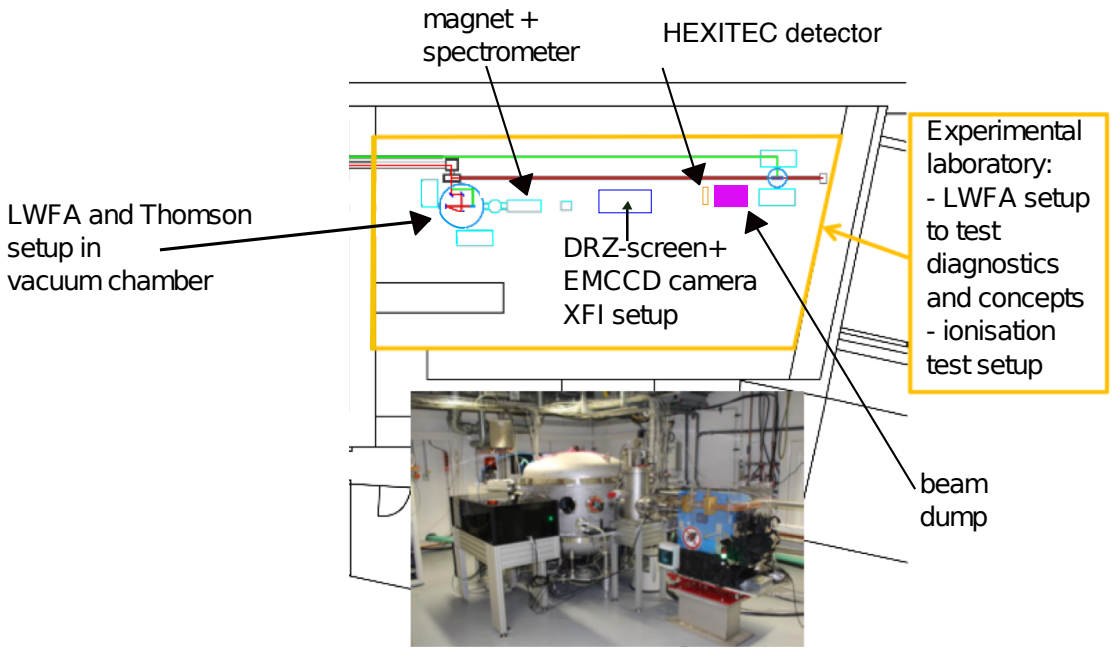

Figure 6.7: Schematic and picture of the BOND laboratory housing two vacuum chambers as well as various diagnostics for the laser, electron and X-ray beams (adapted from [110])

The big vacuum chamber is surrounded by various diagnostics for the laser beam (pre- and post-interaction) and the accelerated electrons which exit the chamber and first pass through a dark current monitor (DaMon) to measure electron charges. This device was developed to measure beam properties in a non-destructive way by detecting signals that are generated by the fields of charged beams. Therefore, a resonator made from stainless steel is used where the beam induces electromagnetic fields at certain modes. The TM01 mode, which is independent of the position of the electron beam but proportional to the charge, is detected by antennas inside of the resonator guided to electronics [118, 119]. The electrons are then deflected by a dipole magnet and their energy can be measured in a spectrometer where electrons with different energies reach different positions on a screen behind the magnet. This magnet has been characterised for currents ranging from 0 up to 311 Ampere using a Hall probe and the resulting scaling of the magnetic field strength with the applied current is shown in figure 6.8.

The X-rays produced in the Thomson scattering-process (TS) can pass all the diagnostics (see schematic setup in figure 7.1) and are in a first step directed onto a DRZ-screen that is imaged with an electron multiplying charge-coupled device (EMCCD) camera for a rough estimation of the photon numbers. The DRZ series [120] is a gadolinium oxysulfide (GOS)-based scintillator

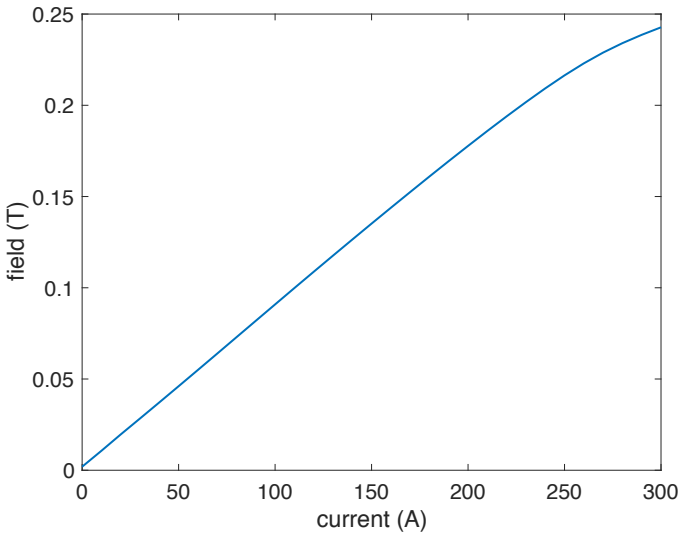

Figure 6.8: Magnetic field characterisation of the dipole magnet used in the BOND laboratory for currents ranging from 0 up to 311 Ampere

product used in the indirect conversion method of X-rays to light by irradiating the phosphor and reading the light as an image with a photodetector. When moving a stage to change the timing of the main laser beam in the vacuum chamber and simultaneously watching the number of counts seen by the camera, one can identify a clear peak of maximum photon production at the correct timing between the two laser beams. In the next step, the DRZ-screen as well as the camera are removed, and a semiconductor radiation detector is positioned in the direct beam path to measure the produced Thomson X-ray spectrum. The performance of the HEXITEC detector used for several direct spectrum measurements as well as for imaging runs will be described in the following section.

6.3 Measured performance of a HEXITEC detector

6.3.1 Charge sharing

The pixelated HEXITEC detector used for all measurements was provided by colleagues from the Rutherford Appleton Laboratory (RAL). In order to get a first impression of the detector and software functionality, measurements with radioactive sources were used. To cover the interesting energy range, ^{241}Am with a decay at 59.5 keV, having an activity of approximately 348 MBq at the time of operation, was chosen. The source was positioned directly in front of the sensitive

detector area of 4 cm^2. One has the option to either measure with a thin Al-window in front of the chip or remove it, which did not make a difference in these measurements since the emitted X-Ray energies were high enough to penetrate the aluminium.

The first measurements were done with the ^{241}Am-source and in order to test the different settings in the HEXITEC software, runs of 200 s duration were taken with different configurations. The HEXITEC system records the energy measured by every pixel in each frame of data which ensures that no information is lost in the raw data [121]. Using this data, different correction algorithms can be used to remove or recover energy deposited by charge sharing events, which are charge sharing discrimination (CSD) and charge sharing addition (CSA). In both algorithms, each frame of data is inspected for multiple events that occur in neighbouring pixels, and which are labelled as shared event. While in the CSD algorithm these events are removed and not included in the processed spectra, the CSA algorithm sums together the energies of the individual components of a shared event and assigns it to the pixel that originally received the largest proportion of the energy [121].

First, a baseline measurement without any charge sharing mode activated was taken, which shows a significant amount of noise in the low energy region of the spectrum and a plateau starting at the 59.5 keV photopeak of americium. Since each single pixel only detected a very low number of hits, the sum spectrum of all 6400 pixels was used to analyse the different configurations. Next, charge sharing discrimination was activated, leading to a spectrum with the majority of low energy events removed and also a reduced number of events in the photopeak tail. With this algorithm activated, the total number of counts in the spectrum is reduced but the remaining peaks show an improved energy resolution compared to the baseline measurement. With the third option, charge sharing addition, the resulting spectra suffer from a reduction of energy resolution due to an increase in noise and errors in the addition process [122]. Figure 6.9 shows the spectra resulting from all three different options starting with no charge sharing algorithm and followed by charge sharing discrimination and addition. Due to the fact that charge sharing discrimination yields the best energy resolution, as discussed in more detail in the following section, this option was chosen to be the most appropriate one for the Thomson spectrum and XFI-measurements.

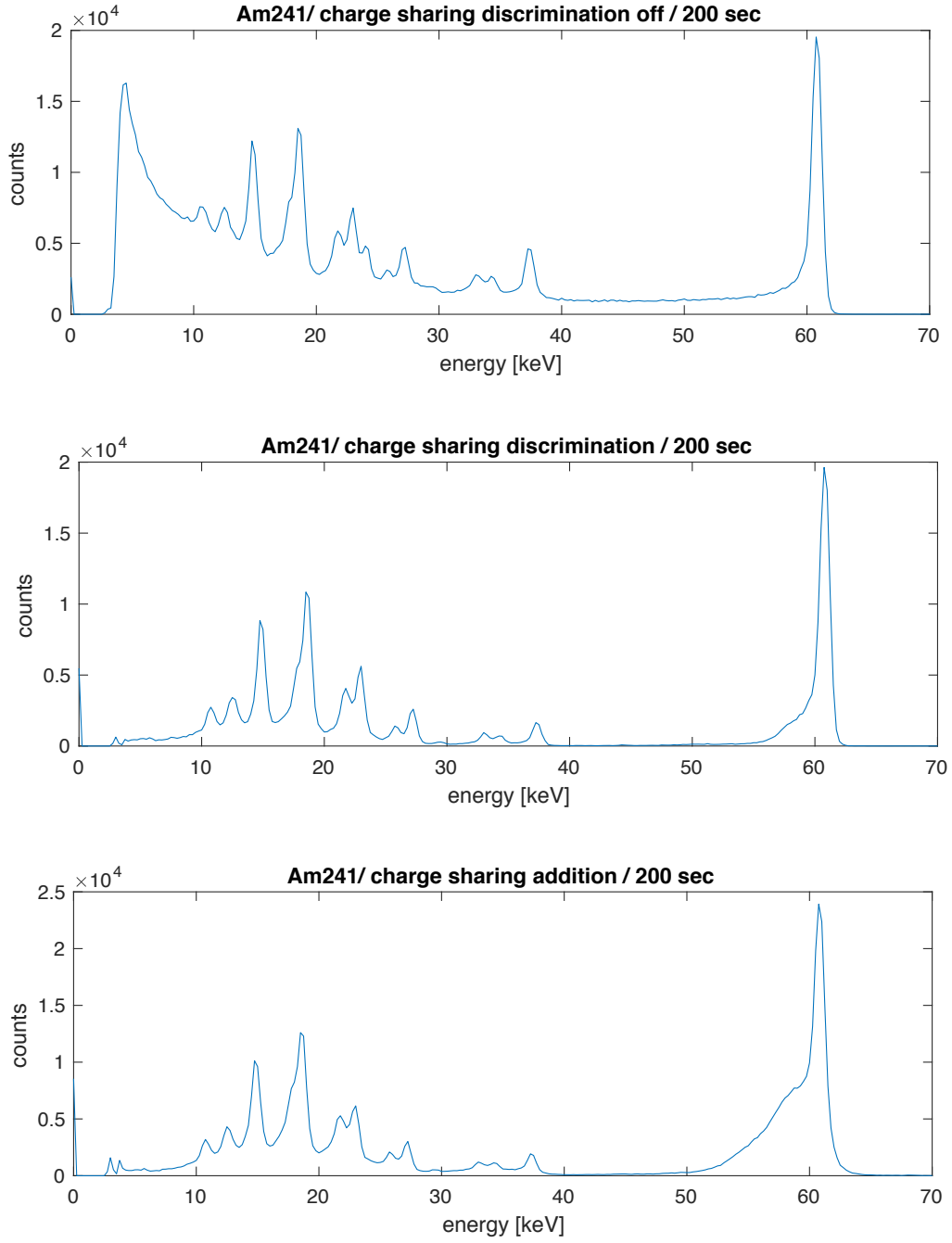

Figure 6.9: Recorded ^{241}Am-spectra with different charge sharing compensation options starting from no algorithm activated (top), charge sharing discrimination (middle) and charge sharing addition (bottom).

6.3.2 Energy resolution and calibration

The calibration process of a pixelated detector means more effort than comparable procedures for detectors with only a single pixel as each pixel on the grid delivers its own spectrum and consequently has to be calibrated individually. In order to assign the detector output to a specific energy, it is necessary to fit peaks of known energies in a recorded spectrum which can again be done with radioactive sources. To cover the majority of the recordable energy range of the detector (from 4 to 200 keV), ^{241}Am- and ^{57}Co-sources were chosen with emission lines at 59.54 keV and 122.06 keV, respectively. Furthermore, one can make use of the presence of fluorescence lines resulting from interactions with the detector materials, Cd and Te, which are present in all recorded spectra and offer reference points in the lower energy region. The according characteristic energies of Cd and Te that were used for the calibration are given in table 2.3.

In the first step of the calibration algorithm, all selected peaks in the spectrum have to be found. Once all significant peaks are found, Gaussian functions are used to fit them and a polynomial of third order approximates the background in a region around the peaks. Due to an internal threshold, the peak positions differ from pixel to pixel, making it necessary to apply the fits in a rather wide range around the peaks. This threshold has the purpose to reduce dark current and therefore shifts the peak positions to higher or lower detector values. Usually, those thresholds should be taken before a measurement and not changed any more during data taking as they influence the energy calibration.

One parameter from the Gaussian fits applied to the peaks, the standard deviation (σ), can also be used to determine the energy resolution of the detector at certain energies. This standard deviation can be converted to the full width at half maximum value (FWHM) of the Gaussian with

$$\text{FWHM} = 2\sqrt{2\,ln\,2\sigma} \approx 2.355 \cdot \sigma. \tag{6.2}$$

The resulting energy resolution of the detector at the mean peak energy of ^{241}Am of 59.54 keV was therefore calculated to be 0.72 ± 0.12 keV with 96.8 % of all pixels having an energy resolution better than 1 keV. This is comparable to the performance of a HEXITEC detector reported in the literature [123]. At the energy of the ^{57}Co-peak of 122.06 keV, the energy resolution yields a higher value of 1.03 ± 0.2 keV with 97 % of all pixels having a better energy resolution than 1.5 keV. This worse energy resolution value at a higher energy is due to the Fano noise which dominates at energies higher than 60 keV and arises due to the statistics of the charge carrier

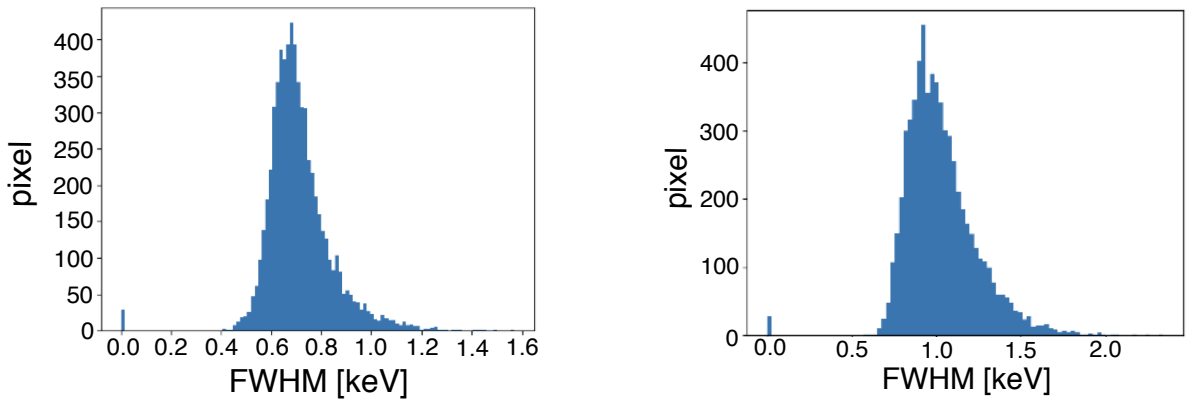

(a) (b)

Figure 6.10: Histogram showing the distribution of FWHM-values across all pixels at the ^{241}Am-peak energy of 59.54 keV (a). The energy resolution at this peak position was measured to be 0.72 ± 0.12 keV with 96.8 % of all pixels having an energy resolution better than 1 keV. In (b) the corresponding histogram for ^{57}Co with the main peak energy at 122.06 keV is shown. Here, the energy resolution was calculated to be 1.03 ± 0.2 keV with 97 % of all pixels having a better energy resolution than 1.5 keV.

generation [124]. Histograms showing the FWHM-values for all pixels are presented in figure 6.10 (a) for ^{241}Am and in (b) for ^{57}Co.

Another result of the calibration measurements is the finding that several pixels at the edges of the detector chip, as well as some pixels in the central area, are so-called dead pixels which show a high amount of noise and therefore have to be excluded in the analysis of recorded spectra. At the moment, the crystal growing process of CdTe is not as pure as for other materials, leading to defects and impurities especially at the edges and consequently resulting in worse conducting conditions due to the presence of many trapping sites and high leakage currents [125]. As all those factors deteriorate the detector performance, it is advisable to exclude such pixels in the calibration process which still leads to reasonable results since only 0.45 % of all pixels were identified to be erroneous ones in the used detector.

6.3.3 Efficiency

As already discussed in section 2.4, X-ray beams passing through a material get attenuated which is an important consideration in the performance of X-ray detectors. The sum of the probabilities for possible interaction processes in the material is described by the mass atten-

uation coefficient (μ/ρ) which is strongly energy dependent. In the energy region relevant for direct Thomson spectrum and XFI measurements, photoelectric interactions and Compton scattering are the most important processes. The total interaction probability in 1 mm CdTe between 0 and 200 keV is shown in figure 6.11. As one can see from the presented curve, the efficiency starts decreasing at 70 keV, making a correction of spectra recorded at higher energies necessary.

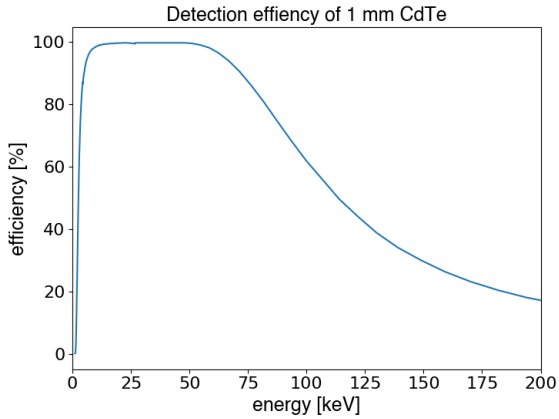

Figure 6.11: Detection efficiency of 1 mm CdTe between 1 and 200 keV computed from the NIST X-Ray mass attenuation coefficients for CdTe [26]

6.4 Plasma density measurements

In order to monitor some of the main process parameters in laser wakefield acceleration, the particle number density in the gas used as target medium and the free-electron density in the created plasma, real-time diagnostic tools have to be implemented. Either interferometric methods or optical emission spectroscopy, such as Stark broadening and Raman scattering, can be used. As the first option requires an appropriate optical line of sight through the sample, which is easy in case of a gas jet, interferometry was used in the experimental setup discussed in this thesis. Therefore, only the actually used interferometric method will be discussed here, while a detailed description of alternative approaches can be found in [126], where also the following information was extracted from. With interferometry, the density of a plasma is determined by measuring the phase shift acquired by a probe beam when passing through a sample relative to a known reference phase. The refractive index $\eta(n)$ of the sample is dependent on the particle number density n, with the refractivity $\eta(n) - 1$ actually being proportional to the particle number density n_g in a gas and of free electrons n_e in a plasma. The refractivity in an underdense

plasma is

$$\eta_e(n_e, \lambda) - 1 = -\frac{n_e e^2 \lambda^2}{8\pi^2 m_e \epsilon_0 c^2}, \tag{6.3}$$

with e the electron charge, m_e the electron rest mass, ϵ_0 the vacuum permittivity, λ the wavelength of the incident light and c the speed of light. The phase acquired by a light beam as it passes through a sample of length L is, in general,

$$\Phi = \frac{2\pi}{\lambda} \int_L \eta(l, \lambda) dl = \frac{2\pi}{\lambda} \times L \times \eta(\lambda), \tag{6.4}$$

where $\eta(\lambda)$ is the average refractive index along the geometrical path. Therefore, the acquired information is related to the line-integrated particle density from which the actual density has to be retrieved from. Under the assumption of a cylindrically symmetric sample, as for pulsed gas jets from circular nozzles, Abel inversion is used to extract the actual value of the radially dependent density from the line-integrated data along several chords [127]. The probe beam crosses the cylindrical plasma of radius R_0 perpendicular to the cylindrical axis and the smallest distance from the axis, R, can be measured. Several measurements with different distances R can be taken by either a parallel shift of the interferometer or with two probe beams. Figure 6.12 elucidates the geometry for reconstruction of the line-of-sight measurements with Abel inversion. The resulting phase change due to the shift position R is given by [128]

$$\phi(R) = \frac{2\pi}{\lambda n_c} \int_R^{R_0} \frac{n(r)}{\sqrt{r^2 - R^2}} r dr, \tag{6.5}$$

with λ being the wavelength of the probe beam and the cutoff density $n_c = \frac{4\pi^2 c^2 \epsilon_0 m_e}{\lambda^2 e^2}$. In a plasma of frequency ω_p, the refractive index given by $N = (1 - \frac{\omega_p^2}{\omega^2})^{1/2}$ is always less than one, decreases with increasing density and vanishes at n_c. For $n > n_c$, the displacement current due to the light wave is compensated by the electron current, and an incident wave is reflected [128]. Relation 6.5 can be inverted using Abel inversion to give the plasma density

$$n(r) = \frac{-\lambda n_c}{\pi^2} \int_r^{R_0} \frac{d\phi(R)}{dR} \frac{dR}{(\sqrt{R^2 - r^2})}. \tag{6.6}$$

A schematic of a typical configuration for plasma density measurements, a modified Mach-Zehnder interferometer, is given in figure 6.13. In contrast to conventional Mach-Zehnder setups, the laser beam is split after it has passed the interaction region and not already before. This offers the advantage of building the whole interferometry setup outside the vacuum chamber and therefore easing the alignment. Furthermore, this setup allows more control over the

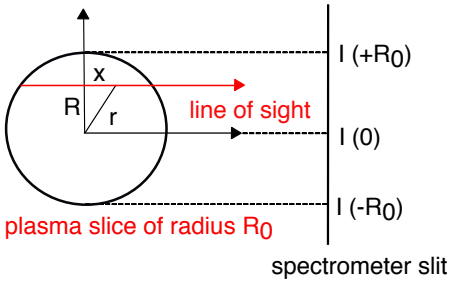

Figure 6.12: Schematic of Abel inversion geometry for reconstruction of the line-of-sight measurements (taken and modified from [129])

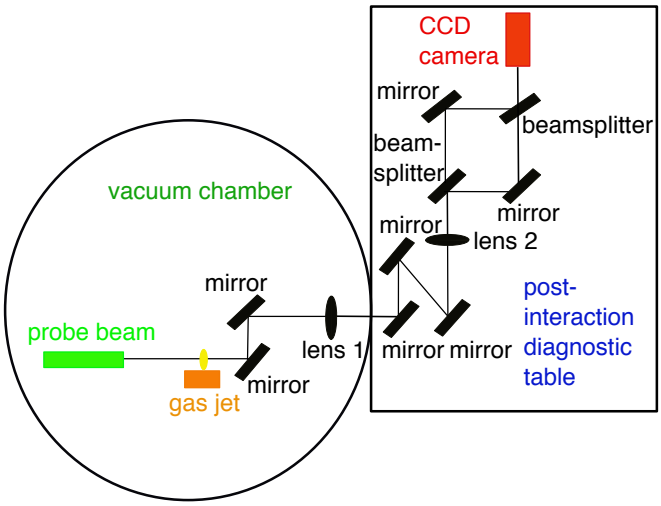

Figure 6.13: Schematic of a Mach-Zehnder interferometer setup for plasma density measurements in the BOND laboratory

fringe spacing and the orientation of the interferogram. After the first beamsplitter, the two replicas travel the same distance before they are reunited with the second beamsplitter. With the mirrors in both arms, the part of the laser beam with the phase-shift is made to overlap with the undisturbed part of the second beam, revealing the occurring phase changes when the probe beam propagates through the gas jet. The obtained interference patterns can then be converted into a map of the plasma density via inverse Abel transformation, as shown in equation 6.6.
An example of such a pattern recorded with a transverse probe diagnostic is shown in figure 6.14. In the first step, a Fourier filter is used to obtain the phase map from the interferogram, followed by Abel inversion to determine the plasma density, using the framework described in [130]. The resulting density map as well as the mean on-axis density profile are shown in figure 6.14 (b) and (c), respectively.

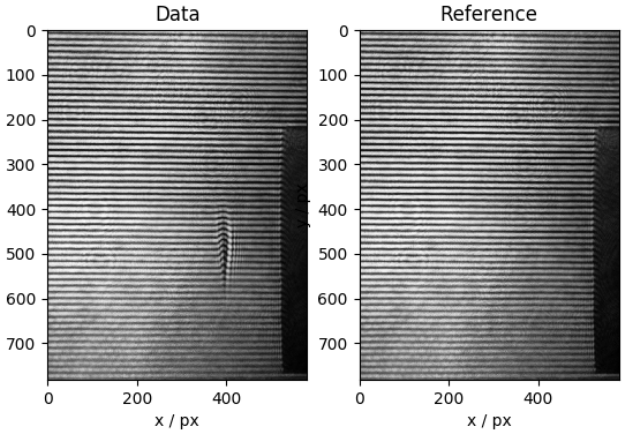

(a) Interferogram of a plasma channel and reference image where one pixel (px) = 7.58 µm

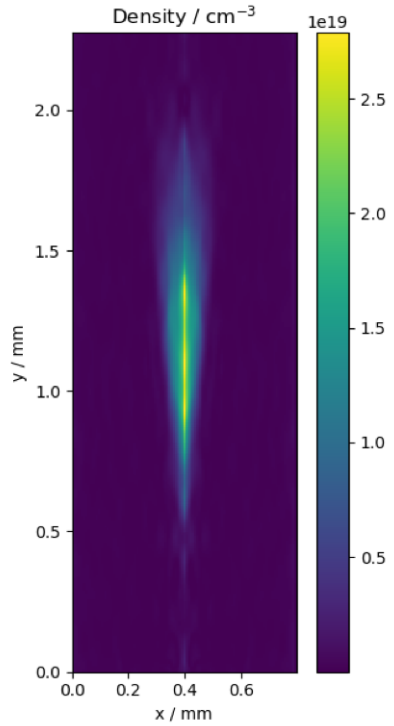

(b) Density map

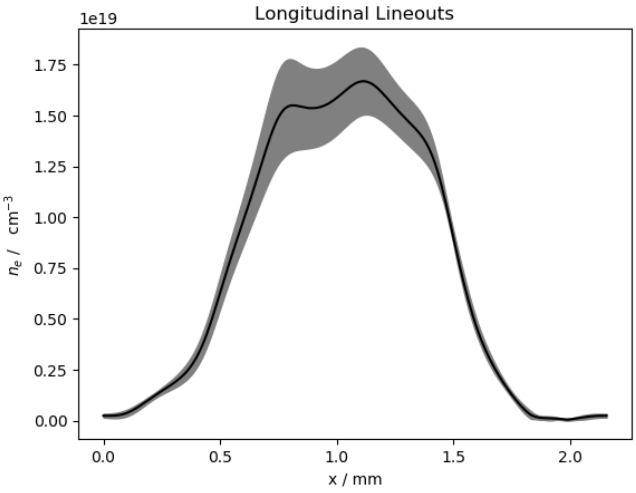

(c) On-axis plasma density

Figure 6.14: Interferogram and reference image of a modified Mach-Zehnder interferometer recorded with a CCD camera (a). The fringes show a constant phase-difference between the two laser beams and a shift in the fringes is visible above the centre of the nozzle in the left image, which corresponds to the density distribution of the gas jet. By the use of a Fourier filter, the phase map is obtained from the interferogram. Subsequent use of Abel inversion gives the density map (b) and the corresponding on-axis plasma density which is on the order of $10^{19}/\mathrm{cm}^3$(c).

7 Thomson signal and XFI measurements

7.1 Experimental setup

The experimental realisation of a laser-driven, all-optical Thomson X-ray source was done in the large vacuum chamber of the BOND laboratory right next to the laser laboratory housing the 25 TW system. A schematic drawing of the process is shown in figure 7.1 and a drawing of the actual setup in the chamber is given in figure 7.2. One significant advantage of such a source lies in the fact that only one high power laser is needed to drive both processes, the electron acceleration, as well as the Thomson scattering. As can be seen in both schematics, the incident laser pulse is split into two parts by a beamsplitter. The main pulse, containing two thirds of the total laser energy is then focused by an off-axis parabola onto the gas jet to drive a wakefield and accelerate electrons via laser wakefield acceleration (LWFA). The remaining part of the beam gets focused by a spherical mirror onto the accelerated electrons to induce the Thomson scattering process. As discussed in section 4.1, part of the electron energy is then transferred to the laser photons, leading to the emission of X-rays in a forward cone. The resulting X-rays as well as the electrons then leave the vacuum chamber. The electrons pass through several diagnostics and the spectrometer (see section 6.2) while the X-rays leave the vacuum through an Al-window where they can be used for direct spectrum measurements or imaging applications. In order to enable a high laser repetition rate (up to 10 Hz), a differential pumping system was installed to keep the chamber pressure at reasonably low values. Note that several diagnostics in the chamber, used to measure the focal spot of the main beam and the scattering arm, as well as the probe beamline, are not shown in figure 7.2. The pulse duration of the main laser was measured to be (26.9±0.2) fs and (31.3±0.6) fs were measured for the Thomson laser after the beamsplitter. With the use of a spherical mirror the Thomson laser was focused to an astigmatic focus of 25 µm FWHM size and the resulting peak a_0 was 0.27. The angle between the electron and Thomson laser axis was 7 °.

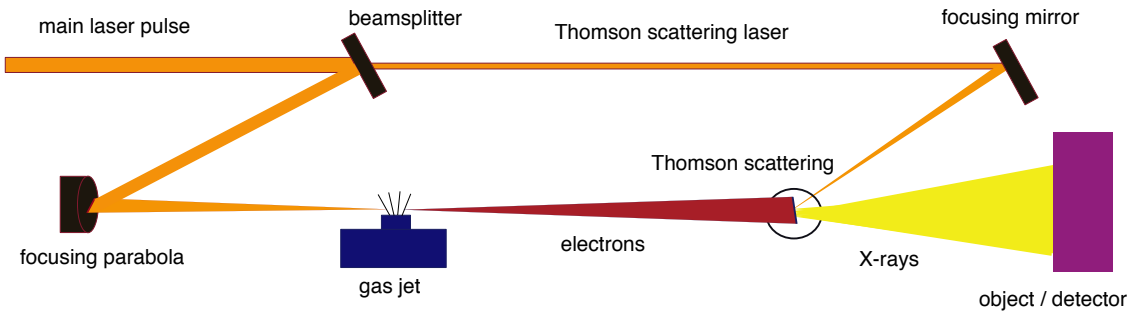

Figure 7.1: Schematic drawing of the Thomson scattering process. The main laser pulse is split into two parts by a beamsplitter which reflects two thirds of the total energy into the main beam and the remaining energy is transmitted into the scattering arm. The main laser beam is then focused with an off-axis parabola onto a gas jet to drive a wakefield and accelerate electrons up to energies of several tens of MeV. Meanwhile, the scattering laser is also focused onto the accelerated electrons, to induce the Thomson scattering process in which part of the electron energy is transferred to the laser photons. The resulting X-rays can then either be used for direct spectrum measurements or for imaging applications.

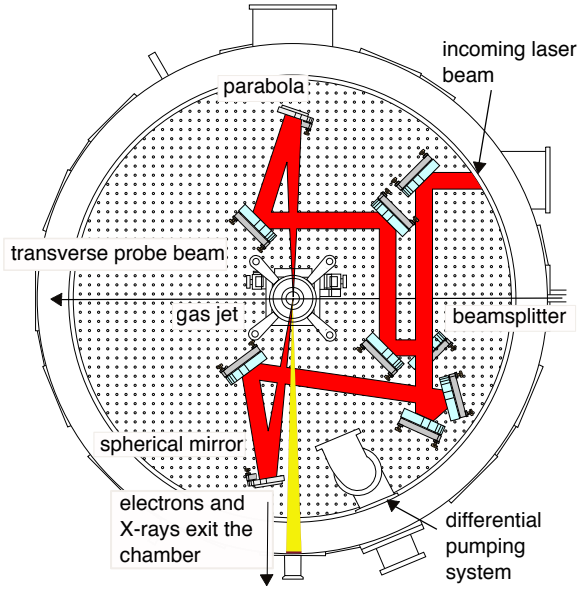

Figure 7.2: Schematic drawing of the Thomson scattering setup in the vacuum chamber with the same components as described in figure 7.1. The diagnostics for the focal spot of the main beam and the scattering laser are not shown in the schematic, as well as the probe beamline is missing. The differential pumping system indicated in the bottom right corner enables high laser repetition rates (adapted from [110]).

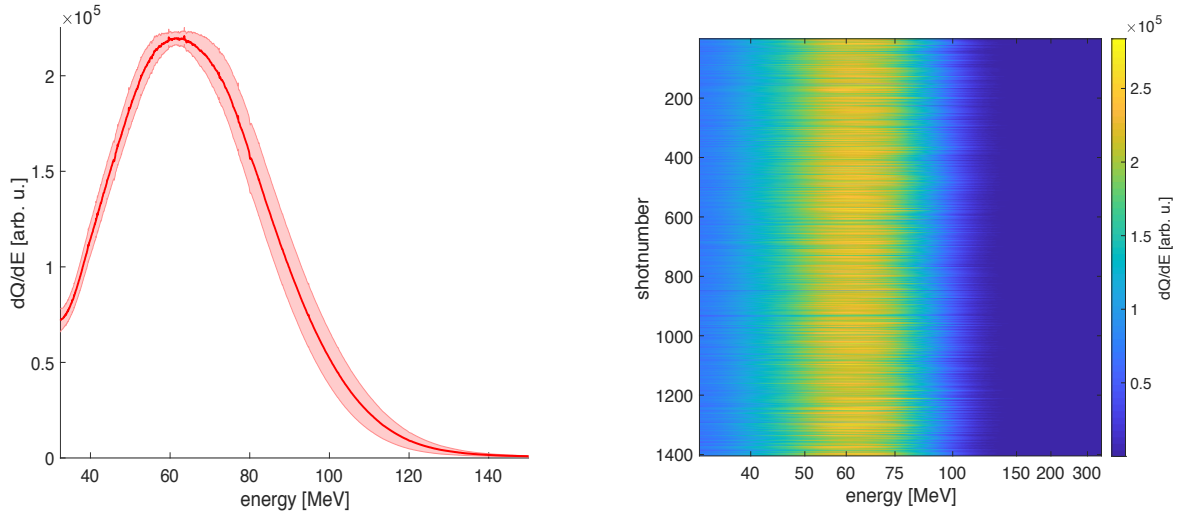

(a) (b)

Figure 7.3: Measured average electron spectrum for 60 % laser power with the laser firing at 1.4 Hz for 1000 seconds (a). The spectrum was fitted with a Gaussian function, yielding a mean energy of $\mu = (63.6 \pm 2)$ MeV with an energy spread of $\sigma = (20.7 \pm 1)$ MeV. The waterfall plot (b) clearly shows the electron stability during the run.

7.2 Measurement procedure

The very first step in the experimental process is to find a stable regime with electrons of constant energy and charge which comprises the tuning of several parameters. Here, the crucial factors are the plasma density determined by the backing pressure and the exact positioning of the gas jet, the laser power and the spectral phase of the laser which can be controlled with the Dazzler as described in section 6.1.2. The ideal parameters for the first, unoptimised setup were found to be a gas pressure of (3.0±0.1) bar for the gas mixture of 99.5 % He with a 0.5 %N_2 dopant. A laser power of 60 % which equals a laser energy between 250 and 300 mJ resulted in a mean electron energy of (63.6 ± 2) MeV with an energy spread of $\sigma = (20.7 \pm 1)$ MeV as shown in figure 7.3 and a mean charge of (16 ± 3) pC. The exact energy on target is unknown as the transmission of the laser beamline changed during the experiments. The relative stability of the laser energy was equal to 1.5 %. For the main laser, the FWHM spot size was 10 µm and the peak a_0 between 0.8 and 1, depending on the used laser power.

Once a stable acceleration regime has been established, scans to find the correct timing between the main and the scattering laser are started. Therefore, a stage in the vacuum chamber is moved to alter the length of the main laser beam and therefore the timing between both beams.

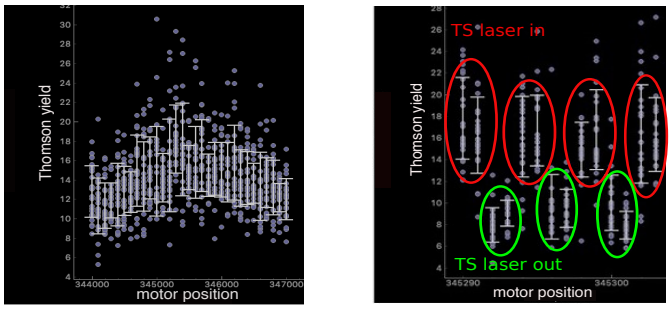

(a) (b)

Figure 7.4: Photons recorded by an EMCCD camera positioned at a 45 °-angle to a DRZ screen in the direct beam path. At each motor position, 25 shots are taken and the mean photon number with the corresponding errors is represented by the white bars. While moving a stage in the vacuum chamber to change the timing between the drive and the scattering laser, the number of recorded photons increases at the correct timing position (a). Blocking and unblocking the scattering laser arm after two series of shots at the motor position yielding the highest peak shows a clear difference in photon counts (b).

Meanwhile, the number of photon counts registered on a DRZ-screen imaged by an EMCCD - camera is recorded, as explained in section 6.2. At the correct timing position, one expects a higher number of detected photons, as exemplary shown in figure 7.4 (a), resulting in a peak structure around the respective motor position. After having determined the position with the highest number of registered photons, the stage is moved there and another check is done which consists of blocking and unblocking the scattering laser arm in regular intervals. The result shown in figure 7.4 (b) is another indicator that X-rays are produced in the setup, as there is a clear pattern with less counts without the TS laser and significantly more detected photons with the TS laser in. Having verified the presence of X-rays produced by the process of Thomson scattering, the next step is to measure the produced spectrum with a pixelated detector to determine the energy distribution as well as the number of produced photons.

7.3 Direct Thomson spectrum measurements

The measurements of the produced Thomson X-ray spectra are done with the pixelated HEXITEC detector described in sections 2.6.3 and 6.3.2. As it is only possible to measure a meaningful spectrum if not too many photons hit the sensitive detector area at the same time, it was necessary to position the device at a distance of 7.8 m from the source. Moving the detector closer leads to the effect that real events cannot be discriminated from charge shared ones any

more, producing an unphysical spectral shape. Furthermore, it was necessary to decrease the laser power to the point where electrons could still be accelerated but their charges had to be as low as 2 –3 pC to produce only a low number of Thomson photons in the scattering process and additionally decrease the amount of Bremsstrahlung background. The influence of the electron beam parameters such as the divergence on the recorded spectrum as discussed in section 4.2.2 is studied in detail in [131] where effective quantities are defined to provide a more suitable description of the spectral dependence. Taking into account the electron beam divergence of (12±5) mrad measured with the profile screen previous to the spectrum measurements, equation 4.1 has to be multiplied with a correction factor to calculate the peak of the Thomson spectrum with respect to the on-axis spectrum. According to experimental and simulation data presented in [131], a good approximation for this factor is 0.9, resulting in higher required electron energies to reach certain on-axis peak X-ray energies.

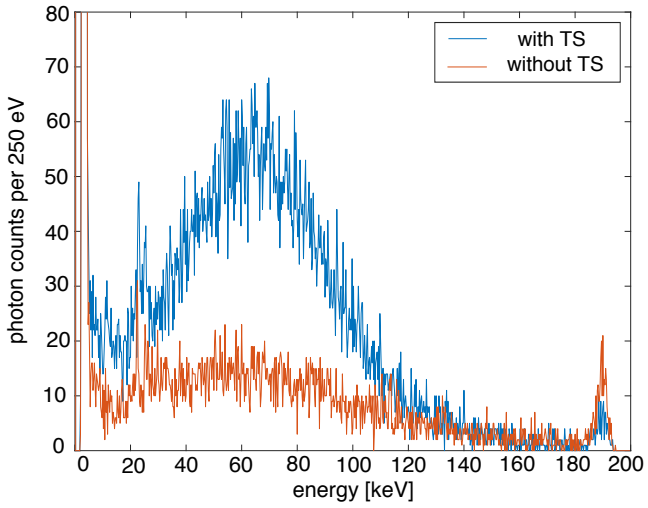

Figure 7.5: Spectra measured by the HEXITEC detector at a distance of 7.8 m from the interaction point. The blue curve shows the recorded spectrum with the Thomson laser beam in while the red curve shows the corresponding spectrum without the scattering laser.

In this configuration, spectra were recorded for five minutes with charge sharing discrimination activated. To get an estimation of the background originating from e.g. Bremsstrahlung of the electron beam, the same measurement was performed without the Thomson laser. The resulting recorded spectrum shown in figure 7.5 reveals a clear difference between those scenarios: with the Thomson laser, a spectrum with a clear peak around 66 keV is visible while

without this laser only background photons arising from Bremsstrahlung processes in the laboratory are recorded. Note that the spectra presented in figure 7.5 are not corrected neither for transmission in air and aluminium nor the quantum efficiency of the detector. Low energy X-rays are not measured due to filtering effects of the materials in front of the detector chip. At higher X-ray energies with a mean above 65 keV, the efficiency of the CdTe-chip starts decreasing. Both effects have to be considered to determine the actual mean incident photon energy as well as the produced photon number. Other effects include the fluorescence peaks from the detector materials Cd and Te at 23 and 27 keV as well as a high number of counts below 5 keV. These low-energetic counts arise from detector noise and the peak at 190 keV is the sum of all registered photon counts with energies higher than 200 keV that could not be resolved by the HEXITEC.

7.4 XFI-measurements with a laser-driven Thomson X-ray source

The first XFI-measurements were done with electron beams as described above, yielding a mean energy around 64 MeV and 16 pC charge. As the usual starting point, a timing scan as described in section 7.2 was done to find the Thomson signal and the thereby identified correct motor position was fixed.

XFI with gold nanoparticles

As Thomson scattering could be shown with the direct measurements presented in section 7.3, a 0.1 mm thick gold foil was positioned at a 45 °-angle with respect to the incident beam and at a distance of 6 cm to the HEXITEC, as shown in figure 7.6 (a), still at the far distance of 7.8 m from the source. Also here, one measurement was taken with the Thomson scattering laser in and another one with the scattering laser blocked, to prove that fluorescence is actually induced by Thomson scattering and not by background radiation arising from Bremsstrahlung and scattering processes in the laboratory. The resulting spectra with a measurement time of 10 minutes at a laser repetition rate of 1 Hz using charge sharing discrimination are shown in figure 7.6 (b). The clear difference once more proves that Thomson scattering was actually happening since only in the measurement with the scattering laser significant fluorescence peaks are visible.

The detector was then repositioned much closer to the source at a 90 °-angle with respect to the incident beam direction. A Plexiglass cylinder of 3 cm diameter and 6 cm height containing

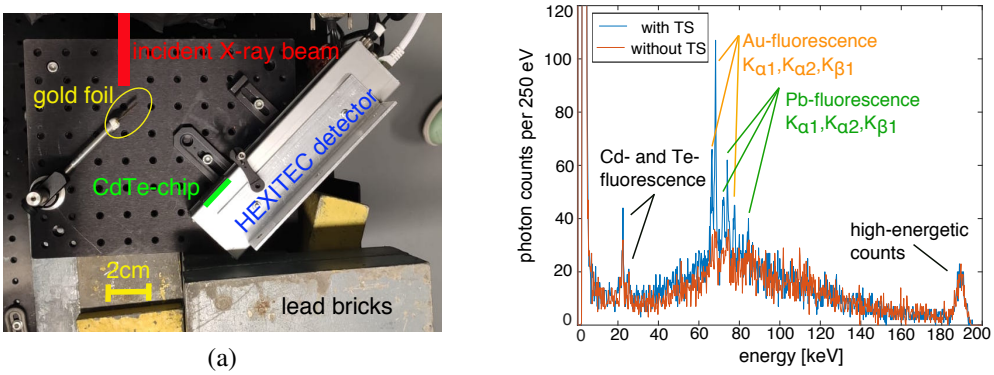

(a) (b)

Figure 7.6: (a) Experimental setup with a 0.1 mm thick gold foil positioned at a 45 °-angle with respect to the incident beam and at a distance of 6 cm to the HEXITEC. (b) Spectra recorded for 10 minutes at a laser repetition rate of 1 Hz, one with the Thomson scattering beam in (blue curve) and one without the second laser beam (red curve). The produced X-rays from the TS process have high enough energies to induce gold and lead fluorescence, resulting in the significant peaks between 67 and 75 keV. Without the scattering laser, only Bremsstrahlung can reach the gold foil and hardly any fluorescence photons are created and registered by the detector.

a small Eppendorf tube (0.3 ml volume) with a 10 mg/ml GNP solution, which will from now on be referred to as mouse target or phantom (see figure 7.7 (a)), was positioned 5.5 cm from the detector chip at a distance of 3.25 meters from the interaction point. Previous measurements and simulations showed the severe impact of Bremsstrahlung radiation due to the dumping of energetic electrons by a dipole magnet right in front of the XFI-setup. Thus, the lead shielding before and around the target was improved. The resulting spectra for a measurement time of 1000 seconds with the laser firing at 1.4 Hz is shown in figure 7.7 (b), where one was recorded with 10 mg/ml GNPs and the second one with water in the centre of the target. While in the signal spectrum one can see two fluorescence peaks at 67 and 69 keV, yielding a calculated significance of $Z = 5.4$, those peaks are not present any more in case of the water-scenario. Even though such a significance value would already account as sensitive enough to be detected in a medical application, it is reduced due to a lot of noise recorded from background photons. Those photons do not arise from scattering processes inside the target, but rather from Bremsstrahlung production in close proximity to the electron deflection by the dipole magnet. Therefore, the whole XFI-setup was shielded even better, resulting in an almost complete coverage, as shown in figure 7.8.

The mouse target was again put into the direct beam at a distance of 3.25 meters from the

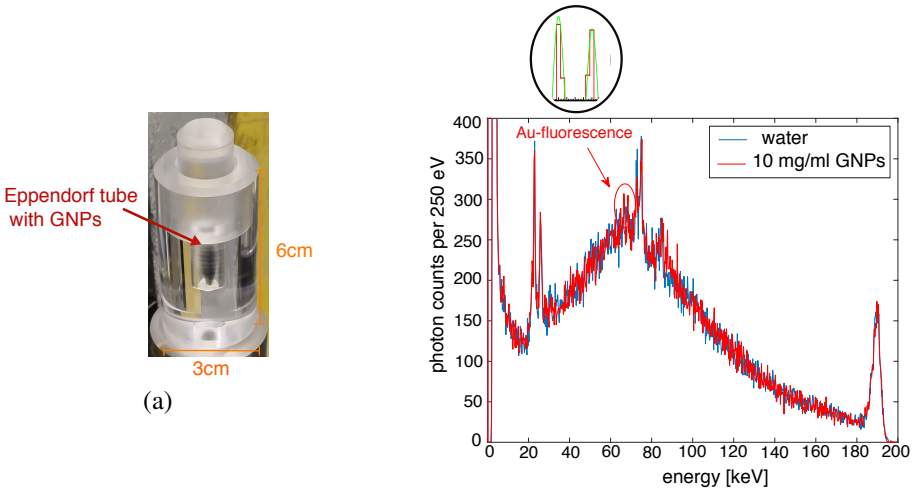

Figure 7.7: Picture of the 3 cm diameter and 6 cm height Plexiglass cylinder containing a small Eppendorf tube, referred to as mouse target or phantom (a). The plug on the top can be removed to replace the Eppendorf tube in the centre in order to vary the concentrations of the GNPs or to position tubes with different materials in the target. (b) Spectra measured with 60 % laser power firing at 1.4 Hz for 1000 seconds with the HEXITEC detector at a distance of 5.5 cm from the mouse target containing 10 mg/ml GNPs (red curve) or water (blue curve). The lack of Au-fluorescence peaks in the blue curve indicates that the X-ray production process is working.

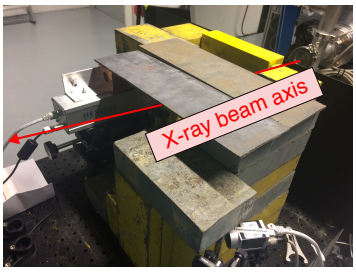

Figure 7.8: Improved lead shielding around the XFI-setup to reduce Bremsstrahlung radiation background arising from the deflection of electrons by the dipole magnet right next to the measurement table

source and 5.5 cm from the HEXITEC chip. The central part of the target was filled with a small Eppendorf tube, this time containing 18.87 mg/ml GNPs. The final spectrum recorded by the HEXITEC detector at an angle of 90 ° with respect to the incident beam and with the laser firing at 1.4 Hz for 1000 seconds is shown in figure 7.9 (a), where the Au-fluorescence peaks yield a significance of Z = 8.3 and the amount of Bremsstrahlung is less than in the previous spectra where the lead shielding was not as compact around the setup.

Even though it was possible to successfully demonstrate first XFI-measurements with GNPs irradiated by a laser-driven source, the incident parameters of the Thomson spectrum were not ideal. As the mean energy was around 75 keV and the bandwidth broad, as shown in the input spectrum in figure 7.9 (b), only a very small fraction of the incident photons was energetic enough to induce gold fluorescence processes. Increasing the mean energy would have meant major modifications of the whole setup and therefore it was decided to switch to a different fluorescence marker with a lower absorption edge instead, as discussed in the following section.

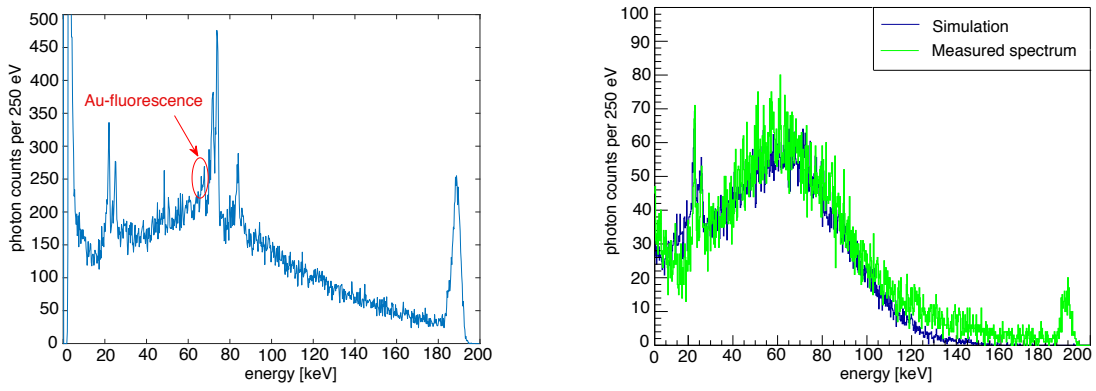

(a) (b)

Figure 7.9: Measured spectrum of the 18.87 mg/ml GNPs containing mouse target with the laser firing at 1.4 Hz for 1000 seconds (a). Compared to previous measurements with the mouse target, the number of background photons is reduced due to the improved lead shielding, consequently also leading to more dominant Pb-fluorescence peaks. Nevertheless, also the Au-fluorescence peaks are clearly visible, yielding a calculated significance value of Z = 8.3. The input spectrum shown in (b) was determined from measurements with less laser power and compared to simulations, showing a mean energy of 75 keV and a broad bandwidth of $\sigma \approx 30$ keV.

XFI with gadolinium solution

As it was not possible to achieve higher electron and consequently Thomson X-ray energies without major changes, it was decided to switch to a different fluorescence marker, namely Gadolinium (Gd). This element is commonly used as a contrast agent for MRI-measurements and has its K-absorption edge at 50.24 keV, so roughly 30 keV lower than gold. In order to induce as much fluorescence processes as possible, the incident energy spectrum should have a peak slightly above the absorption-edge energy which was already seen in direct Thomson spectrum measurements. Nevertheless, it is not possible to decrease the laser power too much as then no electrons are accelerated any more or the bunch charge becomes so low that hardly any Thomson photons are produced. The optimal shooting parameters (again determined by looking at the electron profile screen and spectrometer) were found to be 55% laser power and a backing pressure of (3.7 ± 0.1) bar. As the Gd-solution of 78 mg/ml concentration was only available in big Eppendorf tubes of 1 cm diameter, this tube was put directly into the beam path without any phantom surrounding it. The resulting recorded spectrum is shown in figure 7.10, where the laser was firing at 1.4 Hz for 1000 seconds. The Gd-fluorescence peaks at 42 and 43 keV (K_α) and at 49 keV (K_β) are clearly visible and yield a calculated significance value of Z = 32 for the K_α-lines.

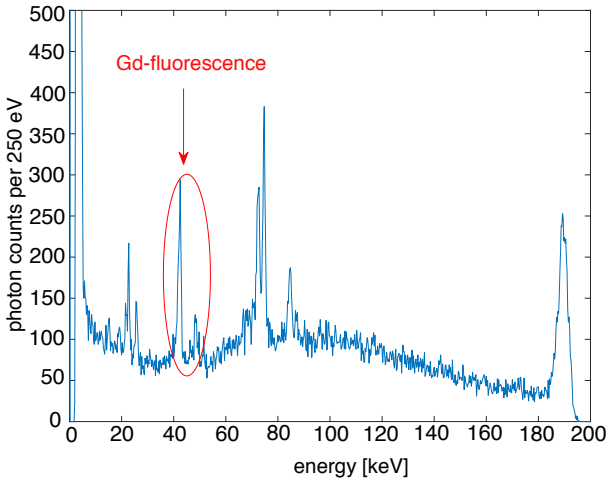

Figure 7.10: Spectrum measured with 55 % laser power firing at 1.4 Hz with the HEXITEC detector at a distance of 5.5 cm from the big Eppendorf tube containing 78 mg/ml Gd-solution. The spectrum was recorded for 1000 seconds at a gas pressure of (3.7 ± 0.1) bar. The Gd-fluorescence peaks at 42 and 43 keV (K_α) and at 49 keV (K_β) are clearly visible as way more incident photons are energetic enough to induce fluorescence processes in Gd with an absorption edge at 50.24 keV.

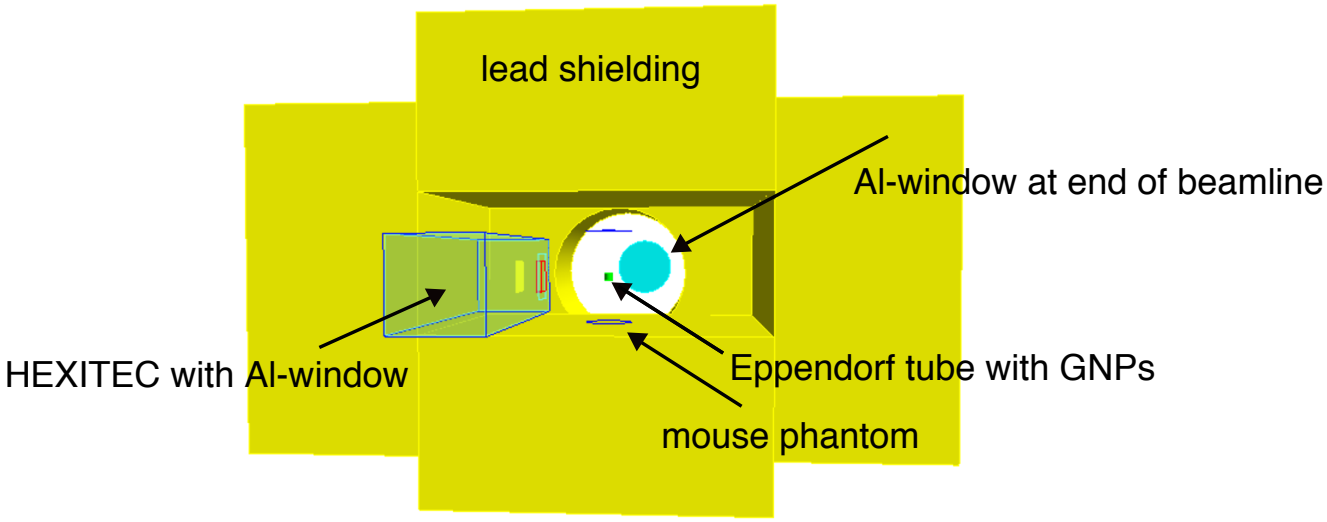

Figure 7.11: Screenshot of the GEANT4-setup for the XFI-simulations from the perspective of the incident photon beam. The yellow objects represent lead bricks surrounding the target which consists of a Plexiglass-cylinder with 3 cm diameter containing a small Eppendorf tube with a 18.87 mg/ml GNP solution. Only the outer parts of the cylinder are shown in blue while the Eppendorf tube with the gold particles is shown in green. The turquoise round object in the back represents the Al-window at the end of the beamline.

7.5 Simulations of the experimental setup

As usual in scientific practice, the experimental results have to be compared to simulations and numerical calculations. Therefore, GEANT4 simulations were performed with the goal to model the setup as realistically as possible. Nevertheless, in such a complex setup, it is hardly possible to consider all factors in detail such that deviations will always occur. The chosen scenario is the one with the 18.87 mg/ml GNPs containing mouse phantom at a distance of approximately 6 cm from the HEXITEC which was positioned at a 90 °-angle with respect to the incident beam. The input spectrum for the XFI-simulation was determined from the direct Thomson spectrum measurements with lower laser power (see figure 7.9 (b)). A lead coverage which was built in the laboratory to reduce the amount of Bremsstrahlung background was also rebuilt in the simulation and screenshots of the final construction can be seen in figure 7.11.

As already discussed in previous sections, charge sharing plays a major role in pixelated detectors. To make simulations comparable to measurements, it is therefore essential to implement the algorithm of charge sharing discrimination into them as well. The main parameters

such as the charge cloud size were determined in comparison with directly measured Thomson spectra. The difference with and without charge sharing discrimination is presented in figures 7.12 and 7.13. In both cases, experimentally measured direct Thomson spectra are compared to simulated ones. While in figure 7.12, the simulation was analysed without consideration of any charge sharing effects, the simulation spectrum in figure 7.13 used such an algorithm. The main difference lies in the height of the fluorescence peaks arising from processes in the detector chip itself. But also the total number of registered counts deviates by up to 80 %. Therefore, it is absolutely necessary to consider this detector effect, especially if the incident photon flux is not exactly known and simulations are used as an estimate for photon numbers.

Under the assumption of an empirically chosen charge cloud size of 70 µm, which is close to literature values [36], the number of registered photons in a directly measured, background-subtracted spectrum at 7.8 m distance is on the order of 6.7×10^3 per second. As photons are attenuated in air, the flux at the source can therefore be calculated to be about 8×10^3 photons per second in a representative direct spectrum measurement at very low electron charges of 2 – 3 pC per shot. Extrapolation of this value to higher charges and the applied measurement time and repetition rate yields a total incident photon flux on the order of 3×10^8, leading to a close agreement of measured and simulated spectra. In figure 7.14, two curves are shown, one for the measured spectrum with 18.87 mg/ml GNPs in the mouse phantom and one for the sum of the simulated XFI-scenario and the experimentally measured background. Apart from deviations in the height of the Pb-, Cd- and Te-fluorescence peaks, which can be explained with slightly different geometric arrangements and the modelling of the HEXITEC detector in the simulation under several assumptions, the agreement between both curves is good.

Another factor of great impact is the exact distance r between the target and the detector as the number of registered photons decreases according to the inverse square law with $\frac{1}{r^2}$. The approximate distance of 6 cm in the experiment was necessary to prevent the detector from standing in the incident beam but ideally it should be positioned closer to increase the number of detected photons. Also here, deviations between the experiment and simulation can arise as the detector positioning was done by hand and might slightly vary from the distances assumed in the simulated setup.

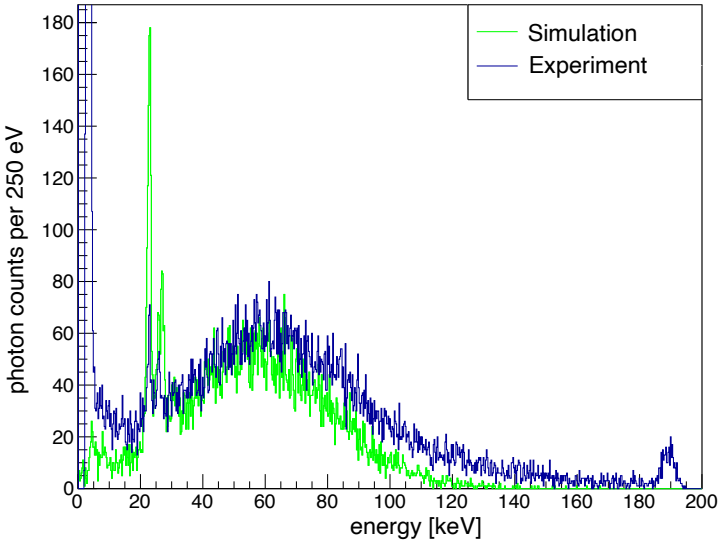

Figure 7.12: Comparison of experimentally measured (blue) and simulated (green) direct Thomson spectra. The simulation was analysed without consideration of charge sharing between pixels, leading to a higher number of fluorescence counts from the detector material and a wrong estimate of the total photon number used to scale the recorded spectrum.

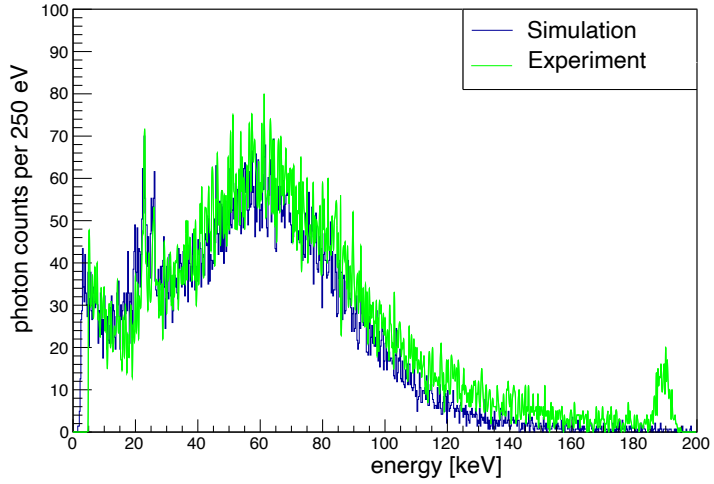

Figure 7.13: Comparison of experimentally measured (blue) and simulated (green) direct Thomson spectra. The simulation was analysed under consideration of charge sharing between pixels and the corresponding charge cloud expansion. Resultingly, the two spectra match significantly better.

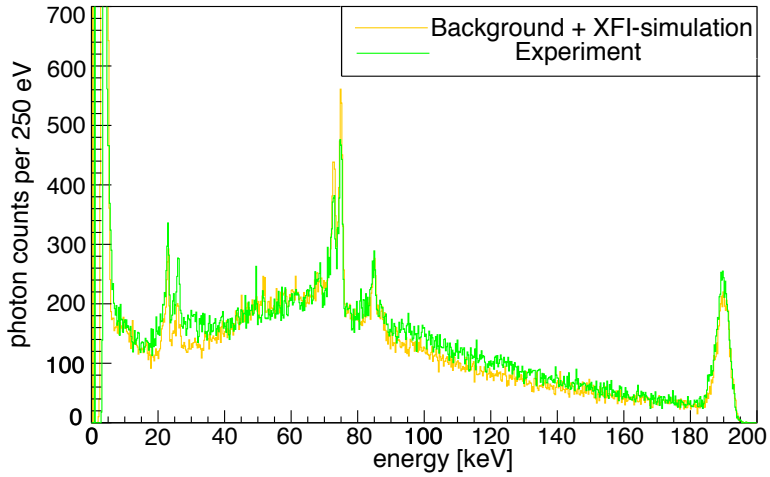

Figure 7.14: Experimentally measured XFI-spectrum for 18.87 mg/ml GNPs in the mouse phantom (green) and the sum of the simulated XFI-scenario and the experimentally measured background (yellow). In this simulation, the incident spectrum was approximated from direct spectrum measurements with $\mu = 75\,\text{keV}$ and $\sigma = 30\,\text{keV}$. The number of incident photons was $3\times\ 10^8$ in a 60 mm diameter beam with 10 mrad divergence.

7.6 Optimisation steps discussion

As the Thomson-XFI-measurements were done in a proof-of-principle experiment, the setup was in no way optimised to achieve results with high significances. Instead, the main focus was on the successful production of X-rays via Thomson scattering and the subsequent use of this radiation for an XFI-demonstration. Even though it was possible to measure fluorescence signals of different elements, the following parameters have to be improved for future measurements:

- **Incident Thomson spectrum**: the mean energy of the spectrum was at roughly 75 keV which is too low to induce fluorescence processes in gold atoms with the K-absorption edge at 80.72 keV. Furthermore, the bandwidth of the spectrum was large, on the order of $\sigma = 30\,\text{keV}$, which means unnecessary dose deposition in the phantom and a massive reduction of sensitivity. The ideal incident spectrum should have a mean X-ray energy around 90 keV and a maximum bandwidth of 15 % FWHM [101]. Methods to achieve these goals have already been developed and verified in simulations [82]. They rely on the implementation of an active plasma lens to reduce the bandwidth of the Thomson spectrum by reducing the electron divergence. They are also dependent on the use of chirped mirrors or e.g. a glass block to increase the interaction length between laser pho-

Energy	90 keV
Divergence	1 mrad
Number of photons	3×10^8
Beam diameter	1 mm

Table 7.1: Optimised source parameters for an XFI-scan of the mouse phantom containing 18.87 mg/ml GNPs in the original BOND laboratory setup

tons and electrons. Furthermore, the energy of the electrons colliding with the scattering laser pulse has to be increased by using a different nozzle (bigger diameter), different gas mixtures or injection mechanisms in the laser wakefield acceleration process.

- **Collimation of the X-ray beam**: so far, the X-ray beam hitting the phantom of investigation was only limited by the diameter of the beam pipe and the opening window in the lead shielding, both having a diameter of roughly 60 mm. Clearly, such a big beam diameter is only useful for a first scan if the overall presence of a fluorescence marker is investigated. For all consecutive measurements, it is necessary to collimate the beam, ideally to a pencil beam of 1 mm diameter as the resolution in XFI is only defined by this one parameter. The easiest method to achieve this goal is the design of a copper-collimator with the desired small inner diameter and a thickness of several cm to block all photons outside of the beam volume.

  An example XFI-spectrum for the very same setup as simulated in figure 7.14 with the optimised input parameters listed in table 7.1 is shown in figure 7.15. In comparison to the measured spectrum, the Au-fluorescence peaks in the simulated curve can be clearly separated from the Compton scattering background between 70 and 80 keV.

- **Shielding of the XFI-setup**: as Bremsstrahlung is a very dominant contributor to the total radiation present in the laboratory, it is essential to shield the experimental setup in a way that only the desired Thomson photons can reach the phantom and the detector. Ideally, the setup has to be positioned far from the electron beam dump where the majority of Bremsstrahlung production happens. This only works at the cost of flux reduction, making this option not very attractive. An alternative method is building a complete lead shielding around the setup with openings only at the beam entrance and exit. Even though different suitable materials exist, lead usually is the element of choice as it offers high stopping power for energetic radiation and its fluorescence lines can easily be separated from the gold lines as they lie several keV apart. Furthermore, a different beam dump

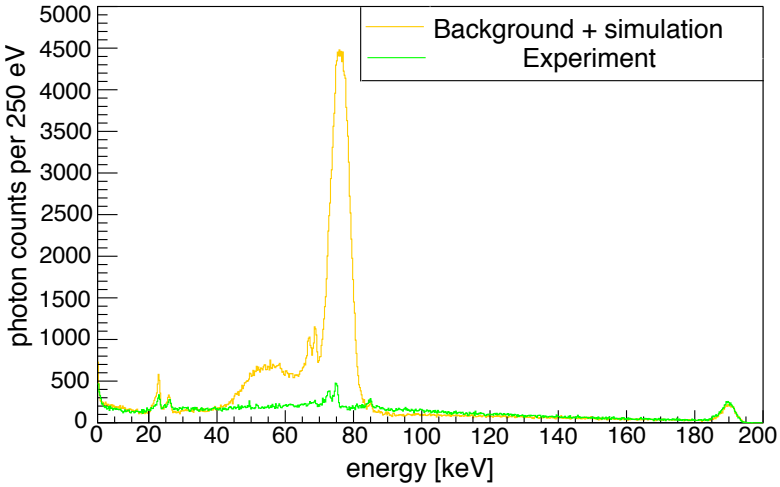

Figure 7.15: The green curve shows the experimentally measured XFI-spectrum for 18.87 mg/ml GNPs in the mouse phantom, while the yellow one is the sum of the simulated XFI-scenario and the experimentally measured background. In this simulation, a monochromatic incident spectrum of 90 keV energy was chosen. The number of incident photons was 3×10^8 in a 1 mm diameter beam with 1 mrad divergence.

design has to be considered since the electrons are only deflected into the ground and some lead bricks at the moment, enabling scattering in all directions.

- **Flux measurement**: a major uncertainty factor in the comparison of measurements with simulations is the number of produced Thomson photons. As the flux on the detector must not be too high in order to still extract a meaningful spectrum, it was not possible to directly measure the produced spectrum for electron charges higher than 2 –3 pC. But since the shape and the mean energy of the spectrum change with different laser powers, it is necessary to determine the exact incident spectrum and also the number of produced photons. Without further optimisation, it was only possible to measure the spectrum at low charges and extrapolate it to higher laser powers, which is only a rough estimate. Therefore, it would be desirable to obtain a more exact measurement method by e.g. placing a scintillator crystal into the beam or to use a spectroscopic detector that can cope with a high incident flux. Another option is to place filters made of dedicated materials right in front of the HEXITEC detector to attenuate the photon flux. By knowing the exact thickness of the filters and therefore the attenuation properties it would then be possible to calculate the original spectrum and photon numbers.

All of the factors listed above contribute to errors when comparing experimental to simulated data. As neither the beam diameter, nor the mean energy and energy spread of the incident spectrum are known exactly, the number of simulated photons might deviate from the experimentally produced flux. Also, the Bremsstrahlung background could not be simulated exactly so far as the laboratory consists of many single components that were not all rebuilt in the GEANT4-scenario. Nevertheless, the results from the simulations under several assumptions still agree well with the experimental data.

8 Optimised experiment

The first measurement campaign of X-ray fluorescence imaging with a laser-driven source, described in chapter 7, successfully demonstrated the applicability of novel accelerator technology for medical imaging purposes. Nevertheless, the parameters of the electron source and of the X-rays resulting from Thomson scattering did not meet the necessary requirements for XFI measurements with high significance levels yet. As the upper bandwidth limit for the novel imaging application was determined to be 15 % FWHM [101], one main improvement has to be the reduction of the effective electron bandwidth which results in a narrow bandwidth Thomson X-ray spectrum. To meet the desired properties, it is therefore necessary to modify the LWFA-setup and implement new devices such as an active plasma lens which has been studied in detail in [82]. Besides the desired bandwidth reduction, an APL also offers the possibility to produce X-ray spectra with different mean energies depending on the electron energy focused to the interaction region. For XFI, this property is highly beneficial as it enables the use of different fluorescence markers. While high-Z elements are necessary to scan big objects, lower-Z materials are suitable candidates for small-animal studies where the fluorescence photons do not have to penetrate a thick layer of tissue. Having an X-ray source which can provide energies over the whole range from 50 to 100 keV therefore significantly extends the diagnostic capabilities.

8.1 Modified experimental setup with an APL

The preparation of the Thomson scattering experiment with an active plasma lens (APL) started with the reconstruction of the whole LWFA-setup in the large vacuum chamber in the BOND laboratory. While the basic setup for the main laser beam used to drive a wakefield and accelerate electrons remained the same, the focal position of the parabola was moved downstream to accomodate the plasma lens. Right behind the gas jet with a 1 mm diameter de Laval nozzle, a newly designed active plasma lens was installed. It contains a capillary of 40 mm length and 2 mm diameter milled into sapphire. To keep the pressure in the vacuum chamber at tolerable values, it has a built-in differential pumping system on each side of the capillary consisting of 13 mm diameter in the sapphire block followed by a pumping line with 10 mm diameter. In

order to protect the holder from laser exposure, a ceramic plate with a 3 mm opening hole was additionally installed. Figure 8.1 shows the described APL from the front (a) and the back (b) where the sapphire milled capillary and the differential pumping connections are visible.

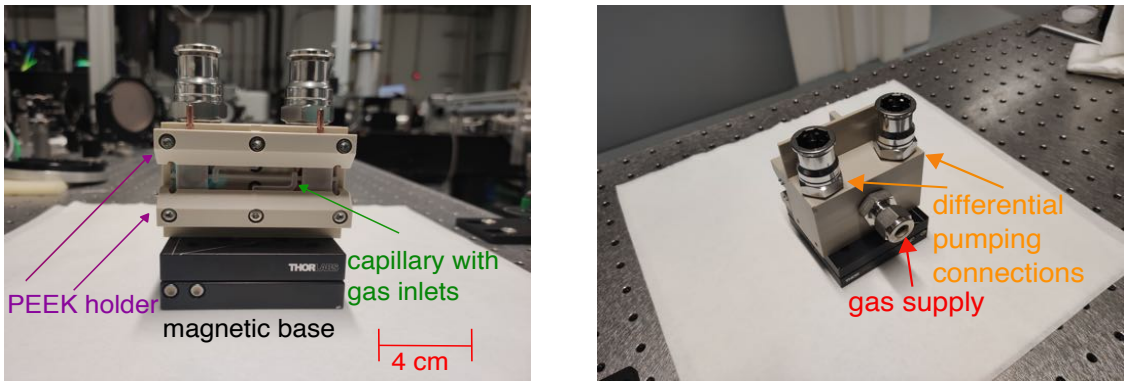

(a) (b)

Figure 8.1: Front view of the APL (a) with the 40 mm long capillary milled into sapphire and mounted in the holder made of PEEK (a thermoplastic polymer). In (b), the backside of the APL is shown where the connections for the differential pumping and the gas supply are located. To provide flexibility, the APL is bolted to a magnetic stage such that it can be removed easily from the setup without losing any references.

The setup of the second, scattering laser arm was also modified with the main goal to implement a focusing parabola as well. In the previous setup, a spherical mirror was used to focus the laser onto the accelerated electrons, but this resulted in spherical aberration and astigmatism and hence not a good focus quality. Therefore, a parabola of 500 mm focal length was also installed in the Thomson scattering laser arm. Due to the compactness of the setup, it is followed by a folding mirror to reach the required focal length distance and the resulting scattering angle is 10 °. Similar to the main laser arm, several mirrors before the parabola as well as the parabola itself are connected to picomotors to enable steering and optimisation also in a pumped state. A schematic drawing of the new setup, as well as a photograph of the actual setup in the vacuum chamber are presented in figure 8.2 (a) and (b), respectively. In addition to the basic components included in the schematic, figure 8.2 (b) also shows the various diagnostics for the focuses of the single laser beams and the differential pumping system to enable high repetition rates. A picture of the active plasma lens capillary filled with 95% argon and 5% hydrogen gas, which was chosen to achieve emittance preservation as discussed in [132], is shown in figure 8.2 (c).

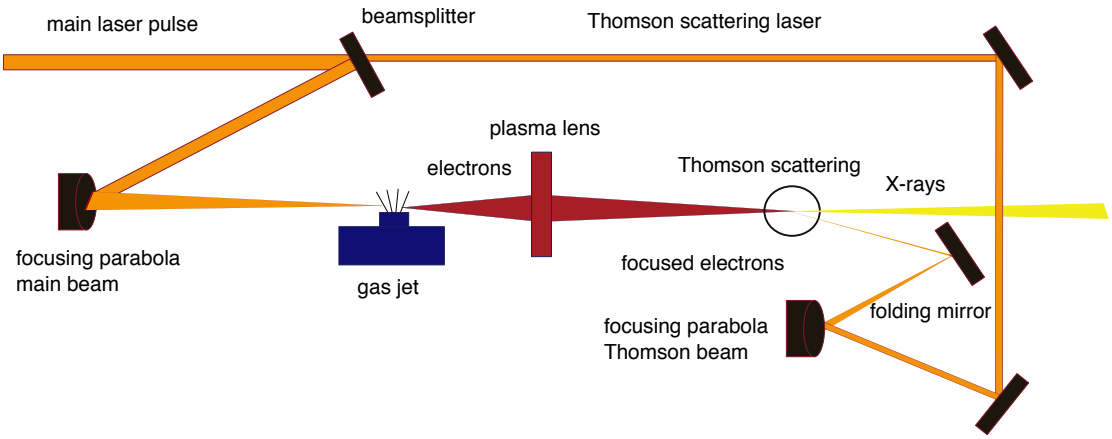

(a)

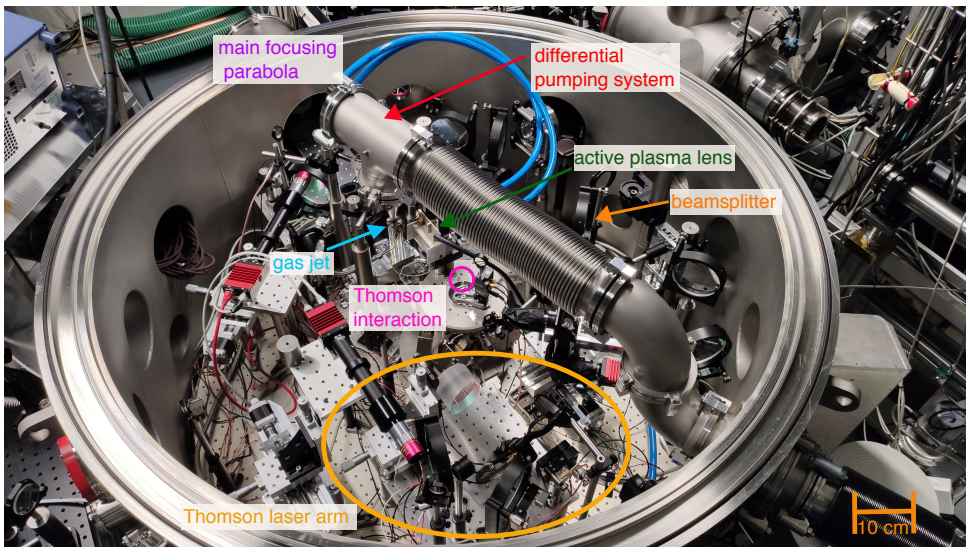

(b)

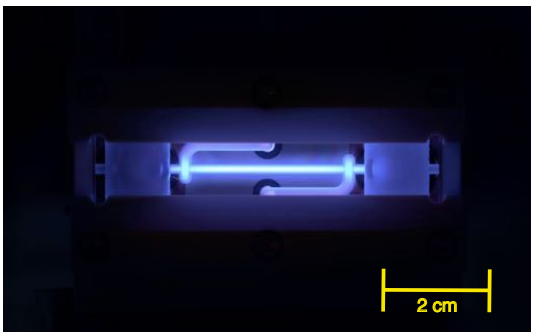

(c)

Figure 8.2: Schematic drawing of the Thomson scattering process with an active plasma lens (a). While the basic mechanism remains the same, the accelerated electrons are focused by the plasma lens before they interact with the scattering laser. A photograph of the actual setup in the vacuum chamber is shown in (b) where in addition to the components listed in the schematic, several diagnostics for the focuses as well as the temporal and spatial overlap are implemented. In (c), a picture of the active plasma lens capillary filled with argon gas is shown.

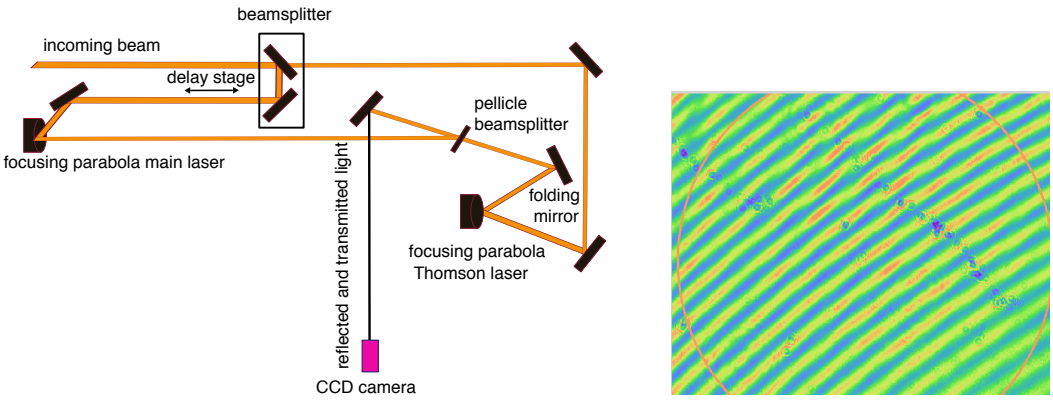

(a) (b)

Figure 8.3: Simple sketch of the diagnostic used for precise temporal overlap of the two laser beams. The transmitted and reflected beams from a pellicle beamsplitter are directed onto a CCD camera where strong contrast spatial fringes are only visible if the two beams are timed (b).

8.1.1 Temporal beam overlap

To ensure a highly precise temporal overlap of the two laser beams, a new diagnostic had to be designed since the probe beam cannot be used for timing purposes any more in the modified setup. It consists of a pellicle beamsplitter positioned at the focus of the Thomson scattering laser to transmit this pulse and reflect the main laser beam. The beamsplitter's angle has to be adjusted such that the reflected and transmitted beams are directed onto a camera to do spatial interferometry and hence time the beams. The electric field of two waves within the plane wave approximation is

$$E_1(\mathbf{r},t) = a_1 f(t) exp(-i\omega_1 t) exp(-i\mathbf{k_1 r}), \tag{8.1}$$

$$E_2(\mathbf{r},t) = a_2 f(t) exp(-i\omega_2 t) exp(-i\mathbf{k_2 r}), \tag{8.2}$$

with the amplitudes $a_{1,2}$, temporal shape $f(t)$, angular frequencies $\omega_{1,2}$, wavevectors $\mathbf{k_{1,2}}$ and the pulse duration $\tau = \tau_1 = \tau_2$ defined by the FWHM of the intensity profiles $I_{1,2}(\mathbf{r},t) = |E_{1,2}(\mathbf{r},t)|^2$ [133]. The intensity distribution of the total field in time and space gives a fringe pattern represented by $I(\mathbf{r},t) = |E_1 + E_2|^2$ which is only visible when the beams are superposed in time and space. In the presented setup, a delay stage is used to adjust the timing between the pulses such that an interference pattern is visible. Figure 8.3 (a) shows a simple sketch of the setup and in (b), a recorded camera image is shown where strong contrast fringes are visible, indicating that the two beams are timed.

8.1.2 Spatial beam overlap

To overlap the two beams not only in time but also in space, a second diagnostic was designed. On the same stage where the pellicle beamsplitter is mounted, a DRZ-screen was installed at the position of the Thomson laser focus. This screen is imaged by a vacuum-compatible camera and it can be moved into the Thomson laser beam axis as well. At this position, it is possible to image the Thomson laser focus as well as the focused electrons one after the other. By imaging the Thomson laser focus first and fixing this position with a region of interest on the camera, it is possible to steer the electrons to the same place in the second step. Moving the electron focus is possible by moving the hexapod where the APL is mounted on.

8.1.3 Measurement procedure with an APL

The very first steps in every LWFA-experiment consist in checking the laser beam alignment and the focus quality of the laser beams. In case of a Thomson scattering setup, the focal spot of the main laser and the scattering laser both have to be of good quality in order to enable highest intensities for the acceleration and later scattering process. Improving the focus quality is done by tweaking the mirror right in front of the parabola and the parabola itself. This method removes astigmatism from the focus. In case of a pulse front tilt being present, it is necessary to adjust the angle of the gratings in the vacuum compressor. The resulting focal spots show a diameter of 12 µm (FWHM). At this point it is also important to measure the laser pulse length with the Wizzler. In case of pulse lengths higher than 30 fs it is possible to use the feedback algorithm with the Dazzler to compress the pulse to lower values.

In the next step, the APL has to be aligned with respect to the main laser beam which is done with a reduced laser spot size. Using the hexapod, the capillary has to be positioned such that the laser can pass without any scattering. The ceramic plates on either end of the APL were designed to protect the capillary holder from laser damage from the main and Thomson beam while letting the electron beam pass through. For a start, the APL is then driven out of the beamline to find a stable regime of laser wakefield acceleration. Only if this point has been reached, the lens is moved to its assigned position without igniting the discharge. The electron beam pointing then has to be optimised such that the beams pass the APL without scattering and the charge registered by the DaMon gets maximised. At this point, the gas flow and the differential pumping are activated and the discharge can be triggered. The thereby focused electron transverse profile can be diagnosed on either the overlap screen, the profile screen located in the auxiliary chamber or the electron spectrometer.

Having found the optimal parameters for stable electron acceleration through the plasma lens, the spatial beam overlap has to be checked on the overlap screen. As described before, the Thomson laser focus is first imaged on a DRZ-screen and its position fixed by a region of interest on the camera. After blocking the Thomson beam, the focused electrons are steered into the very same region to achieve precise spatial overlap.
The temporal overlap of both beams is done already in low power such that no filters which would cause an additional time delay are needed. One has to keep in mind that the spatial and temporal beam overlap are done at slightly different positions which has to be compensated for. Other uncertainties arise from focusing imprecisions onto the overlap screen or the pellicle as well as from the thickness of the DRZ-screen. These possible deviations have to be kept in mind as they lead to a slightly different optimal timing position which can only be determined in scans over a wide area around the determined pellicle timing as described in section 7.2. Different to the first experiment without the APL it was not possible to detect a clear difference in photon counts between TS laser in and out due to the higher amount of Bremsstrahlung radiation relative to the produced Thomson photons. This background radiation is created by electrons which do not pass the APL perfectly centred but rather get dumped there and by unfocused electrons hitting the beamline.

Another means of maximising the recorded signal strength lies in optimising the spatial overlap of electrons and scattering laser. As mentioned above, the electron focus can be steered by moving the hexapod where the APL is located on. It is now possible to use this method while still recording photons with the EMCCD camera and observe the influence of hexapod position changes in terms of photon flux. Also here, charge fluctuations can be seen when electrons do not pass the APL centred any more but rather get dumped in it, leading to less recorded charge but at the same time more photon counts due to Bremsstrahlung. Maximising the Thomson yield was not possible due to high camera fluctuations which overrule potential Thomson yield changes. Consequently, it is necessary to find new methods to (a) perform meaningful on/off-scans and (b) maximise the Thomson yield by optimising the spatial overlap. The only way to verify the presence of X-rays produced by Thomson scattering is to use a spectroscopic detector at a large distance to the interaction point which is described in detail in section 8.3.

8.2 Electron parameters

Previous to the spectrum measurements, the electron pointing stability and divergence without the APL were measured with the profile screen, resulting in a divergence of (3.46 ± 0.51) mrad by (7.85 ± 1.36) mrad as shown in figure 8.4 (a). The pointing of the beams shown in (b) results in a standard deviation of 1.6 mrad in the horizontal axis and 0.9 mrad in the vertical axis.

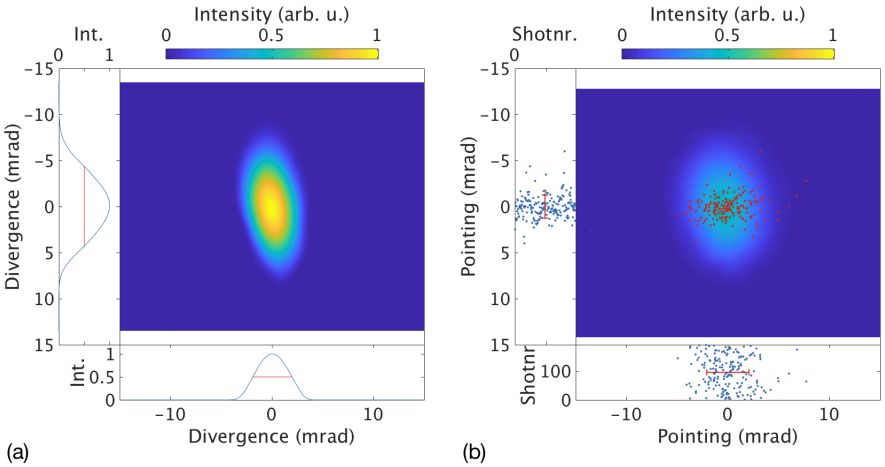

Figure 8.4: Electron divergence (a) and pointing stability (b) determined previously to the spectrum measurements using the profile screen

An exemplary average electron spectrum recorded for 200 shots on the electron spectrometer is presented in figure 8.5 which shows a broad energy distribution, ideal for tuning purposes.

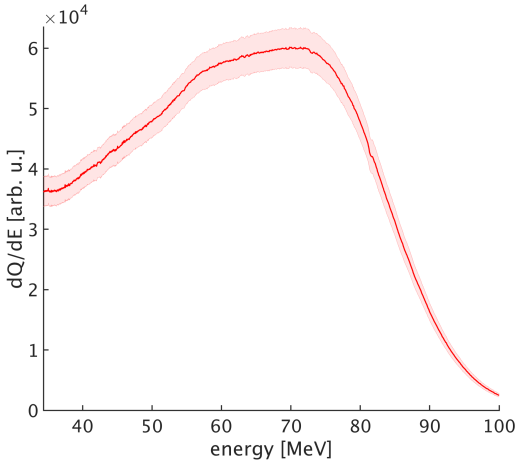

Figure 8.5: Average electron spectrum recorded for 200 shots on the electron spectrometer without the APL in the beamline

8.3 Measurement of X-ray spectra with variable mean energies

It was already known from the first experiment that not too many photons should hit the HEXITEC detector at the same time which implies positioning the detector at 8 m distance from the source and finding a regime with stable electrons of only several pC charge per shot, mainly by reducing the laser power but also fine-tuning of the other shooting parameters. The laser beam energy entering the LWFA-chamber was 109 mJ of which roughly two-thirds (69 mJ) go into the drive laser for electron acceleration and the remaining energy (40 mJ) into the scattering laser beam. Using self-referenced spectral interferometry the pulse lengths of the two laser beams were determined to be (28.9±0.2) fs and (33.1±0.3) fs for the drive and the scattering laser, respectively. The peak a_0 calculated from the pulse length and the focus intensity of the scattering laser was 0.48. For the main laser beam, the peak a_0 was 0.79 and the retrieved plasma density for a backing pressure of (4.4±0.1) bar of the gas mix 99.5 % He with 0.5 % N_2 dopant was (1.67±0.12) × 10^{19} cm^{-3}.

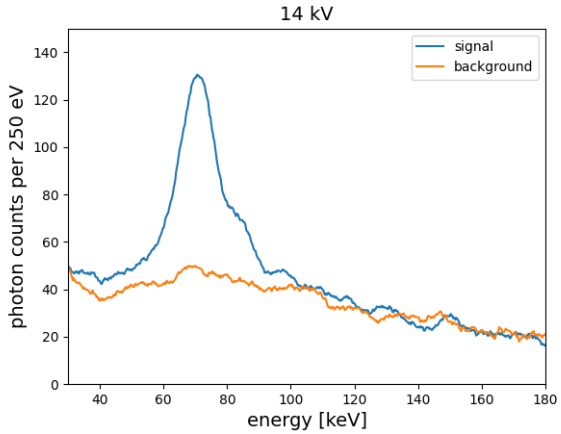

Figure 8.6: Recorded, smoothed spectrum for 14 kV charging voltage with and without the Thomson scattering laser for a measurement time of 240 sec and a laser repetition rate of 1.4 Hz. The signal peak has a mean energy of (70.8 ± 1.5) keV and a bandwidth of (6.9 ± 2.6) keV (σ).

After the first spectrum measurement which showed a clear difference with and without the scattering laser shown in figure 8.6, the on-axis position of the detector was determined. Therefore, it was moved by steps of 7 mm in the horizontal axis and spectra were recorded for each position. As the produced X-ray energy decreases with a larger observation angle (see formula

4.1), the position with the highest recorded energy and intensity has to be found. Figure 8.7 (a) shows the strong energy variation of 50 keV for different transversal detector positions and (b) the corresponding intensity variation. At the thereby determined on-axis position, X-ray spectra were recorded for several different charging voltages, resulting in different electron energies focused to the interaction region, as summarised in table 8.1.

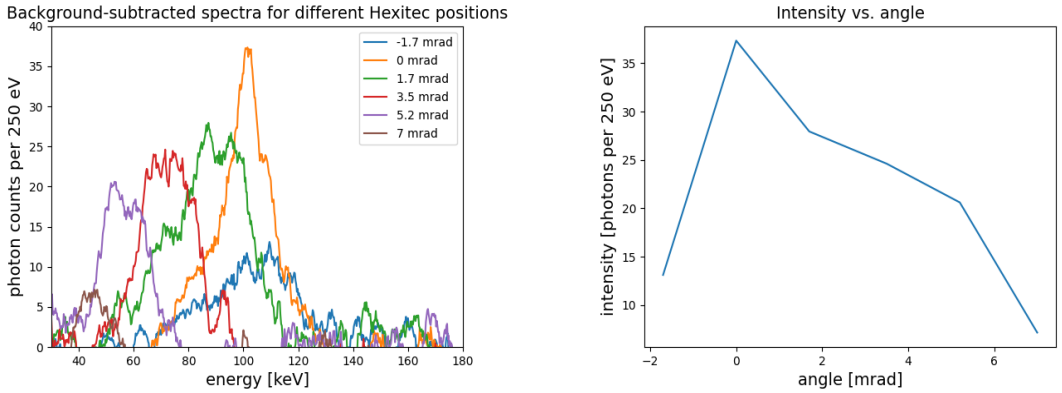

(a) (b)

Figure 8.7: Thomson spectra for 17 kV charging voltage recorded for different transversal detector positions (a) showing variation in mean energy of 50 keV. In (b), the recorded photon intensity for different observation angles is shown where the maximum intensity corresponds to the energy spectrum with the highest recorded energy.

Charging voltage [kV]	APL current [A]	Focused electron energy at interaction point [MeV]
11	330	48.51
12	360	52.92
13	390	57.33
14	420	61.74
15	450	66.15
16	480	70.56
17	510	74.97

Table 8.1: Correlation between charging voltage, expected APL current and focused electron energy at the interaction point. The given high voltage charges capacitors with a total impedance of 16.7 Ω. From the applied charging voltage, the delivered APL current is determined which in turn is used to calculate the focused energies at the interaction point with linear beam transport, based on [134].

Before each measurement, the spatial overlap of the Thomson laser and the focused electron beam was optimised with the procedure described in 8.1.2 and for each setting spectra were recorded for 240 sec with a laser repetition rate of 1.4 Hz. Figure 8.8 shows the background-subtracted X-ray spectra for five different charging voltages covering an energy range from 50 keV up to 100 keV. All spectra are smoothed and corrected for attenuation in air and aluminium as well as for the detection efficiency and dead time of the detector.

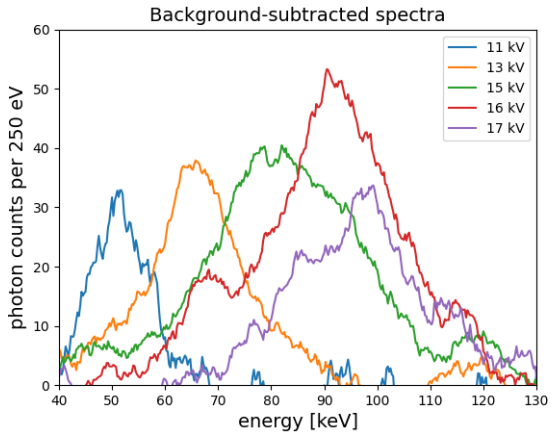

Figure 8.8: Background-subtracted X-ray spectra recorded for five different charging voltages showing a variable mean energy range from 50 keV up to 100 keV

Figure 8.9 presents the mean X-ray energies (a) and bandwidths (b) of the measured spectra.

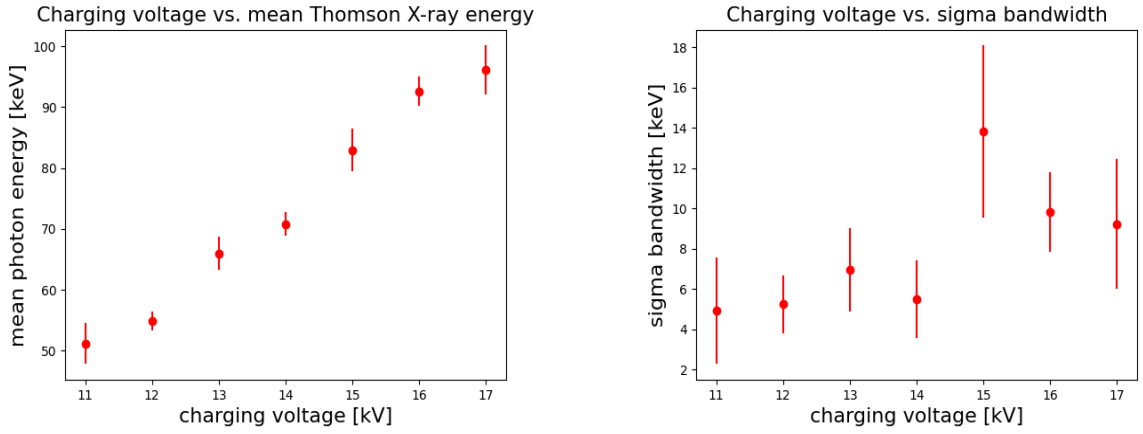

(a) (b)

Figure 8.9: Mean energy (a) and sigma bandwidth (b) of the measured X-ray spectra for different charging voltages

8.4 Calculation of the X-ray source brilliance

A commonly used quantity to compare different X-ray sources and to measure their quality is brilliance or brightness [135]. It is defined as:

$$\frac{\text{photons}}{\text{second} \cdot \text{mrad}^2 \cdot \text{mm}^2 \cdot 0.1\,\% \text{ bandwidth}} \tag{8.3}$$

and describes the number of produced photons of a given wavelength and direction concentrated on an area per second. The term mrad describes the angular beam divergence, mm^2 refers to the source area and 0.1% bandwidth includes the number of photons falling within a bandwidth of 0.1% of the energy where the spectral amplitude is maximum. Since the number of photons was measured with the HEXITEC detector at a distance of 8 m from the interaction point, it takes up 2.5×2.5 mrad^2. The source area is given by the Thomson laser spot size at focus which was determined to be 12 µm FWHM in the presented experiment. Figure 8.10 shows the calculated average (a) and peak brilliance (b), respectively, for different charging voltages. The peak brilliance is calculated by

$$\frac{\text{photons}}{\text{shot} \cdot \text{mrad}^2 \cdot \text{mm}^2 \cdot 0.1\,\% \text{ bandwidth} \cdot \text{pulse duration}} \tag{8.4}$$

where the pulse duration is given by the electron beam duration of 12 fs for a bandwidth of 8 % FWHM at focus which is interacting with the Thomson laser, as determined from simulations.

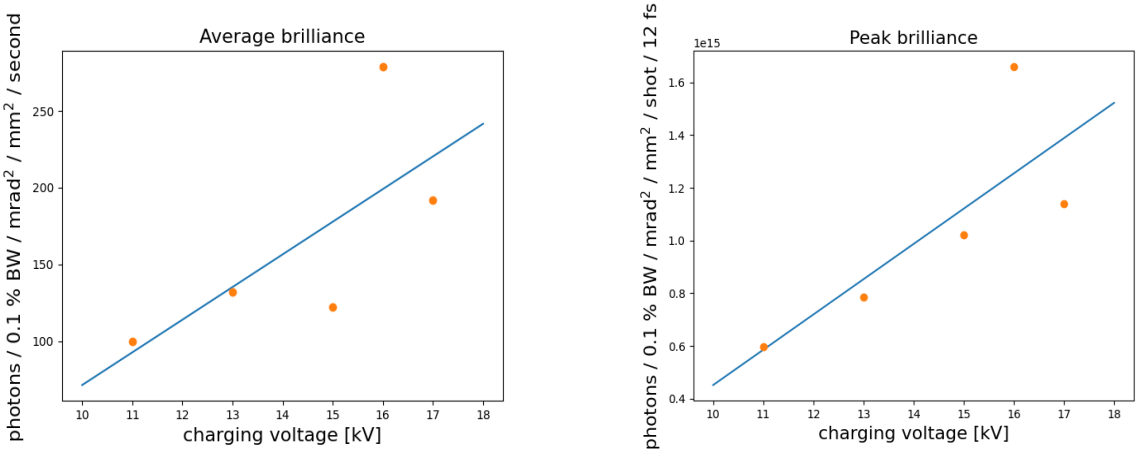

(a) (b)

Figure 8.10: Calculated average (a) and peak (b) brilliance of the X-ray source for different charging voltages

8.5 XFI-measurements with variable incident energies

Having shown the possibility to produce X-ray spectra of different mean energies over a wide range, a new campaign of XFI-measurements was started. To provide good knowledge of the input spectrum, the source parameters were left unchanged, resulting in low mean electron bunch charges. Consequently, the concentration of the fluorescence targets was increased to keep the measurement times low. The setup was located on a table 3.8 m from the interaction point right behind a newly installed electron beam dump consisting of concrete blocks to reduce the Bremsstrahlung background at the target position. A gold foil of 0.1 mm thickness was placed at a 45°-angle with respect to the incident beam and at 4 cm distance to the HEXITEC detector. In this configuration, spectra were recorded for 600 sec for different charging voltages and therefore different mean X-ray energies. As the incident signal peaks are located on Bremsstrahlung background arising from scattering of electrons at the APL, in the chamber and beampipe, all measurements were taken once with the Thomson laser and once without it to determine the fluorescence yield actually induced by Thomson X-rays. Fluorescence yield here is defined as the number of photons in the 3σ-region of the K_α-fluorescence lines. Figure 8.11 shows the resulting recorded gold fluorescence signals for five different incident X-ray spectra. As expected, no fluorescence photons are emitted for irradiation with energies lower than the K-absorption edge at 80.7 keV which is the case for 12 and 14 kV charging voltages. At 15 kV, at least part of the incident photons is energetic enough to produce fluorescence photons and the highest yield is achieved for 16 kV which corresponds to a mean X-ray energy of ~ 90 keV. To fully understand the yield variation, simulations of the actual setup were run. The incident energies and photon numbers were determined from the direct spectrum measurements as well as the applied beam diameter and beam divergence. The bottom plot in figure 8.11 shows good agreement in terms of fluorescence yield between experiment and simulations with a varying incident photon flux for the different spectra. Assuming a constant flux of ~ 1000 photons/sec represented by the green curve, less fluorescence photons are expected and also the difference between the higher incident energies is less significant. The recorded XFI-spectra therefore not only show the change in incident energy, but also the varying photon flux for the different focused electron energies as calculated in section 8.4.

A similar scan was done with an Eppendorf tube containing 78 mg/ml Gd-solution also positioned 4 cm from the HEXITEC detector which itself was at a 90°-angle with respect to the incident beam. As the K-absorption edge of Gd is at 50.2 keV, one would expect a significant amount of fluorescence photons for low charging voltages which was not seen in the measure-

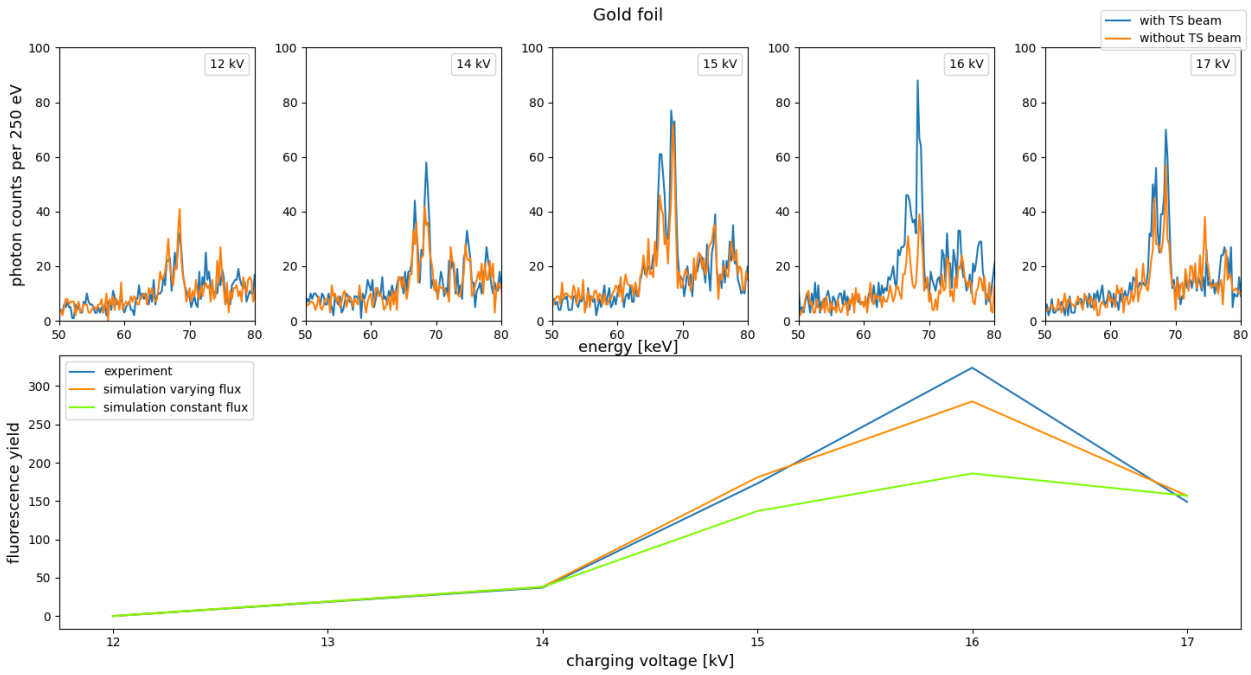

Figure 8.11: Recorded fluorescence photons emitted by a gold foil for different incident energies. At each configuration a spectrum was recorded with (blue curve) and without (orange curve) the scattering laser to determine the fluorescence yield actually produced by Thomson X-rays. The bottom plot shows the recorded fluorescence yield from the experiment (blue curve) and simulations for a varying (orange curve) and constant (green curve) incident photon flux. As expected, the maximum yield is achieved for a charging voltage of 16 kV which results in a mean X-ray energy of ~ 90 keV.

ment where the highest yield was achieved again at higher X-ray energies as shown in figure 8.12. Simulations with the determined varying incident flux revealed that the produced photon numbers in the lower-energetic spectra were not sufficient to induce fluorescence processes. Had the flux been constant for all configurations which is presented by the green curve, the yield would have been significantly higher at the low energies right above the absorption edge.

The observed varying photon flux for different focused energies originates from the fact that the electron charge is not distributed homogeneously over the whole energy range and an imperfect spatial overlap between focused electrons and scattering laser. Even though it was optimised before each setting change, drifts of the Thomson laser focus as well as electron pointing degradation were observed during the measurements. Furthermore, the determination of the X-ray beam axis is crucial in terms of mean energy and intensity hitting the target as presented in section 8.3. As the electron beam pointing changes, also the emission cone of X-rays is altered, which once again emphasises the importance of establishing a stable acceleration regime.

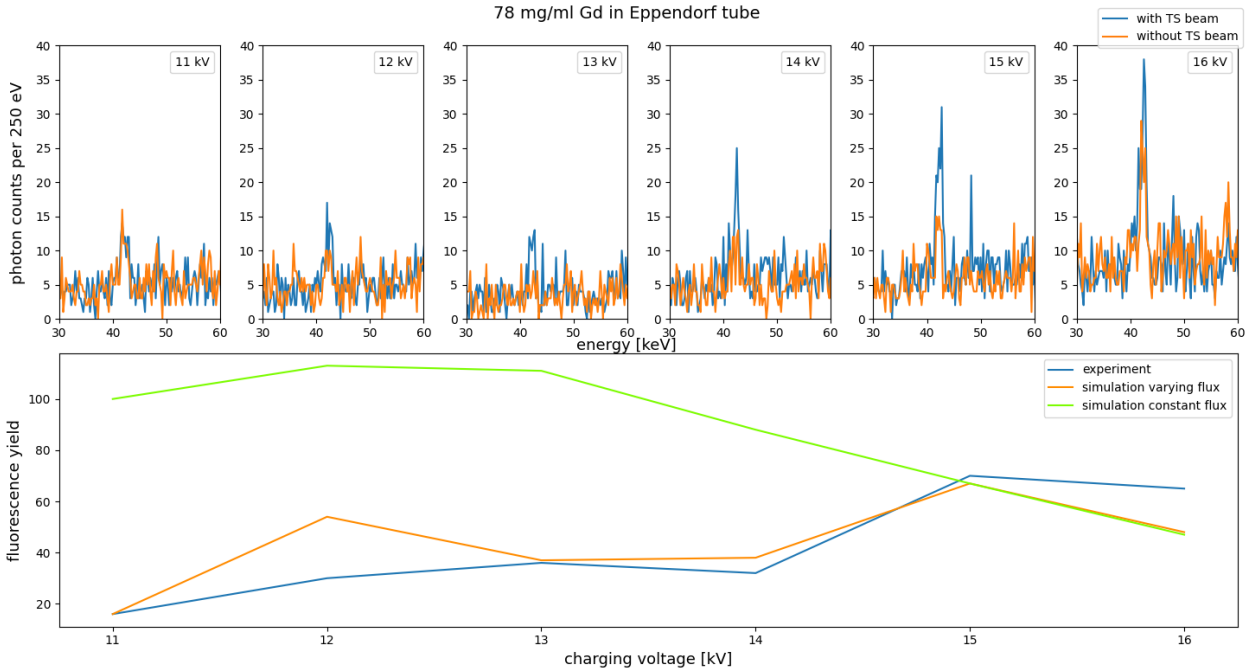

Figure 8.12: Recorded fluorescence photons emitted by a Gd-solution of 78 mg/ml concentration in an Eppendorf tube for different incident energies. At each configuration a spectrum was recorded with (blue curve) and without (orange curve) the scattering laser to determine the fluorescence yield actually produced by Thomson X-rays. The bottom plot shows the recorded fluorescence yield from the experiment (blue curve) and simulations for a varying (orange curve) and constant (green curve) incident photon flux. Had the flux been constant for all configurations, the maximum fluorescence yield would have been recorded for low incident energies right above the absorption edge of Gd at 50.2 keV.

8.6 Discussion of further improvements towards a high-flux X-ray source

The presented experimental results already show a significant improvement in terms of spectral bandwidth which could be reduced from $\sim 40\,\%$ (σ) in the unoptimised setup down to $\sim 10\,\%$ (σ). Nevertheless, further improvements are necessary to reach the ultimate goal of producing quasi-monochromatic X-ray spectra at high fluxes. Table 8.2 lists the current and target source parameters which are required for XFI-applications.

Parameter	Current	Target
Mean X-ray energy [keV]	50 - 100 keV	50 - 100 keV
Bandwidth [% σ]	$\mathcal{O}$ (10 %)	$\mathcal{O}$ ($\leq$7 %)
X-ray beam divergence [mrad]	8.75	1
Peak brilliance [photons/shot $\cdot$ fs $\cdot$ mrad^2 $\cdot$ mm^2 $\cdot$ 0.1 % bandwidth]	$\mathcal{O}(10^{15})$	$\mathcal{O}(10^{18})$
Pulse duration main laser [fs]	$\sim$30	$\sim$30
Pulse duration scattering laser [fs]	$\sim$30	$\sim$600
Repetition rate [Hz]	1.4	$\geq$ 1000

Table 8.2: Current and target parameters of the compact X-ray source dedicated to XFI-based medical imaging applications. While crucial attributes such as the mean X-ray energy and the pulse duration of the main laser have already reached the target value, improvements are necessary to enhance the produced photon flux as well as further decrease the spectral bandwidth.

8.6.1 Laser repetition rate

While some of the listed parameters have already been reached with the current setup, further improvements are necessary to increase the number of produced photons in a narrow bandwidth and emission angle. In the pilot experiments, a laser repetition rate of 1.4 Hz was used but the 25 TW-system can provide a rate up to 10 Hz. Necessary preparation work to enable high repetition rates comprises extensive testing of heating effects of the compressor grating [136] as well as thermal lensing causing the laser focus position to shift over time [137]. Additionally, a newly designed, compact differential pumping cube has to be installed around the gas jet to keep the chamber pressure at tolerable values. Ultimately, the increase in photons per second by only a factor of $\sim$7 reached with the currently used laser system points out the need for a transition to a kHz-laser such as the planned KALDERA-system [138] to gain a factor of $\sim$1000.

8.6.2 Electron bunch charge

Besides increasing the repetition rate of the operating laser system, another gain in the number of photons per shot can be achieved with higher electron bunch charges as the number of produced photons scales linearly with the total charge involved in the interaction. All source parameters presented in table 8.2 were determined from measurements done with intentionally low charges to enable spectrum measurements. The production of stable total bunch charges of $\sim 16\,\mathrm{pC}$ has already been demonstrated as reported in section 7.4. However, in a setup with an APL, not the total bunch charge but the charge within a small effective bandwidth determines the number of photons per shot [82].
The so far used technique of self-truncated ionisation injection to trap electron beams is an efficient and reliable method which works well even for modest laser energy, is generally leading to the production of large energy spread electron beams. Such a broad electron energy spectrum is beneficial for tuning purposes with an APL as it offers the possibility to focus energies over a wide range and scatter them off a laser beam to produce X-ray spectra of variable mean energies. Nevertheless, for an application where X-rays with a certain energy and photon number are required, it is more favourable to produce low energy spread electron beams with high energy density for the scattering process. A method which could be implemented in the already existing setup is based on the creation of a shock front in the gas jet which leads to localised trapping and low energy spreads as demonstrated in [66]. Such a shock front can be created by inserting a wafer into the gas flow and by varying its position along the laser propagation axis, the electron energy can be tuned. Optimisation of the shock by changing the plasma density and laser intensity can increase the beam charge without changing significantly the energy distribution or divergence [66]. Using such a sharp downward density jump enables the generation of stable electron spectra containing a charge per energy interval of more than $10\,\mathrm{pC/MeV}$ as demonstrated in [139].

8.6.3 Scattering laser pulse duration

One main advantage of the combination of LWFA and TS lies in the fact that only a single laser system is needed for both processes. Since a short pulse of $\sim 30\,\mathrm{fs}$ duration is needed for the acceleration process, also the scattering laser has a similar duration which is only slightly longer as it has to travel through a beamsplitter. As already discussed in [82], a large photon production requires long interaction durations and thus a long scattering laser pulse duration. A consequence of stretching the pulse is a reduction of the laser strength parameter a_0 which has to be considered as the produced photon number scales with a_0^2 (see equation 4.3). However,

since a_0 can be high in LWFA-experiments, a reduction is beneficial in terms of prevention of nonlinear effects and high order emission as discussed in section 4.2.5. As the electrons oscillate in the local field of the laser during the interaction, they experience a different laser strength depending on their relative position as well as on the time of interaction. Resultingly, also here, only an effective laser strength is contributing to the bandwidth of the Thomson spectrum [131]. Pulse stretching can be accomplished by propagating the laser pulse through a dispersive medium like e.g. a glass block or chirped mirrors [140]. The option of installing a glass block in the scattering laser beamline is favourable in terms of space and integrability. However, pulse stretching requires an optimisation process in which the focal waist of the laser beam as well as the electron focus are tuned such that the resulting gain in the effective photon production scales with the square root of the laser pulse energy (see equation 4.17).

8.6.4 Spatial overlap improvement and energy monitoring

As described in section 8.1.3, it was not possible to optimise the spatial overlap between focused electrons and scattering laser with the designed diagnostic. Since the photon production is strongly dependent on an optimised transverse overlap, it is essential to develop reliable diagnostic tools. The use of a less temperature-sensitive camera in combination with a scintillating screen of higher light output in the hard X-ray energy range of interest could solve the reported issues. For precise measurements of the actual photon flux, instruments such as flux diodes should be tested. Passivated, implanted, planar silicon (PIPS) detectors developed by CANBERRA are already used at synchrotron beamlines where their capability to accurately measure photon fluxes even in the hard X-ray range has been intensively studied [141]. Another necessity for stable operation comprises the implementation of diagnostics to monitor the laser energy on target. Experiments have shown that the output of the laser amplifier decreases over time and so does the transmission of the beamline as optics get damaged. Both factors require monitoring and compensation as a decreasing laser energy influences both, the acceleration and scattering process and therefore the characteristics of the produced radiation. Such diagnostics should be installed at the output of the second laser amplifier and on the pre-interaction table such that the intial energy as well as the transmission through the vacuum compressor and the beamline can be measured. In case of a decreasing output energy, the voltage applied to the pump lasers can be adjusted and for the case of sinking transmission, all optics in the setup, especially the compressor gratings, should be inspected for burn spots. Contamination layers on mirror surfaces can be removed using Radio Frequency (RF) plasma cleaning which was already studied and tested for the vacuum compressor in the laser laboratory in [136].

8.6.5 Further divergence reduction

Even in a setup with an APL, the Thomson source is polychromatic and divergent. With Highly Annealed Pyrolytic Graphite (HAPG), an advanced type of pyrolytic graphite that combines high integral reflectivity with a very low mosaicity, it is possible to parallelise divergent radiation from a source to a focus point. Optimal mosaic focusing takes place in a symmetric geometry, where the distances between the radiation source and the crystal, and between the crystal and the image plane are nearly equal [142]. As the material has excellent thermal properties, it can be exposed to an environment with high power lasers and electrons without loss of reflectivity. With the use of ray-tracing simulations, shape and material thickness can be determined to meet the requirements of a Thomson X-ray source.

8.6.6 Background reduction and new optimisation algorithms

The main origin of background radiation is Bremsstrahlung produced by electrons as they scatter in the plasma lens, the vacuum chamber walls or in the beampipe before they finally get dumped by a dipole magnet. An earlier separation of electrons and X-rays, e.g. already in the vacuum chamber, in a controlled and radiation safe way, can significantly reduce the amount of background radiation. Furthermore, especially in a setup with optics like an APL in the beam path, the electron pointing stability has to be optimised by means of tuning the laser and gas jet parameters to achieve stable injection. This fine-tuning is an essential part to enable stable operation over many hours. So far, it was done by hand which is not only time-consuming but also not the most efficient way as only one parameter can be scanned at a time. For such a multi-dimensional parameter space, machine learning algorithms could be a promising alternative to achieve fast and potentially even better results.

8.7 LINAC-based Thomson scattering

8.7.1 Source layout and parameters

Even though all-optical laser-driven X-ray sources offer several advantages such as compactness and inherent synchronisation, they still suffer from instabilities mainly in the acceleration process. A possible alternative therefore lies in the use of conventional linear accelerators (LINACs) to produce highly energetic electron bunches in a stable manner. In the context of the Extreme Light Infrastructure Nuclear Physics (ELI-NP) project in Romania [143] such a LINAC was designed with the intention to provide gamma ray beams with tuneable energies from the keV-, up to the MeV-range with narrow bandwidths and high photon numbers. The proposed machine has a length of 25 m and consists of a photoinjector, cavities (C- and S-band structures), a switching dipole magnet, a laser beam circulator with the Thomson interaction cell and finally an electron beam dump for energies up to 300 MeV, as schematically shown in figure 8.13. The original source beam specifications described in [144] are listed in table 8.3. The electron beam and colliding laser pulse parameters needed to meet the source beam specifications are given in tables 8.4 and 8.5, respectively.

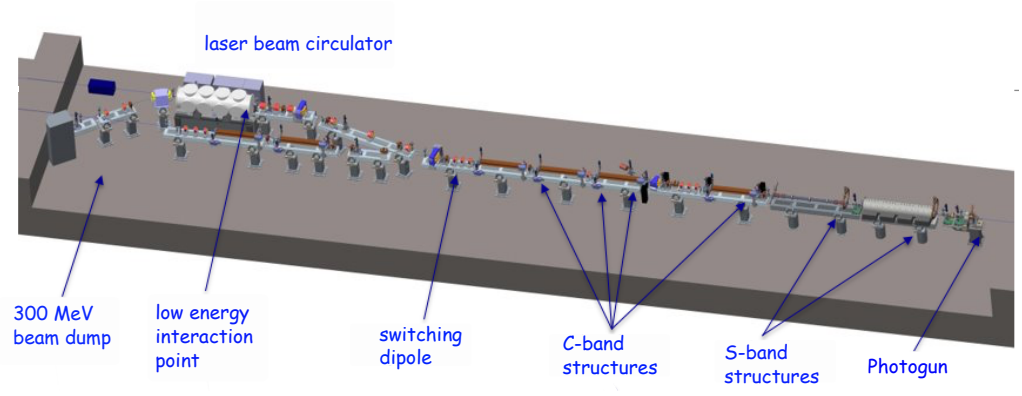

Figure 8.13: Layout of the proposed LINAC consisting of a high brightness photoinjector composed of an S-band RF gun embedded in an emittance compensation solenoid, followed by an S-band and two C-band accelerating cavities [144]. The C-band structure is followed by a final focusing region to provide optimal electron properties at the Thomson scattering interaction point.

It is also possible to use such a setup for lower photon energies without any major modifications of the machine design. The application case of scanning a mouse phantom with a thereby produced pencil X-ray beam will be briefly discussed in the following section.

Energy	0.2 – 19.5 MeV
Bandwidth	$\leq 0.5\,\%\ \sigma$
Divergence	25 – 200 µrad
Photons/s within FWHM bandwidth	8.3×10^{8}
Macro repetition rate	100 Hz
Spectral density	$0.8 - 4 \times 10^{4}$ photons/(s· eV)

Table 8.3: Source beam specifications for a brilliant γ-ray source based on scattering laser photons off relativistic electrons. The acceleration process is done in a conventional LINAC with a total length of 25 m. The calculation was done under the assumption of a 250 pC electron beam colliding with a single pulse from a green (Yb:Yag) laser with specifications as listed in table 8.5 [144].

Energy	80 – 720 MeV
Bunch charge	25 – 400 pC
Bunch length	100 – 400 µm
Emittance	0.2 – 0.6 mm mrad
Bunch energy spread	0.04 – 0.1 %

Table 8.4: Electron beam parameters necessary to fulfil the source beam specifications given in table 8.3. The simulations and calculations were done for a 250 pC electron beam colliding with a single pulse from a green (Yb:Yag) laser with specifications as listed in table 8.5 [144].

Pulse energy	200 mJ
Wavelength	515 nm
Pulse length (FWHM)	3.5 ps
Repetition rate	100 Hz
Focal spot size	> 28 µm

Table 8.5: Parameters of the Yb:Yag collision laser used for the Thomson scattering process [144]. The laser architecture consists of a chirped-pulse amplification design composed of an oscillator, a stretcher, several amplifiers and a compressor, subsequently frequency doubled in a conversion stage. Combining the requirements of high energy and high average power at the same time can be achieved by Yb:Yag lasers due to their superior thermal behaviour, high energy storage capability and laser diode pumping compatibility [145].

Energy	90 keV
Bandwidth (σ)	1 keV
Divergence	0.2 mrad
Number of photons	8.3×10^8
Beam diameter	1 mm

Table 8.6: Source parameters for XFI-scan with a LINAC-based Thomson scattering source

8.7.2 XFI-scan of a mouse phantom

Under the assumption of the source parameters listed in table 8.3, an XFI-simulation was performed. The usual mouse target, a 3 cm diameter PMMA-cylinder containing GNPs of different concentrations is scanned with a pencil X-ray beam of 1 mm diameter and parameters as listed in table 8.6 at a distance of 1 m. A HEXITEC detector of 4 cm^2 active area is positioned at 90° with respect to the incident beam and at 6 cm distance to the target. The recorded spectra for gold concentrations of 18, 10 and 1 mg/ml with their calculated significances are shown in figure 8.14. A scan of the whole phantom consisting of 1800 scan points with the given parameters would take 30 min (without consideration of additional time for motor movements or detector dead time).

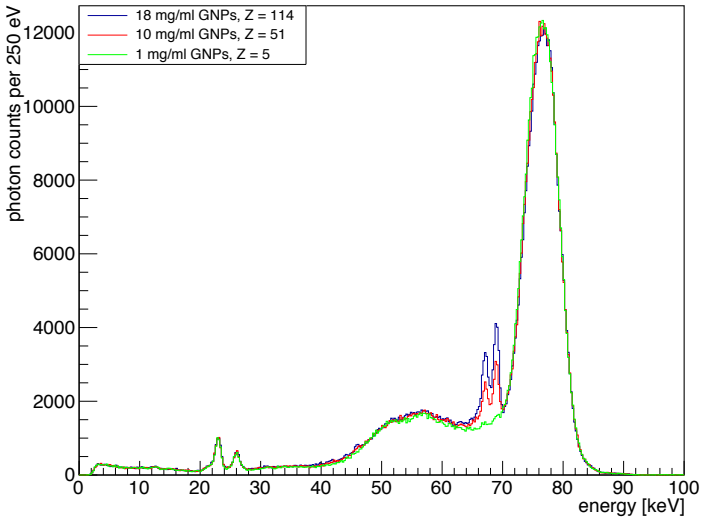

Figure 8.14: Recorded spectra for three different concentrations of GNPs: 18 mg/ml (blue), 10 mg/ml (red) and 1 mg/ml (green). The legend in the top left corner shows the calculated significances of the K_α-peaks which are clearly visible in case of the high concentrations and exactly at the significance limit for 1 mg/ml.

The presented linac-based X-ray source offers suitable beam parameters for XFI, but the total costs and size of such a machine compared to an all-optical source have to be considered. Even though the LINAC itself has a length of roughly 25 m, the necessary laser and photon collimation system needs additional space. Originally, it was designed to fit into an accelerator hall of 90 m length. The total costs of the project, including all components starting from the accelerator to the experimental areas, are estimated to be on the order of 67 million € [144].

A rough estimate of the total costs for the all-optical X-ray source presented in this thesis amounts to 1.5 million € for the laser system and the setup [146]. The laser system and the vacuum chamber fit into a room of roughly 30 m length and even with additional room for measurements, the total footprint is a factor of 2 lower. A new project at DESY with a kHz-laser system has a planned budget of 15 million € [146] which is still only less than one fourth of the ELI-NP costs. Nevertheless, there still are steps to take to improve the stability as well as the produced photon flux in laser-driven accelerators as discussed in section 8.6.

At the moment, one has to make a compromise between compactness combined with inherent synchronisation and reliable beams produced in a larger and more cost-effective facility. Another aspect that has to be kept in mind is the work and manpower required for operation and maintenance of the single components which should be reduced to a minimum for future applications in medical environments.

9 Conclusion and Outlook

First proof-of-principle experiments were set up and conducted to demonstrate the applicability of laser-based Thomson X-ray sources for medical XFI-based imaging purposes. A stable acceleration regime providing electrons with the necessary properties for Thomson scattering which requires fine-tuning of several parameters such as laser energy, spectral phase of the laser and plasma density was successfully established. Self-truncated ionisation injection was found to be the most reliable technique to produce stable electrons with a peak around the design energy. To overlap electrons and the scattering laser in time and space, diagnostics were developed to not only find the correct timing but also maximise the signal strength. The first experimental setup presented in this thesis produced long-term stable electron beams. Those could be used for Thomson scattering and, due to their energy-spreads and divergence, resulted in broadband X-ray spectra. XFI-measurements with gold nanoparticles and gadolinium-solution were possible but the significance of the detected fluorescence peaks was reduced due to a high amount of Bremsstrahlung background and the broadband input spectrum with a suboptimal mean energy.

In order to reduce the effective electron bandwidth and to vary the produced mean X-ray energy, the experimental setup was modified to implement an active plasma lens. Such a device offers the possibility to focus selected electron energies from a broadband spectrum to the interaction region with the scattering laser which lowers the bandwidth of the resulting X-ray spectra. Furthermore, depending on the focused electron energy, the mean X-ray energy can be varied and chosen such that it is above the absorption edge of the selected fluorescence marker. It could be shown that the production of X-ray spectra with a narrower bandwidth is possible over the energy range relevant for XFI from 50 keV up to 100 keV. XFI-measurements with two different elements did reflect the varying incident spectra and could also reveal changing photon fluxes.

Conventional linear accelerators can alternatively be used to drive a Thomson scattering source. The thereby provided electron beam parameters meet some of the requirements for an X-ray source dedicated to medical imaging. However, the total footprint and costs of the

necessary components as well as no inherent synchronisation are drawbacks compared to an all-optical source.

The next steps towards a high-flux, compact X-ray source comprise the transition to higher laser repetition rates, the exploration of different injection mechanisms to increase the charge density at the design energy and an increase of the scattering laser pulse duration. As the photon production per second grows linearly with the laser repetition rate, the transition to a kHz-system increases the photon number per second by a factor of 1000 and accordingly reduces scanning times. Stretching the scattering laser pulse for a longer interaction duration in combination with optimised laser and electron focus characteristics further increases the photon numbers within a defined bandwidth. Bremsstrahlung background reduction can be accomplished with a new beam dump design to separate electrons and X-rays at an earlier point and thereby reduce scattering possibilities. The stability of the acceleration process can benefit from the installation of novel feedback algorithms which enable improved control over the required shooting parameters such as laser energy, plasma density and spectral phase of the laser. Large-area pixelated detectors to measure the X-ray beam properties precisely as well as flux diodes to determine the produced photon fluxes accurately should be tested and enhanced. Further bandwidth reduction can be achieved with X-ray optics based on mosaic crystals which can be easily implemented while maintaining the compactness of the source.

List of Figures

List of Tables

Bibliography

[1] W. C. Röntgen, "ON A NEW KIND OF RAYS," *Science*, vol. 3, pp. 227–231, February 1896.

[2] J. L. Prince and J. M. Links, "Medical Imaging Signals and Systems," *Pearson Education*, 2015.

[3] A. H. Bequerel, "On radioactivity, a new property of matter," *Nobel Lecture*, December 1903.

[4] G. Hevesy, "Adventures in Radioisotope Research: The Collected Papers of George Hevesy," *Pergamon Press*, 1962.

[5] W. Roberts, "Estimation of Strontium in Animal Bone using X-ray Fluorescence Analysis," *Nature*, vol. 183, pp. 887–888, 1959.

[6] G. V. Alexander, "An X-ray Fluorescence Method for the Determination of Calcium, Potassium, Chlorine, Sulfur and Phosphorus in Biological Tissues," *J. Anal. Chem.*, vol. 37, pp. 1671–1674, December 1965.

[7] F. Schulz *et al.*, "Gold Nanoparticles Functionalized With a Fragment of the Neuronal Cell Adhesion Molecule L1 Stimulate L1-mediated Functions," *Nanoscale*, vol. 5, November 2013.

[8] J. Copland *et al.*, "Bioconjugated gold nanoparticles as a molecular based contrast agent: implications for imaging of deep tumors using optoacoustic tomography," *Mol. Imaging Biol.*, vol. 6, pp. 341–349, 2004.

[9] "Gold Nanoparticles: Properties and Applications." `http://sigmaaldrich.com/`. Accessed: 2019-08-22.

[10] A. Simionovici *et al.*, "High-Resolution X-Ray Fluorescence Microtomography of Homogeneous Samples," *IEEE T. Nucl. Sci.*, vol. 47, pp. 2736–2740, December 2000.

[11] T. Tajima and J. Dawson, "Laser Electron Accelerator," *Phys. Rev. Lett.*, vol. 43, pp. 267–270, 1979.

[12] A. W. Chao, "Handbook of Accelerator Physics and Engineering," *World Scientific Pub. Co.*, 2013.

[13] S. Corde *et al.*, "Femtosecond x-rays from laser-plasma accelerators," *Rev. Mod. Phys.*, vol. 85, pp. 1–48, January 2013.

[14] D. Strickland and G. Mourou, "Compression of amplified chirped optical pulses," *Opt. Commun.*, vol. 56, pp. 219–221, December 1985.

[15] F. Arutyunyan and V. Tumanyan, "THE COMPTON EFFECT ON RELATIVISTIC ELECTRONS AND THE POSSIBILITY OF PRODUCING BEAMS OF HARD GAMMA RAYS," *Sov. J. Exp. Theor. Phys.*, vol. 17, December 1963.

[16] F. Arutyunyan and V. Tumanyan, "QUASI-MONOCHROMATIC AND POLARIZED HIGH-ENERGY GAMMA RAYS," *Phys.-Usp*, vol. 7, 1964.

[17] R. Milburn, "Electron Scattering by an Intense Polarized Photon Field," *Phys. Rev. Lett*, vol. 10, pp. 75–77, February 1963.

[18] O. Kulikov, Y. Telnov, E. Filippov, and M. Yakimenko, "Compton effect on moving electrons," *Sov. J. Exp. Theor. Phys.*, vol. 13, pp. 344–346, December 1964.

[19] E. Esarey, S. Ride, and P. Sprangle, "Nonlinear Thomson scattering of intense laser pulses from beams and plasmas," *Phys. Rev. E*, vol. 48, pp. 3003–3021, October 1993.

[20] I. Pogorelsky, I. Ben-Zvi, X. Wang, and T. Hirose, "Femtosecond laser synchrotron sources based on Compton scattering in plasma channels," *Nucl. Instrum. Methods Phys. Res. A*, vol. 455, pp. 176–180, November 2000.

[21] H. Ohgaki *et al.*, "Linearly polarized photons from Compton backscattering of laser light for nuclear resonance fluorescence experiments," *Nucl. Instrum. Methods Phys. Res. A*, vol. 353, pp. 384–388, December 1994.

[22] W. S. Graves *et al.*, "Compact x-ray source based on burst-mode inverse Compton scattering at 100 kHz," *Phys. Rev. ST Accel. Beams*, vol. 17, December 2014.

[23] N. Bohr, "On the Constitution of Atoms and Molecules," *Philos. Mag.*, vol. 26, 1913.

[24] J. Stachel, D. C. Cassidy, J. Renn, and R. Schulmann, "The collected papers of Albert Einstein, Volume 2: The Swiss Years: Writings 1900-1909," *Princeton University Press*, 1989.

[25] J. Beutel, H. L. Kundel, and R. L. van Metter, "Handbook of Medical Imaging Volume 1," *SPIE PRESS*, 2000.

[26] "X-Ray attenuation and absorption calculator." `/https://web-docs.gsi.de/~stoe_exp/web_programs/x_ray_absorption/index.php/`. Accessed: 2019-05-12.

[27] "MathWorks." `https://mathworks.com`. Accessed: 2019-10-12.

[28] "Patient dose information: guidance." `https://www.gov.uk/government/publications/medical-radiation-patient-doses/patient-dose-information-guidance`. Accessed: 2019-12-05.

[29] S. Cherry, J. Sorenson, and M. Phelps, "Physics in nuclear medicine," *Elsevier Inc.*, 2012.

[30] "AMPTEK XR-100 CdTe X-Ray and Gamma Ray Detector." `http://amptek.com/products/xr-100cdte-x-ray-and-gamma-ray-detector`. Accessed: 2019-06-30.

[31] "Understanding Charge Trapping in Amptek CdTe Detectors." `https://amptek.com/documentation/`. Accessed: 2019-03-05.

[32] M. D. Wilson *et al.*, "A 10 cm x 10 cm CdTe Spectroscopic Imaging Detector based on the HEXITEC ASIC," *J. Instrum.*, vol. 10, October 2015.

[33] "Quantum Detectors." `https://quantumdetectors.com/n/products/hexitec/`. Accessed: 2019-03-25.

[34] M. Veale *et al.*, "Investigating the small pixel effect in CdZnTe Hard X-ray detectors - The PIXIE ASIC," *IEEE Nuclear Science Symposium and Medical Imaging Conference*, 2011.

[35] Z. He, "Review of the Shockley-Ramo theorem and its application in semiconductor gamma-ray detectors," *Nucl. Instrum. Methods Phys. Res.*, vol. 463, pp. 250–267, May 2001.

[36] Salah Awadalla, "Solid-State Radiation Detectors: Technology and Applications," *CRC Press*, vol. 1, 2017.

[37] C. Chen *et al.*, "Numerical Modeling of Charge-Sharing in CdZnTe Pixel Detectors," *IEEE NSS. Conf. Rec.*, 2000.

[38] P. Seller *et al.*, "Pixellated Cd(Zn)Te high-energy X-ray instrument," *J. Instrum.*, vol. 6, December 2011.

[39] J. Peng and X. Liang, "Progress in research on gold nanoparticles in cancer management," *Medicine (Baltimore)*, vol. 98, March 2019.

[40] L. Yuan *et al.*, "Chiral polymer modified nanoparticles selectively induce autophagy of cancer cells for tumor ablation," *J. Nanobiotechnology*, vol. 16, July 2018.

[41] Y. Bae and K. Park, "Targeted drug delivery to tumors: Myths, reality and possibility," *J. Control Release*, vol. 153, pp. 198–205, August 2011.

[42] E. Sykes *et al.*, "Tailoring Nanoparticle Designs to Target Cancer Based on Tumor Pathophysiology," *Proc. Natl. Acad. Sci. USA.*, vol. 113, pp. 1142–1151, March 2016.

[43] A. Rastinehad *et al.*, "Gold nanoshell-localized photothermal ablation of prostate tumors in a clinical pilot device study," *Proc. Natl. Acad. Sci. USA.*, vol. 116, pp. 18590–18596, September 2019.

[44] M. Xu *et al.*, "How Entanglement of Different Physiochemical Properties Complicates the Prediction of in Vitro and in Vivo Interactions of Gold Nanoparticles," *ACS Nano*, vol. 12, pp. 10104–10113, September 2018.

[45] T. Cedervall *et al.*, "Understanding the nanoparticle-protein corona using methods to quantify exchange rates and affinities of proteins for nanoparticles," *Proc. Natl. Acad. Sci. U.S.A.*, vol. 104, pp. 2050–2055, February 2007.

[46] O. Vilanova *et al.*, "Understanding the Kinetics of Protein-Nanoparticle Corona Formation," *ACS Nano*, vol. 10, pp. 10842–10850, November 2016.

[47] "X-Ray Emission Lines." `http://www.med.harvard.edu/jpnm/physics/refs/xrayemis.html`. Accessed: 2019-08-08.

[48] Particle Data Group, "Review of Particle Physics," *Chin. Phys. C*, vol. 38, no. 090001, 2014.

[49] L. Kirkup, "Experimental methods: an introduction to the analysis and presentation of data," *Wiley*, 1994.

[50] P. Armitage and G. Berry, "Statistical Methods in Medical research," *Blackwell: Oxford*, vol. 3, 1994.

[51] M. Pentz, M. Shott, and F. Aprahamian, "Handling Experimental Data," *Open University Press*, 1988.

[52] J. R. Taylor, "Introduction To Error Analysis," *University Science Books, U.S.*, 1997.

[53] E. Esarey, C. Schroeder, and W. Leemans, "Physics of laser-driven plasma-based electron accelerators," *Rev. Mod. Phys*, vol. 81, pp. 1229–1285, August 2009.

[54] F. F. Chen, "Introduction to Plasma Physics and Controlled Fusion," *Plenum Press*, 1974.

[55] P. Gibbon, "Introduction to Plasma Physics," *Accelerator School: Plasma Wake Acceleration*, 2014.

[56] K. Midorikawa, E. Takahashi, and Y. Nabekawa, "High-Brightness Coherent Soft X-Ray Generation by High-Order Harmonics," *AIP Conference Proceedings*, vol. 634, 2002.

[57] B. Cros, "Laser-driven Plasma Wakefield: Propagation Effects," *CAS-CERN Accelerator School: Plasma Wake Acceleration*, 2014.

[58] J. M. Dawson, "Nonlinear Electron Oscillations in a Cold Plasma," *Phys. Rev.*, vol. 113, pp. 383–387, January 1959.

[59] A. Pak *et al.*, "Injection and Trapping of Tunnel-Ionized Electrons into Laser-Produced Wakes," *Phys. Rev. Lett.*, vol. 104, p. 025003, January 2010.

[60] S. Mangles *et al.*, "Self-injection threshold in self-guided laser wakefield accelerators," *Phys. Rev. STAB.*, vol. 15, p. 011302, January 2012.

[61] A. Modena *et al.*, "Electron acceleration from the breaking of relativistic plasma waves," *Nature*, vol. 377, pp. 606–608, September 1995.

[62] J. Faure *et al.*, "Controlled injection and acceleration of electrons in plasma wakefields by colliding laser pulses," *Nature*, vol. 444, pp. 737–739, December 2006.

[63] G. Fubiani, E. Esarey, C. Schroeder, and W. Leemans, "Beat wave injection of electrons into plasma waves using two interfering laser pulses," *Phys. Rev. E*, vol. 70, 2004.

[64] C. McGuffey *et al.*, "Ionization Induced Trapping in a Laser Wakefield Accelerator," *Phys. Rev. Lett.*, vol. 104, p. 025004, 2010.

[65] J. Liu *et al.*, "All-Optical Cascaded Laser Wakefield Accelerator Using Ionization-Induced Injection," *Phys. Rev. Lett.*, vol. 107, 2011.

[66] C. Thaury *et al.*, "Shock assisted ionization injection in laser-plasma accelerators," *Sci. Rep.*, vol. 5, 2015.

[67] A. Irman *et al.*, "Improved performance of laser wakefield acceleration by tailored self-truncated ionization injection," *Plasma Phys. Control. Fusion*, vol. 60, 2018.

[68] M. Zeng *et al.*, "Self-truncated ionization injection and consequent monoenergetic electron bunches in laser wakefield acceleration," *Phys. Plasmas*, vol. 21, p. 030701, 2014.

[69] A. Ting *et al.*, "Observation of 20 eV x-ray generation in a proof-of-principle laser synchrotron source experiment," *J. Appl. Phys.*, vol. 78, March 1995.

[70] W. Leemans *et al.*, "X-Ray Based Subpicosecond Electron Bunch Characterization Using 90° Thomson Scattering," *Phys. Rev. Lett.*, vol. 77, pp. 4182–4185, November 1996.

[71] W. Leemans *et al.*, "Radiation from laser accelerated electron bunches: coherent terahertz and femtosecond X-rays," *IEEE Trans. Plasma Sci.*, vol. 33, pp. 8–22, February 2005.

[72] K. Achterhold *et al.*, "Monochromatic computed tomography with a compact laser-driven X-ray source," *Sci. Rep.*, vol. 3, February 2013.

[73] "Lynceantech." `http://www.lynceantech.com/`. Accessed: 2019-10-22.

[74] K. Weeks, V. Litvinenko, and M. Madey, "The Compton backscattering process and radiotherapy," *Med. Phys.*, vol. 24, pp. 417–423, March 1998.

[75] B. Quiter, B. Ludewigt, V. Mozin, and S. Prussin, "Nuclear Resonance Fluorescence for Materials Assay," *IEEE Trans. Nucl. Sci.*, vol. 58, pp. 400–403, March 2011.

[76] H.Toyokawa, H. Ohgaki, T. Mikado, and K. Yamada, "High-energy photon radiography system using laser-Compton scattering for inspection of bulk materials," *Rev. Sci. Instrum.*, vol. 73, May 2002.

[77] J. van Tilborg *et al.*, "Temporal Characterization of Femtosecond Laser-Plasma-Accelerated Electron Bunches Using Terahertz Radiation," *Phys. Rev. Lett.*, vol. 96, p. 014801, January 2006.

[78] S. Rykovanov *et al.*, "Quasi-monoenergetic femtosecond photon sources from Thomson Scattering using laser plasma accelerators and plasma channels," *J. Phys. B.: Atomic, Molecular and Optical Physics*, vol. 47, November 2014.

[79] W. P. Leemans *et al.*, "GeV electron beams from a centimetre-scale accelerator," *Nat. Phys.*, vol. 2, pp. 696–699, September 2006.

[80] "Terawatt systems." `https://www.thalesgroup.com/en/worldwide/group/market-specific-solutions-lasers-science-applications/terawatt-systems`. Accessed: 2019-11-10.

[81] V. Karagodsky and L. Schächter, "High efficiency x-ray source based on inverse Compton scattering in an optical Bragg structure," *Plasma Phys. Control. Fusion*, vol. 53, December 2010.

[82] T. Brümmer *et al.*, "Design study for a compact laser-driven source for medical x-ray fluorescence imaging," *Phys. Rev. Accel. Beams*, vol. 23, p. 031601, March 2020.

[83] K. Poder *et al.*, "Experimental Signatures of the Quantum Nature of Radiation Reaction in the Field of an Ultraintense Laser," *Phys. Rev. X*, vol. 8, July 2018.

[84] D. Seipt and B. Kämpfer, "Nonlinear Compton scattering of ultrashort intense laser pulses," *Phys. Rev. A*, vol. 83, February 2011.

[85] C. Geddes *et al.*, "High-quality electron beams from laser wakefield accelerator using plasma-channel guiding," *Nature*, vol. 431, pp. 538–541, September 2004.

[86] C. Maroli, V. Petrillo, P. Tomassini, and L. Serafini, "Nonlinear effects in Thomson backscattering," *Phys. Rev. ST Accel. Beams*, vol. 16, March 2013.

[87] M. Chen *et al.*, "Modeling classical and quantum radiation from laser-plasma accelerators," *Phys. Rev. ST Accel. Beams*, vol. 16, p. 030701, March 2013.

[88] B. Terzic, K. Deitrick, A. Hofler, and G. Krafft, "Narrowband Emission in Thomson Sources Operating in the High-Field Regime," *Phys. Rev. Lett.*, vol. 112, February 2014.

[89] H. Schwoerer *et al.*, "Thomson-Backscattered X Rays From Laser-Accelerated Electrons," *Phys. Rev. Lett.*, vol. 96, p. 014802, January 2006.

[90] K. T. Phuoc *et al.*, "All-optical Compton gamma-ray source," *Nat. Photonics*, vol. 6, pp. 308–311, April 2012.

[91] J. Osterhoff *et al.*, "Transport and Non-Invasive Position Detection of Electron Beams from Laser-Plasma Accelerators," *AIP Conf. Proc.*, vol. 1299, November 2010.

[92] R. Weingartner *et al.*, "Imaging laser-wakefield accelerated electrons using miniature magnetic quadrupole lenses," *Phys. Rev. ST Accel. Beams*, vol. 14, p. 052801, May 2011.

[93] C. Schroeder, E. Esarey, C. Benedetti, and W. Leemans, "Control of focusing forces and emittances in plasma-based accelerators using near-hollow plasma channels," *Phys. Plasmas*, vol. 20, July 2013.

[94] J. van Tilborg *et al.*, "Comparative study of plasma lenses in high-quality electron accelerator transport lines," *Phys. Plasmas*, vol. 25, p. 056702, February 2018.

[95] J.-H. Röckemann *et al.*, "Direct Measurement of Focusing Fields in Active Plasma Lenses," *Phys. Rev. Accel. Beams*, vol. 21, December 2018.

[96] J. van Tilborg *et al.*, "Active Plasma Lensing for Relativistic Laser-Plasma-Accelerated Electron Beams," *Phys. Rev. Lett.*, vol. 115, October 2015.

[97] N. D. Powers *et al.*, "Quasi-monoenergetic and tunable X-rays from a laser-driven Compton light source," *Nat. Photonics*, vol. 8, pp. 28–31, October 2014.

[98] K. Khrennikov *et al.*, "Tunable All-Optical Quasimonochromatic Thomson X-Ray Source in the Nonlinear Regime," *Phys. Rev. Lett.*, vol. 114, p. 195003, May 2015.

[99] W. Yan, C. Fruhling, G. Golovin, *et al.*, "High-order multiphoton Thomson scattering," *Nat. Photonics*, vol. 11, pp. 514–520, June 2017.

[100] G. Sarri *et al.*, "Ultrahigh Brilliance Multi-Mev γ-Ray Beams from Nonlinear Relativistic Thomson Scattering," *Phys. Rev. Lett.*, vol. 113, p. 224801, November 2014.

[101] F. Grüner *et al.*, "Localising functionalised gold-nanoparticles in murine spinal cords by X-ray fluorescence imaging and background reduction through spatial filtering for human-sized objects," *Sci. Rep.*, vol. 8, November 2018.

[102] S. Agostinelli *et al.*, "GEANT4- a simulation toolkit," *Nucl. Instrum. Methods Phys. Res. A*, vol. 506, pp. 250–303, July 2013.

[103] "Read-out and detector response." `http://www.ge.infn.it/geant4/events/nss2003/geant4course.html`. Accessed: 2019-05-18.

[104] "GEANT4 Book For Application Developers," *GEANT4 Collaboration*, vol. 10.4, 2017.

[105] S. T. Perkins, D. E. Cullen, and S. M. Seltzer, "Tables and Graphs of Electron-Interaction Cross Sections from 10 eV to 100 GeV Derived from the LLNL Evaluated Electron Data Library (EEDL), Z = 1-100," *UCRL-50400*, vol. 31, November 1991.

[106] D. E. Cullen, J. H. Hubbel, and L. Kissel, "EPDL97: The Evaluated Photon Data Library '97 Version," *UCRL-50400*, vol. 6, September 1997.

[107] S. Chauvie *et al.*, "Geant4 low energy electromagnetic physics," *IEEE Xplore*, vol. 3, November 2004.

[108] "ROOT." `https://root.cern.ch`. Accessed: 2019-10-12.

[109] "Pulsar TW." `https://amplitude-laser.com/produit/pulsar-tw/`. Accessed: 2019-11-03.

[110] Courtesy of Simon Bohlen.

[111] R. Paschotta, "Pulse shapers," *Encyclopedia of Laser Physics and Technology*, vol. 1, October 2008.

[112] *DAZZLER manual*.

[113] *WIZZLER manual*.

[114] T. Oksenhendler, "Self-referenced spectral interferometry theory," *FASTLITE*, 2012.

[115] N. Minkovski, G. Petrov, and S. Saltiel, "Nonlinear polarization rotation and orthogonal polarization generation experienced in a single-beam configuration," *J. Opt. Soc. Am. B*, vol. 21, September 2004.

[116] M. Iliev, "Cross-polarized wave generation (XPW) for ultrafast laser pulse characterization and intensity contrast enhancement," *PhD thesis*, 2014.

[117] A. Aschikhin *et al.*, "The FLASHForward facility at DESY," *Nucl. Instrum. Methods Phys. Res*, vol. 806, pp. 175–183, January 2016.

[118] D. Lipka *et al.*, "DARK CURRENT MONITOR FOR THE EUROPEAN XFEL," *Proc. of DIPAC 2011*, 2011.

[119] D. Lipka, J. Lund-Nielsen, and M. Seebach, "RESONATOR FOR CHARGE MEASUREMENT AT REGAE," *Proc. of IBIC 2013*, 2013.

[120] "DRZ." `https://www.m-chemical.co.jp/en/products/departments/mcc/ledmat/product/1201037_7550.html`. Accessed: 2019-11-15.

[121] M. Veale *et al.*, "Measurements of charge sharing in small pixel CdTe detectors," *Nucl. Instrum. Methods Phys. Res.*, vol. 767, pp. 218–226, 2014.

[122] M. Veale *et al.*, "X-ray micro-beam characterization of a small pixel spectroscopic CdTe detector," *J. Instrum.*, vol. 7, p. 07017, July 2012.

[123] M. Veale, S. Bell, P. Seller, M. Wilson, and V. Kachkanov, "X-ray micro-beam characterization of a small pixel spectroscopic CdTe detector," *J. Instrum.*, vol. 7, July 2012.

[124] A. Brahme, "Comprehensive Biomedical Physics," *Elsevier*, vol. 8, pp. 285–314, 2014.

[125] D. Duarte, "Edge effects in a pixelated CdTe radiation detector," *PhD thesis*, August 2016.

[126] F. Brandi and L. Gizzi, "Optical diagnostics for density measurement in high-quality laser-plasma electron accelerators," *High Power Laser Science and Engineering*, vol. 7, March 2019.

[127] S. Merk *et al.*, "Diagnostic of Laser-Induced Plasma Using Abel Inversion and Radiation Modeling," *Appl. Spectrosc.*, vol. 67, August 2013.

[128] R. Dux, "Plasmainterferometry," tech. rep., Max Planck Institute for Plasma Physics.

[129] C. G. Parigger, G. Gautam, and D. M. Surmick, "Radial electron density measurements in laser-induced plasma from Abel inverted hydrogen Balmer beta line profiles," *International Review of Atomic and Molecular Physics*, vol. 6, pp. 43–55, June 2015.

[130] J. M. Cole, "Diagnosis and application of laser wakefield accelerators," *PhD thesis*, 2016.

[131] J. M. Krämer *et al.*, "Making spectral shape measurements in inverse Compton scattering a tool for advanced diagnostic applications," *Sci. Rep.*, vol. 8, January 2018.

[132] C. A. Lindstrøm *et al.*, "Emittance Preservation in an Aberration-Free Active Plasma Lens," *Phys. Rev. Lett.*, vol. 121, p. 194801, November 2018.

[133] S. Odoulov *et al.*, "Interference and holography with femtosecond laser pulses of different colours," *Nat. Commun.*, vol. 6, February 2015.

[134] M. Meisel, "Emittance Measurement of Electron Beams from Laser Wakefield Acceleration using an Active Plasma Lens," *Master's thesis*, July 2018.

[135] J. Nielsen, "Elements of modern X-ray physics," *John Wiley*, 2011.

[136] J.-L. Dresselhaus, "Paving the way of high repetition rate laser wakefield acceleration by solving heat induced grating deformation issues," *Master's thesis*, June 2020.

[137] S. Faas, D. J. Foerster, R. Weber, and T. Graf, "Determination of the thermally induced focal shift of processing optics for ultrafast lasers with average powers of up to 525 W," *Opt. Express*, vol. 26, October 2018.

[138] W. Leemans *et al.*, "KALERDA - High average power laser plasma accelerator project at DESY," *4th European Advanced Accelerator Concepts Workshop*, 2019.

[139] A. Buck *et al.*, "Shock-Front Injector for High-Quality Laser-Plasma Acceleration," *Phys. Rev. Lett.*, vol. 110, p. 185006, May 2013.

[140] H. J. Eichler and J. Eichler and O. Lux, "Lasers: Basics, Advances and Applications," *Springer*, 2018.

[141] R. L. Owen, J. M. Holton, C. Schulze-Briese, and E. F. Garman, "Determination of X-ray flux using silicon pin diodes," *J. Synchrotron Rad.*, vol. 16, pp. 143–151, November 2009.

[142] M. Gerlach *et al.*, "Characterization of HAPG mosaic crystals using synchrotron radiation," *J. Appl. Cryst.*, vol. 48, pp. 1381—-1390, July 2015.

[143] "Extreme Light Infrastructure Nuclear Physics." `https://www.eli-np.ro/index.php`. Accessed: 2020-01-06.

[144] O. Adriani and others, "EuroGammaS proposal for the ELI-NP Gamma beam System," tech. rep., July 2014.

[145] Jörg Neuhaus, "Passively mode-locked Yb:YAG thin-disk laser with active multipass geometry," *PhD thesis*, 2009.

[146] J. Osterhoff. Private Communication, 2020.

Acknowledgement

Firstly, I would like to express my gratitude to my advisor Prof. Dr. Florian Grüner for the continuous support of my PhD study and related research, for your patience and immense motivation. I am very grateful for all the experience I could gather at conferences, workshops and during experiments.
I would like to also thank my second supervisor, Dr. Jens Osterhoff, to give me the opportunity to work in the laboratory and gain highly interesting knowledge about high-laser systems and plasma wakefield accelerators.
My sincere thanks also go to the core BondLab-team consisting of Simon, Martin, Kris and Jon. Not only your great support at the beginning of my thesis when I entered a for me completely unknown territory, but also the very enjoyable after-work activities made working days productive and motivating. Hopefully, we will get a chance to celebrate the joint successes soon!
A big thanks also go to the XFI- and programming-experts Oliver and Christian who always had an open ear for me even if my presence in the office was very infrequent. Even though they are exhausting, I always enjoy the beamtimes at PETRA III with the two of you.
The HEXITEC detector used for the measurements presented in this thesis was kindly provided by colleagues from RAL who helped us with the setup and handling of the detector and software. Especially Matthew Veale was very supportive, explaining us the single steps with great patience and helping us with the data analysis.
Besides my great colleagues at work, I would also like to thank my whole family back in Austria. Even though the distance is far, I always got support in many different ways and especially my parents and my brother did always believe in me.
Last but not least, I would like to thank the one person who had to endure the last four years with me and was always there for me even during difficult times. Thank you, Paul!

Eidesstattliche Versicherung / Declaration on oath

Hiermit versichere ich an Eides statt, die vorliegende Dissertationsschrift selbst verfasst und keine anderen als die angegebenen Hilfsmittel und Quellen benutzt zu haben.

Die eingereichte schriftliche Fassung entspricht der auf dem elektronischen Speichermedium.

Die Dissertation wurde in der vorgelegten oder einer ähnlichen Form nicht schon einmal in einem früheren Promotionsverfahren angenommen oder als ungenügend beurteilt.

Hamburg, den 24. Juni 2020

_____

Theresa Staufer